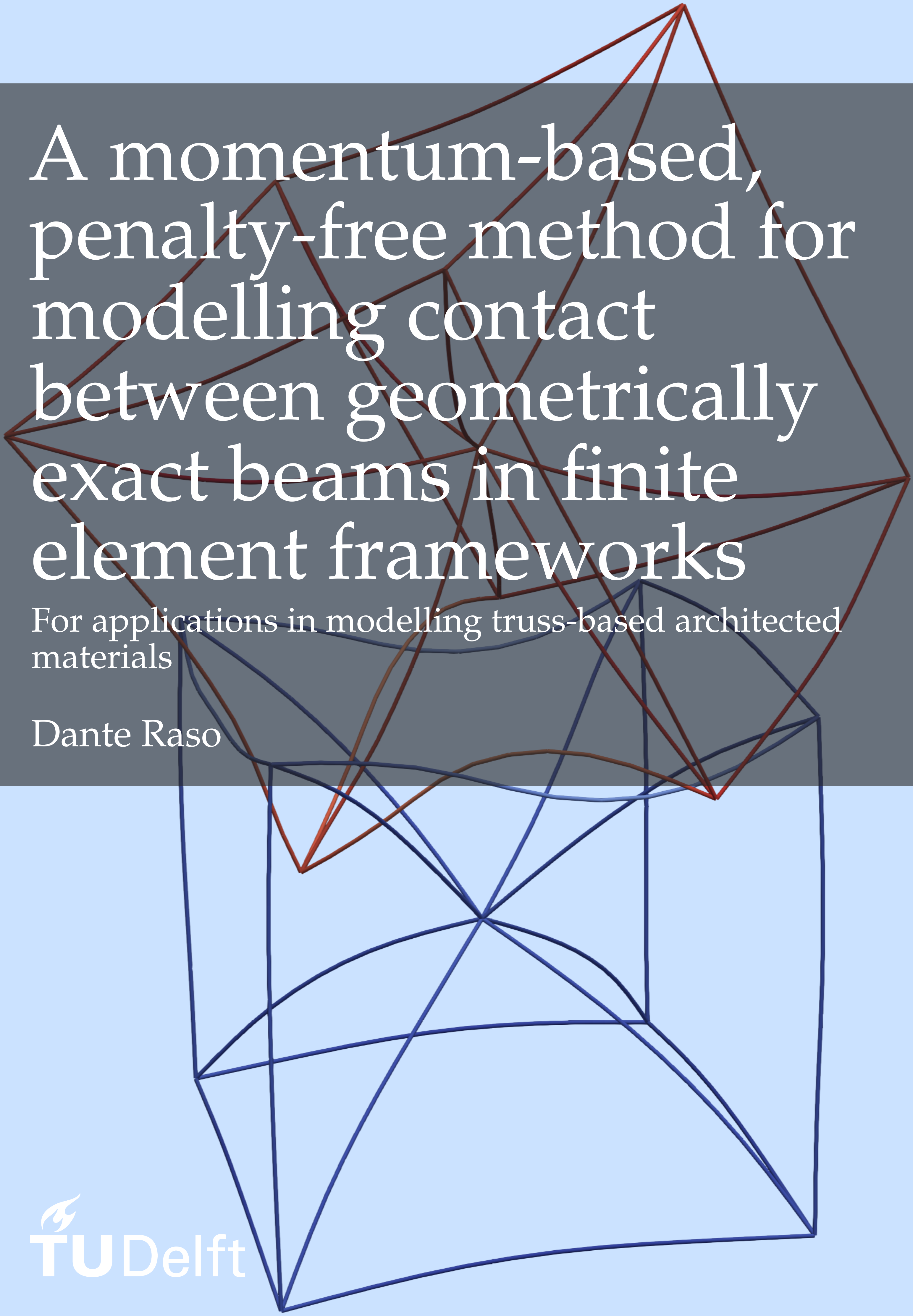

A momentum-based, penalty-free method for modelling contact between geometrically exact beams in finite element frameworks

For applications in modelling truss-based architected materials

Dante Raso

TU Delft

A momentum-based, penalty-free method for modelling contact between geometrically exact beams in finite element frameworks

For applications in modelling truss-based architected materials

by

Dante Raso

to obtain the degree of Master of Science
at the Delft University of Technology,
to be defended publicly on 26 August 2024 at 13:00.

Student number:	5670810	
Project duration:	8 January 2024 – 26 August 2024	
Thesis committee:	Dr. B. Giovanardi,	TU Delft, supervisor
	Dr. S. Turteltaub,	TU Delft, chair
	Dr. N. Yue,	TU Delft, external member

An electronic version of this thesis is available at `http://repository.tudelft.nl/`.

TU Delft

Acknowledgements

First and foremost, I would like to express my deepest gratitude to Dr. Bianca Giovanardi, for her invaluable guidance, unwavering support, and insightful feedback as my thesis supervisor. I am also grateful to Sai Kubair Kota, whose expertise and dedication as a PhD candidate have gotten me out of more than a few jams.

I would also like to extend my heartfelt thanks to my entire family. Your constant love, patience, and encouragement from across the pond have been my foundation. To my friends, thank you for your support and for the occasional distraction that helped me maintain balance.

And, of course, a special thanks to my four-legged friend, Euclid, who provided untimely comic relief and unwavering loyalty throughout the writing process. While you ultimately have not lived up to your namesake in mathematical prowess, your presence was a comforting reminder of the simple joys in life.

Dante Raso
Delft, October 2024

"[...] it can be concluded for the present that there exists nothing which can be called the robust method for all different types of contact simulations [...] However, especially due to the fact that such a method does not exist, it is necessary to discuss those methods which are on the market in the light of good or bad behaviour."

\- Peter Wriggers

Executive summary

This thesis investigates the development and application of a novel finite element beam-to-beam contact model, addressing the shortcomings of existing LAGRANGE multiplier and penalty methods, which suffer from high computational costs and dependency on arbitrary parameters. The proposed model is based on a technique called the decomposition contact response (DCR) method, originally derived for modelling contact with solid elements by Cirak and West [1], and adapted for beam elements in this study. A key motivation for this research is the development of hypervelocity impact (HVI) shields for spacecraft vulnerable to micrometeoroid and orbital debris (MMOD) impact. A novel area of research proposes using truss-based cellular architected materials for improved impact resistance in spacecraft. This new shield concept requires accurate modelling of beam-to-beam contact to assess the metamaterial's performance during collisions. Capturing contact and fracture is integral to modelling impact shields, with this thesis focusing on the issue of contact.

The primary objectives are to derive a suitable DCR-based beam-to-beam contact formulation, verify it with benchmark problems, and apply it to a compressed architected material sample. A compression test is used as a surrogate for analyzing low-velocity impact, serving as a proof-of-concept in advancing the understanding of architected materials under impact loads. Crucially, the research aims to identify the contact stiffening effect — a phenomenon where the compressive load increases following the initial collapse of the structure due to the emergent bulk behaviour of struts coming into contact at large compressive displacements.

The literature review provides a comprehensive overview of existing finite element method (FEM) frameworks for modelling beam-to-beam contact and highlights the requirements of the novel contact model, particularly in its application to truss-based architected materials.

The research methodology involves a thorough derivation of the proposed DCR formulation for beam-to-beam contact. Additionally, the procedure for modelling various scenarios involving a body-centred cubic (BCC)-inspired architected material configurations using the DCR-integrated finite element framework is described. Here, the potential limitations of the assumptions taken in modelling these scenarios are also discussed.

The beam-to-beam DCR formulation was tested in two verification cases to verify its accuracy and reliability. The first verification case is meant to emulate a particle collision, demonstrating that the post-impact kinematic values conserve momentum and agree with analytical predictions. The second verification case involves exciting a cantilever beam with an impact event and studying the beam's response compared to the corresponding analytical solution. Lastly, a standard penalty approach is applied to the same scenario to highlight its susceptibility to the chosen penalty parameter. These steps ensure that the novel formulation is both theoretically sound and practically viable.

The applications in this study include three unique scenarios involving architected cellular materials. The first application is a simple test involving a slender beam impacting a unit cell, intended to isolate the response of the structure to two sequential contact events. The second involves contact between two identical unit cells to simulate a more involved impact scenario with numerous contact events. The last, and most important application, simulates the compression of an architected material comprised of eight unit cells subjected to a compressive load in order to capture the contact stiffening effect. The results of these three applications are documented and discussed in detail, revealing a promising performance of the DCR-enabled contact model. Some shortcomings in the results are nevertheless present, most notably the implementation of pin joints in the lattice structures.

The application of the DCR model successfully preserved total system momentum and accurately modelled large deformations in the struts during beam-lattice and lattice-lattice collisions, despite using idealized pin joints. The compression of a 2x2x2 insideBCC lattice demonstrated the onset of the contact stiffening effect, although the magnitude did not fully match literature due to time constraints limiting the compression to 32%.

Finally, this thesis lays a solid foundation for future research by identifying necessary enhancements, such as the use of rigid joints in modelling beam lattices, the ability to capture plasticity, and parallel implementation of the finite element formulation, among others. The insights gained from this research are particularly valuable for the development of next-generation HVI shields, as accurate beam-to-beam contact modelling is crucial during the design stage. Moreover, this model is applicable to any structure made up of slender beams undergoing large deformations, thereby vastly expanding the space of future applications for this contact model. Overall, the thesis meets its primary objectives and provides valuable directions for future improvements in beam-to-beam contact modelling.

Contents

List of Figures

List of Tables

1

Introduction

Innovations in additive manufacturing have revolutionized material design, enabling the creation of architected materials with exceptional properties. These materials address limitations of conventional materials by incorporating features like cellular structures that promote bulk-level properties.

1.1. Architected cellular materials for impact absorption

Architected cellular materials, in particular, have garnered significant attention due to their unique ability to combine lightweight design with high performance. They are often inspired by natural structures and offer the flexibility to achieve specific mechanical properties, making them suitable for diverse applications. A notable such application is in the aerospace industry, where lightweight, impact-absorbing structures are essential. Traditional materials often fall short in meeting the stringent requirements for impact resistance and weight reduction. Architected cellular materials, such as foams and honeycombs, have long been used to design lightweight structures capable of absorbing impact energy. Recent advancements have focused on truss-based lattices, which offer enhanced impact absorption capabilities due to their unique structural configurations.

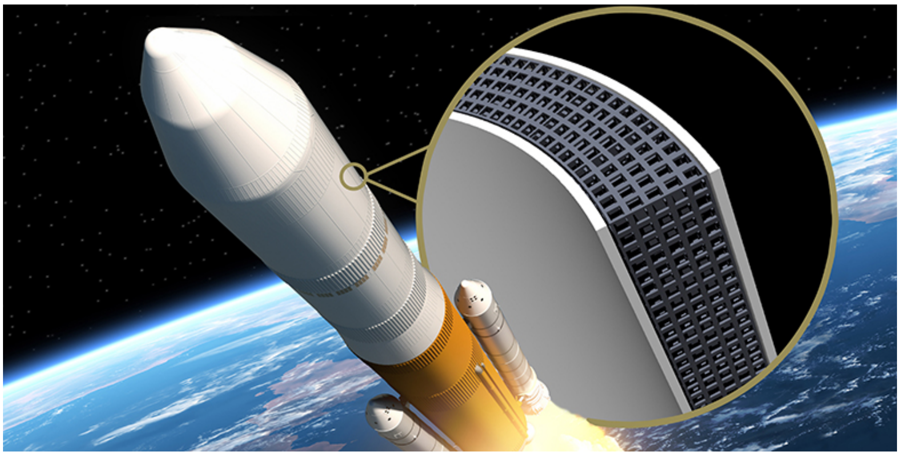

Figure 1.1: Artistic rendering of a vibration-absorbing lattice aboard a launch system by J. Tse

Architected cellular materials show promise for space applications, particularly as MMOD shields. The ever-increasing presence of space debris in low Earth orbit (LEO) poses a significant danger to spacecraft, which are threatened by HVIs at speeds in excess of 6 km/s [2]. NASA research has demonstrated that sandwich structures with open-cell foam cores outperform traditional honeycomb cores [3]. HVI tests support these findings, demonstrating the effectiveness of foam-cored panels, as illustrated in Figure 1.2 below.

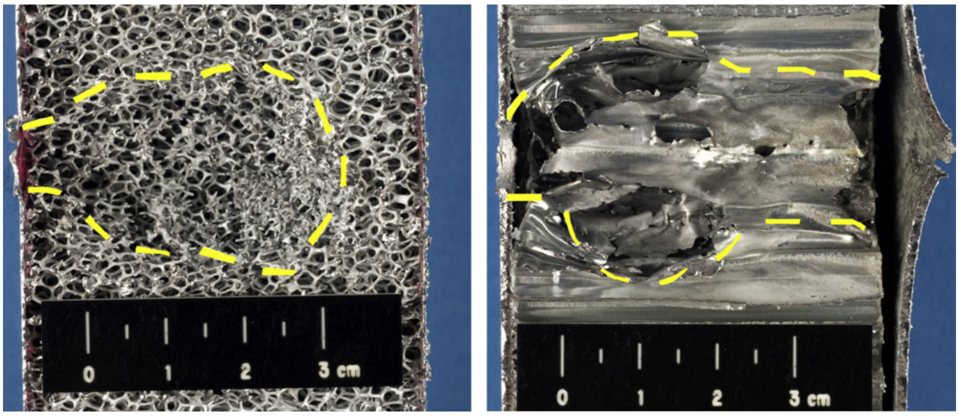

Figure 1.2: Sectioned side-view comparison of damages in open-cell foam core (left) and honeycomb core (right) sandwich panel structures impacted by 3.6 mm Al-spheres at 6.47 ± 0.27 km/s [3]

Another example of architected cellular materials applied to HVI is the study conducted by Voillat *et al.*, which tested two lattice configurations made from cast AlSi12 against 2 mm-diameter aluminum projectiles at velocities of 6.7-7.0 km/s [4]. The two configurations included a stochastic open-cell metallic foam and a periodic diamond cubic structure (see Figure 1.4). The results revealed poor performance of the periodic lattice in impact protection, whereas the stochastic foam successfully stopped debris, with performance comparable to that of a simple Whipple shield (see Figure 1.3). The authors concluded that stochastic foams have potential as sandwich panel cores for space applications, particularly those with finer pores [4].

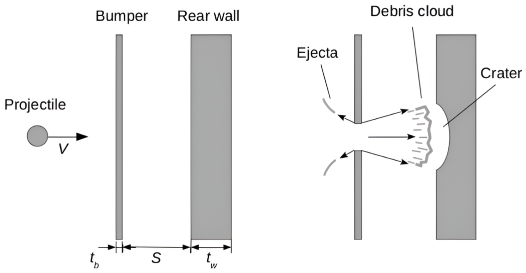

Figure 1.3: Schematic of a simple Whipple shield configuration (left) and a HVI impact scenario (right) [4]

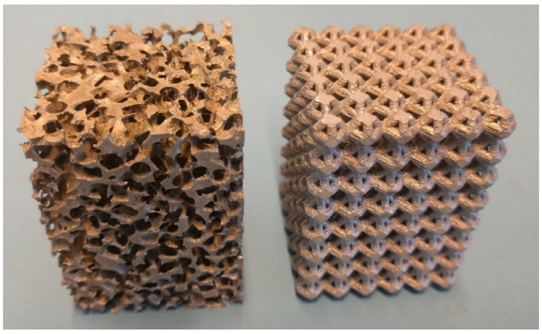

Figure 1.4: Cast AlSi12 lattice sample: stochastic foam (left) and periodic diamond cubic (right) [4]

A third study, also based on modelling aluminum foam lattices for space applications in shielding against HVI, is presented by Zhang *et al.* [5]. The authors propose a smoothed particle hydrodynamics (SPH) numerical framework for modelling HVI in aluminum foam sandwich panels whose core structure is generated via numerical VORONOI tesselation techniques. Their findings confirmed that the foam structure prevails over a homogeneous aluminum panel in terms of ballistic performance, crediting the foam structure's superior ability to diffuse pressure waves [5]. Figure 1.5 below depicts the numerical results as compared to the benchmark test of a 2 mm aluminum projectile propelled at 6.85 km/s at a 25.4 mm thick aluminum foam panel.

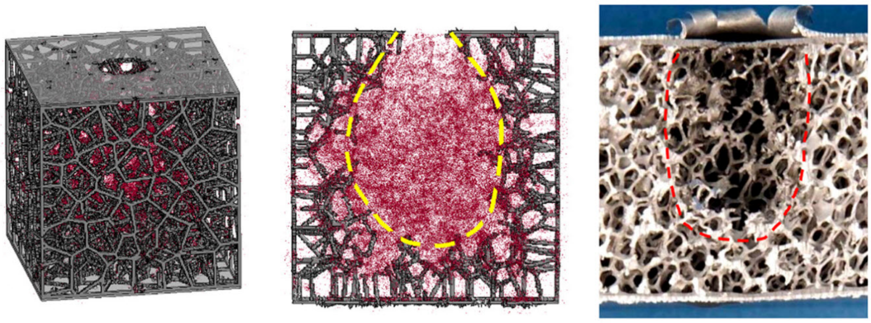

Figure 1.5: Comparison of results in an isometric view (left), numerical results in a vertical section view (middle), and physical test results (right) [5]

While aerospace applications represent a significant use-case for architected materials, it is important to acknowledge that numerous other applications have also been explored. Notably, the use of softer lattices as auxetic materials and phononic crystals has been extensively researched in recent years. An overview of these non-aerospace applications is presented in Appendix A. Although these topics are a corollary to the main focus of this thesis, they are nonetheless worthy of review.

1.2. The role of computational modelling

The vast design space of architected materials necessitates a focused research approach. This study thus centres on leveraging computational mechanics for their design and analysis. Numerical simulations are a critical phase in the synthesis and optimization of new materials for engineering applications, as they can be used to supplement mechanical testing — particularly destructive testing. This approach can save time and resources while allowing for exploration of unconventional configurations.

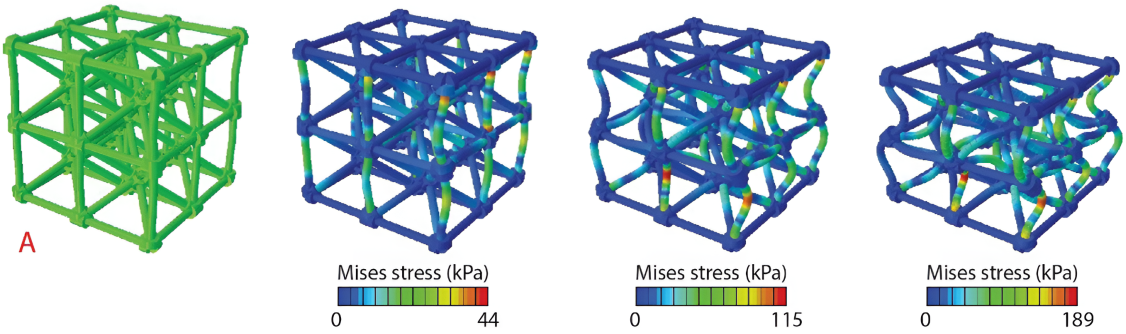

Figure 1.6: Nonlinear buckling analysis for compression of a sample BCC lattice [6]

Within the realm of computational mechanics, this thesis delves into the sub-field of contact mechanics, specifically its role in modelling truss-based architected materials in their large deformation regime. Understanding the interaction between truss members under compression is vital for accurate performance prediction. Despite findings that indicate stochastic open-cell foam lattices offer superior performance in mitigating high-velocity impact (HVI) [4], it is crucial to first establish a use case with simpler periodic structures. This is because generating and analyzing stochastic cells involves its own complex research challenges. This research thus narrows its focus to numerically modelling a variant of the BCC lattice structure called the insideBCC (see Figure 1.7), known for its well-defined geometry and relevance in natural and engineered materials (see Subsection 2.1.1 for additional information on crystal-inspired architected materials).

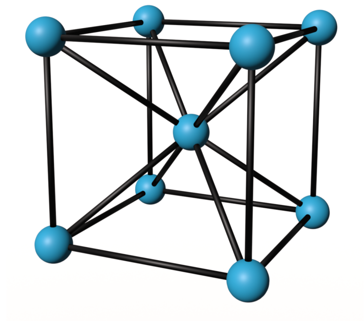

Figure 1.7: Selected cell configuration: the insideBCC structure

The aim of this research is to improve the effectiveness of numerical tools for modelling these materials, particularly in understanding their post-buckling behaviour and the influence of strut-strut contact, whilst maintaining a desirable trade-off with accuracy. However, achieving high-fidelity requires balancing accuracy with computational feasibility. This necessitates an informed selection of a suitable beam model for this study.

1.3. Challenges in high-fidelity modelling of architected materials

In the realm of architected materials, particularly those designed as impact-absorbing structures, understanding and modelling contact interactions between lattice struts is crucial. Accurate simulation of these materials requires a detailed understanding of how lattice members, or *struts*, interact during impact and following structural collapse, hence emphasizing the importance of contact mechanics in predicting their performance. A detailed discussion of the present corpus of work on modelling architected materials is provided in Section 2.1 of Chapter 2. The underlying challenges in the state-of-the-art can be distilled to one prevailing issue — capturing contact.

Modelling contact interactions in the context of FEM poses significant challenges. Beam elements, which are often used for their computational efficiency, struggle with accurately capturing beam-to-beam contact, which is vital for simulating the complex mechanical behaviour of lattice structures. While solid elements can model contact interactions more precisely, they come with increased computational costs, making them impractical for large-scale simulations [7] [8]. Additionally, approaches like homogenized unit cells, which simplify modelling by averaging material properties, fail to capture the nuances of contact mechanics due to their lack of spatial resolution. Therefore, there is a pressing need for advanced modelling techniques that integrate contact mechanics within a beam element framework, allowing for accurate and computationally feasible simulations of lattice structures under various loading conditions [9]. Many of the cited works on compressed lattices contrast their numerical results with physical testing [7] [8] [9] [10]. A key feature of these tests, which is not adequately captured in the numerical counterpart, is the presence of a phenomenon which will hereinafter be referred to as the *contact stiffening effect*. This can be seen in Figure 1.8 below when strains exceed a value of 0.25, with an upward trending load curve.

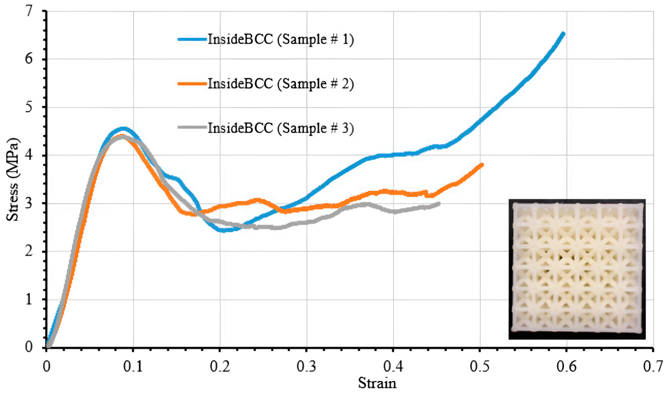

Figure 1.8: Stress–strain curves for three insideBCC specimens under uni-axial compression [10]

The contact stiffening effect is the primary focus of this study, where the requisite theory for understanding the phenomenon and the appropriate methods of modelling it shall be covered in detail. This research seeks to develop a more efficient modelling approach: a contact-integrated FEM model using beam elements that can overcome the limitations of conventional LAGRANGE multiplier or penalty methods. Such an approach would enable the accurate and efficient modelling of compressive failure in architected cellular materials.

In more practical terms, the following research question is posed:

Research question

How can a contact-integrated finite element model be used to enhance simulations involving large compressive deformations in an architected cellular material comprised of slender struts?

1.4. Research approach

Addressing this question would bridge the gap between high-fidelity but expensive solid element models and less accurate but efficient beam element models. This will ultimately advance the field of computational contact mechanics and enable computational design of architected materials for impact absorption [11].

To answer the research question, this thesis will address the following sub-tasks:

(1) Derive a beam-to-beam contact algorithm inspired by a momentum-based method and the point-to-point penalty formulation [1] [12].
(2) Verify the method using simple impact tests.
(3) Apply the novel contact formulation to an idealized architected material cell in three applications, with the final one evaluating the contact stiffening effect in a compressed insideBCC sample.

2

Literature review

This chapter comprises three principal sections. First, Section 2.1 summarizes the current body of work on truss-based architected materials and highlights the gap in modelling the contact stiffening effect. Second, Section 2.2 provides the necessary theoretical context for evaluating various 1D beam models and justifies the choice of the torsion-free KIRCHHOFF–LOVE variant. Thirdly, Section 2.3 explores the canonical methods of modelling contact in FEM frameworks.

Building on this foundational framework, the literature review chapter aims to present all relevant ideas to directly support the ultimate objective: capturing the contact stiffening effect by modelling a compression test of an insideBCC architected material.

2.1. Architected materials

Advancements in additive manufacturing have significantly transformed material design, providing innovative methods for developing materials with unique and superior properties. So called *white-spaces* left in the property space by conventional monolithic materials can be filled by tailoring hybrid materials (see Figure 2.1) [13]. This ability to leverage distinct properties has long been used in the realm of aerospace design, for instance, with composite or sandwich structures. Another highly useful class of hybrid configurations are *architected cellular materials*. This subclass of hybrid materials consists of repeating unit cells that possess a distinct local structure. These hierarchical unit cells can take many forms, often stemming from bioinspired structures [14] or from crystallography [9]. Architected cellular materials inspired by crystal lattice structures are of noted interest, due to their extensively documented structural properties, manufacturability, and relative simplicity [15].

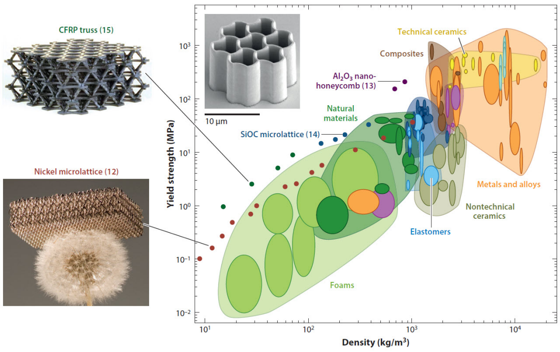

Figure 2.1: Instances of white-space materials achieved through the manipulation of cellular architectures [13]

The high degree of tailorability afforded by architected materials and the numerous potential cellular configurations mean that the applications of such metamaterials are vast. A particular application of interest in the context of aerospace and defence is the design of lightweight impact-absorbing structures for impulsive loads. To protect against the threat of projectile impact, the structure must be capable of undergoing a large volume decrease at constant pressure — a requirement not satisfied by dense or nearly incompressible solids [11]. Recent investigations have explored various avenues concerning truss lattices, including the impact of artificial grain boundaries in an architected material [9], the use of hollow truss members [11] [16], and the integration of metallic microlattices [17]. These research directions aim to harness the mechanical properties of architected materials to enhance impact absorption capabilities.

2.1.1. Crystal-inspired lattices

To present a more coherent narrative on architected materials, this study will focus on a specific lattice cell configuration, which will be examined in detail throughout the remainder of the research. To justify the choice of a particular cell configuration, consideration turns to the related field of solid-state physics known as *crystallography*. The study of crystals is particularly relevant due to the ubiquity of crystal structures in nature. For this study, a focus is placed on *anisotropic* and *periodically homogeneous* lattices, which allow for the characterization of crystal structures using their *unit cell*. A unit cell is a 3D structure that, when periodically translated through linear mapping, forms a truss-like structure. Additionally, the discussion is further narrowed to *orthorhombic* BRAVAIS *lattices*, as their geometric properties are well-documented and extensively studied [18].

Among the reduced set of configurations, there remains an infinite number of possible lattices to choose from. Thus, as a final filtering step, the BCC configuration is selected as the preferred crystal structure. Referring to Figure 2.2, the BCC is characterized has having $a = b = c$, with a point in the centre of the cube.

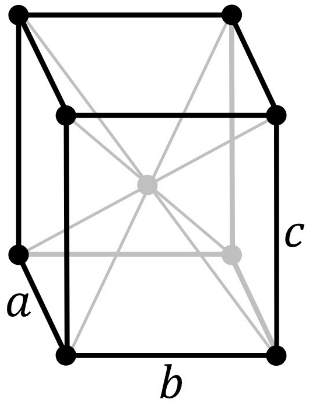

Figure 2.2: Body-centred orthorhombic BRAVAIS unit cell

In crystals, the nodes of the unit cell (shown as points in Figure 2.2), represent the arrangements of atoms in the material and the lines are mere geometric aids in visualizing the lattice. In the case of architected materials, however, these lines precisely coincide with the locations of the struts in the lattice. Therefore, a distinction can be made between a true BCC and the so-called insideBCC, which is characterized as the superposition of the BCC and the simple cubic structure. The difference between the aforementioned configurations is depicted in Figure 2.3 and Figure 2.4 below.

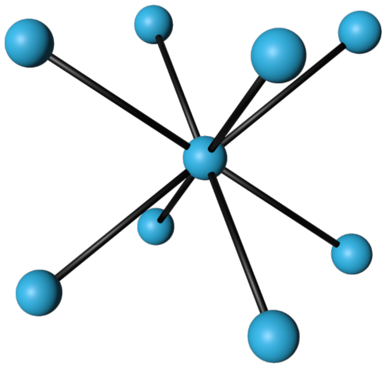

Figure 2.3: BCC unit cell

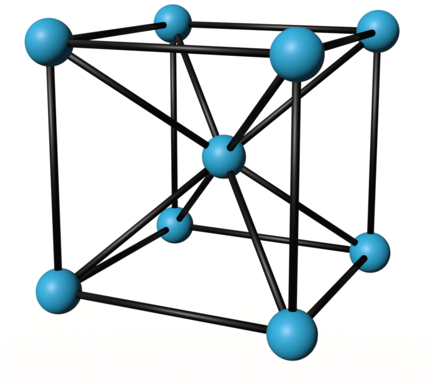

Figure 2.4: insideBCC unit cell

Unlike crystal structures which occur at the microscale in nature, architected material applications in this study are considered only at the macroscale. Considering the downstream application as a compressive test, it becomes evident that the insideBCC unit cell is favourable, due to the added support of the vertical struts. While other crystal structures may have potential in different applications, this thesis focuses on conducting an exhaustive study of an architected material for a single configuration. Constructing a truss-lattice architected material from an insideBCC unit cell involves simply replacing the spheres depicted in Figure 2.4 with joints and assembling unit cells into a *supercell* — a cubic structure comprised of smaller unit cells. In doing so, a three-dimensional truss resembling the atomic structure of BCC crystals can be effectively generated at the macroscopic scale.

2.1.2. BCC truss-based architected materials: state-of-the-art

Having selected a suitable crystal-inspired lattice configuration, the literature on these architected materials may now be explored in greater detail. A notable application of a BCC configuration is the *metallic microlattice*. In their paper, Gümrük and Mines investigate the mechanical properties of 316L stainless steel microlattice structures created via selective laser melting (SLM) [8]. Their research combines theoretical, numerical, and experimental approaches to understanding the static compression behaviour of said microlattices, focusing on the effects of strut connections. The modelling framework in [8] captures shear and bending via a Timoshenko beam model (see Subsection 2.2.2), in addition to plasticity and nonlinear beam buckling. A visual comparison between the experimental and beam model numerical results is shown in Figure 2.5 below.

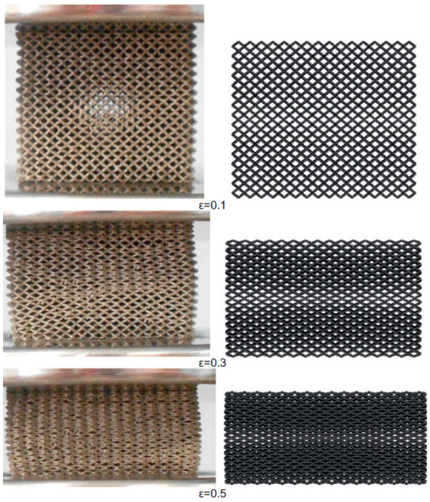

Figure 2.5: Experimental and beam model compression developing stages [8]

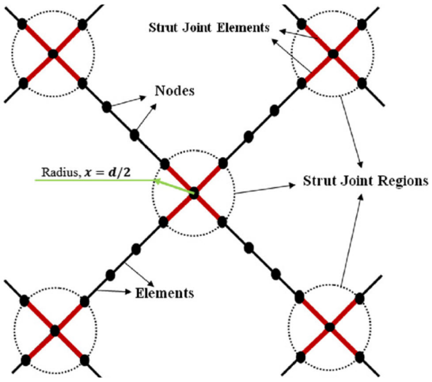

Figure 2.6: Strut joint region convention used by Gümrük and Mines [8]

To tackle the issue of strut-joint complexities that was originally discussed in [19], the authors employ a method of locally adapting the stiffness of beam elements in the vicinity of joints. To overcome the added stiffness to the structure that is to be expected at these joints, stiffness is increased by 50% in the region $\frac{d}{2}$ from the joint's centre, where d is the diameter of the strut. This is shown schematically in Figure 2.6.

This approach yielded accurate results, with the numerical bulk stiffness of the structure closely resembling the experimental results. A comparison of their results is shown in Figure 2.7.

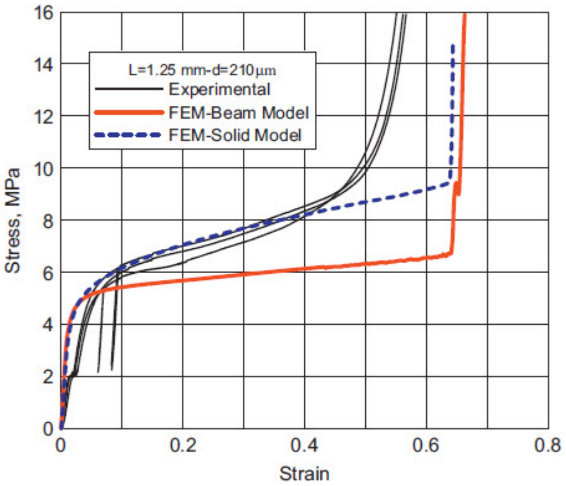

Figure 2.7: Comparisons of numerical and experimental compression results for microlattice blocks [8]

From Figure 2.7, it is evident that the solid element model was more effective at modelling bulk behaviour than the 1D beam model. This discrepancy was identified by Mines as being caused by the collapse of struts and the onset of plasticity [15].

In addition to the contributions to metallic microlattices in [8] and [19], excellent research has also been done for soft lattice materials, most notably by Jamshidian *et al.* [6] for elastomers, and by Alwattar [10] and Pham *et al.* [9] for high-modulus polymers.

Jamshidian *et al.* investigate the nonlinear buckling behaviour and macroscale constitutive modelling of soft beam-lattice structures made of hyperelastic materials. A central focus of their research is on large elastic deformations and buckling that occurs under compression. Using 3D solid elements, they numerically performed a primary linear buckling analysis to incorporate geometric imperfections, followed by a nonlinear post-buckling analysis. This computational model was validated against experimental data from 3D-printed lattice structures subjected to tensile and compressive tests. The results reveal the critical role of buckling and post-buckling responses in the mechanical behaviour of these metamaterials. [6]

A summary of the relevant findings from Jamshidian *et al.* is illustrated in Figure 2.8 for a beam-lattice block comprised of eight insideBCC unit cells under uni-axial compression. Figure 2.8 suggests strong agreement between experiment and simulation, especially when joint stiffening is considered in the finite element model.

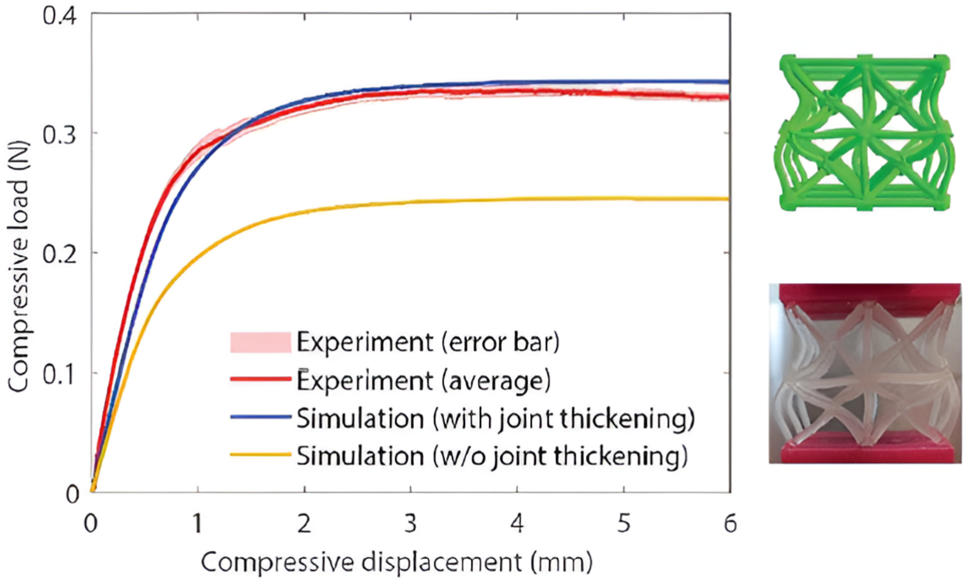

Figure 2.8: Comparison between experimental and simulation results for the nonlinear buckling load-displacement response of a buckling-dominated lattice structure comprised of an insideBCC unit cell [6]

Although the study by Alwattar and Mian only simulates within the linear regime of the material, their experimental tests provide some additional insights, particularly regarding the compression of insideBCC samples until full collapse. These results, presented below in Figure 2.9, reveal an important feature not captured in any of the papers discussed thus far: the stiffening effect at high strains exhibited after the initial collapse of the cells. This bulk phenomenon is attributed to self-contact between the struts [10].

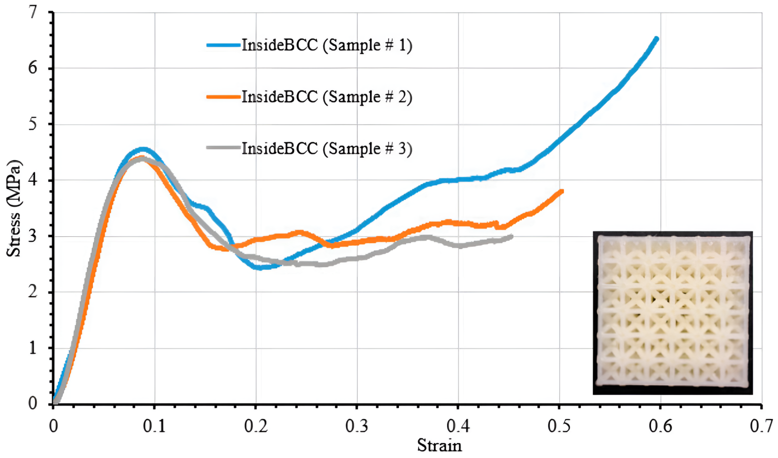

Figure 2.9: Stress–strain curves for three insideBCC specimens under uni-axial compression [10]

As a final example of compressed truss-based metamaterials, the work of Pham *et al.* further elucidates the stiffening effect due to strut self-contact. While the goal of their paper — to mimic the metallurgical concepts of grain boundaries and precipitate hardening in a cellular architected material — falls outside the scope of this thesis, part of their results are incredibly relevant. Most notably, they capture contact in their experimental plots. However, the finite element results at the point of full collapse are not reported, and the stiffening effect observed in experimentation is not reproduced by simulations. Figure 2.10 Shows the characteristic contact hardening effect when the lattice is fully collapsed. [9]

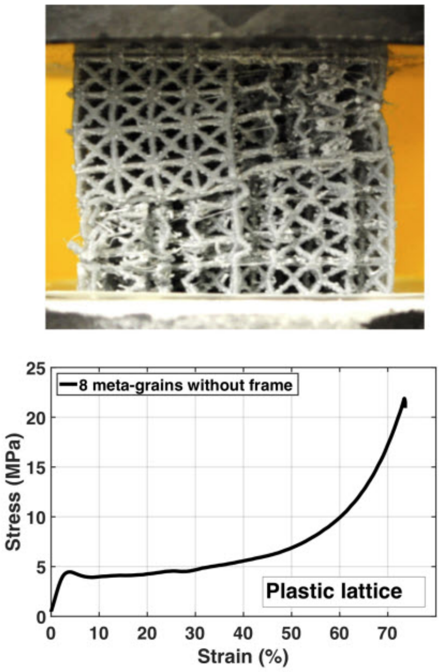

Figure 2.10: Test results from an 8 meta-grain insideBCC polymer block under uni-axial compression (top) and plotted stress-strain response of the block (bottom) [9]

2.1.3. Conclusions on the architected materials literature review

Despite the extensive research on simulating the mechanical behaviour of compressed architected materials, significant gaps remain. Various studies have successfully addressed specific aspects of the problem. For example, Jamshidian *et al.* have made notable advancements in understanding the post-buckling response of soft lattice materials, particularly in hyperelastic materials [6]. Similarly, Gümrük and Mines have effectively modelled the influence of joint stiffening in metallic microlattices using a TIMOSHENKO beam model to capture shear and bending effects, along with plasticity and nonlinear buckling [8].

However, a critical limitation persists in the accurate simulation of beam-to-beam contact interactions using beam elements. Most of the cited studies in this section predominantly opt for solid elements to model the complex mechanical behaviour of lattice structures. This choice often stems from the challenges of incorporating contact mechanics within beam element models, which are crucial for simulating compressive failure accurately.

While solid elements can effectively capture contact interactions in some cases, they significantly increase computational costs, making them less practical for large-scale simulations. The homogenized cells proposed by Labeas and Ptochos also naturally fail to capture contact by virtue of smearing structural properties [7]. The need for a more efficient and accurate modelling approach is evident, particularly one that integrates contact mechanics within a beam element framework. This would allow for the simulation of compressive failure in architected cellular materials comprised of lattice struts, addressing the limitations seen in current models.

Appendix A provides a supplementary discussion on other applications for architected materials. While not directly related to the research objective, this exposition provides interesting tangential insights.

2.2. Overview of beam theories

The concept of a beam element, integral to structural analysis, is specifically engineered to characterize the motion and deformation of slender bodies. The slenderness distinction allows for reductions from three-dimensional continua to its one-dimensional COSSERAT counterpart [20]. Initially motivated by the accessibility of analytical solutions in the time of EULER and LOVE, contemporary applications rely on the efficiency of numerical methods, enabling investigations into complex phenomena involving nonlinearities, be they geometric, material, contact-related, or otherwise. The evolution of beam theory, from EULER to REISSNER and SIMO, introduced additional deformation measures, paving the way for a various *geometrically exact* beam formulations. This section will serve as a historically motivated presentation of the major advancements in beam theory up until the present day. Subsequent subsections will delve into the mathematical descriptions of each theory, as well as their most notable features.

A note on terminology

Induced beam theories are reduced 1D continuum theories derived from 3D continuum mechanics, describing slender body deformations through integration of 3D stress measures over beam cross-sections. *Intrinsic* beam theories directly postulate 1D resultant quantities but are decoupled from 3D continuum mechanics, relying on experimentally determined constitutive constants. *Semi-induced* beam theories strike a balance by postulating the constitutive law while deriving kinetic and kinematic relations consistently from 3D theory. [20]

2.2.1. Euler-Bernoulli beam

The review of useful beam theories begins with the simplest case — the EULER-BERNOULLI beam. Also called, the *thin beam* or *shear rigid beam*, the EULER-BERNOULLI beam gets its namesake in part from the contributions of DANIEL BERNOULLI, who provided the first analytical solution to the bending cantilever problem in the 18th century [21]. His formulation, which assumes small deformations ($ds \approx dx$), is written as:

$$EI\frac{d^2y}{dx^2} = Wx \tag{2.1}$$

For which a cubic equation describing the lateral deformation under the load W can be obtained by simple integration. It is important to note, however, that several other crucial assumptions are made for the EULER-BERNOULLI model. In addition to the assumption of small deformations, this model is applicable solely to initially straight beams and does not account for longitudinal or torsional deformation. Furthermore, it assumes a constant and shear-rigid cross-sectional area [22]. BERNOULLI's hypothesis states that the cross-section of the beam remains perpendicular to the centreline of the beam, even in its deformed state, as shown in Figure 2.11.

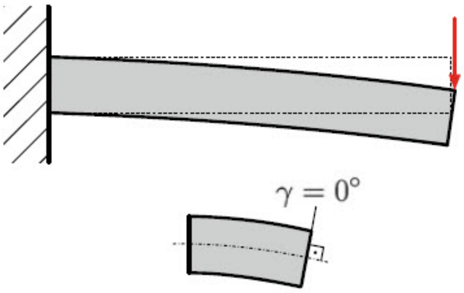

Figure 2.11: Deformation of a bending beam under the shear-rigid assumption [22]

For an EULER-BERNOULLI beam, deformation results from linearly distributed normal forces, leading to maximum tension or compression at the top or bottom face, respectively, with a neutral axis at the centre for symmetric cross-sections.

The EULER-BERNOULLI beam model offers a simplified yet powerful approach for analyzing initially straight beams under various loading conditions. It simplifies the three-dimensional problem into a one-dimensional framework, facilitating straightforward analytical analysis However, it is based on the assumption of linear elastic material behaviour and neglects shear deformation effects, limiting its applicability to long, slender beams with small deflections. Despite these limitations, the EULER-BERNOULLI beam model remains a versatile and indispensable tool for structural analysis and design. Its inability to capture buckling phenomena and its irreconcilability with contact scenarios disqualify it as a suitable model for this study.

2.2.2. Timoshenko beam

The primary feature that distinguishes the TIMOSHENKO beam from its EULER-BERNOULLI predecessor is the inclusion of shear influence. Whereas the BERNOULLI hypothesis precluded the deformed configuration from breaking its orthogonality with the neutral axis, the TIMOSHENKO formulation admits cross-sectional warping through the shear mechanism. This assumption thus necessitates a correction factor to account for the shear contribution, as depicted in xy-plane deformation example of Figure 2.12 below.

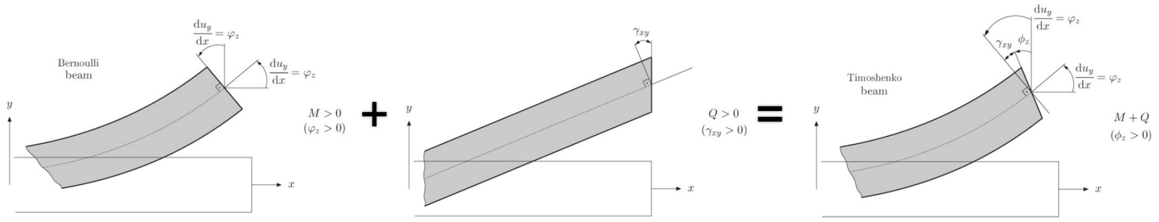

Figure 2.12: Superposition of the EULER-BERNOULLI beam and the shear deformation to produce a TIMOSHENKO beam [22]

TIMOSHENKO beam theory offers advantages in accurately modelling shear deformation effects — a feature not present in the EULER-BERNOULLI beam. In practice, this allows for higher accuracy when modelling high-frequency dynamic loading, which is highly sensitive to the coupling of deformation modes in the beam [22]. Naturally, the complexity and higher computational costs of the TIMOSHENKO beam compared to the EULER-BERNOULLI beam theory pose limitations. Like EULER-BERNOULLI, the TIMOSHENKO model is also constrained to analyses involving slender and initially straight beams undergoing small deformations, thus rendering it ineffective for this study.

2.2.3. Simo-Reissner beam

All formulae in this section have been adapted from Meier *et al.*'s comparative study on geometrically exact beams [20].

KIRCHHOFF introduced a significant advancement in beam theory in 1859, leading to the formulation bearing his name. This formulation, based on the BERNOULLI hypothesis and EULER's work, is notable for its ability to handle beams with non-straight initial configurations as well as large three-dimensional deformations, including bending and torsion [23]. LOVE later extended this theory in 1944 to incorporate the effects of small axial tension [24].

This section introduces the concept of the *geometrically exact beam*. REISSNER made significant contributions to the beam theory established by his predecessors by introducing two additional deformation measures to account for shear deformation [25][26]. REISSNER's work was later extended by SIMO [27] to provide a more consistent formulation based on the 3D continuum theory, leading to what is now known as the SIMO–REISSNER beam theory.

The term *geometrically exact beam* is defined according to SIMO's principles. Specifically, a beam theory is considered geometrically exact if "the relationships between the configuration and the strain measures are consistent with the virtual work principle and the equilibrium equations at a deformed state regardless of the magnitude of displacements, rotations and strains" [28]. This definition implies that the theory remains valid for large deformations, introducing the notion of *finite-strain*. In this context, finite-strain beams are those where large deformations and rotations are considered without simplifying assumptions about their magnitude [28].

Simo-Reissner theory assumes rigid cross-sections, requiring six degrees of freedom to describe the position and orientation of the cross-sections uniquely. This makes the beam theory a one-dimensional Cosserat continuum derived from a three-dimensional Boltzmann continuum [28].

Kinematics
This subsection aims to briefly cover the pertinent details of the kinematics as they were described by Reissner [25][26], Simo [27], Vu-Quoc [29], and later summarized by Meier *et al.* [20]. Key kinematic quantities for the Simo-Reissner beam formulation is presented below in Figure 2.13.

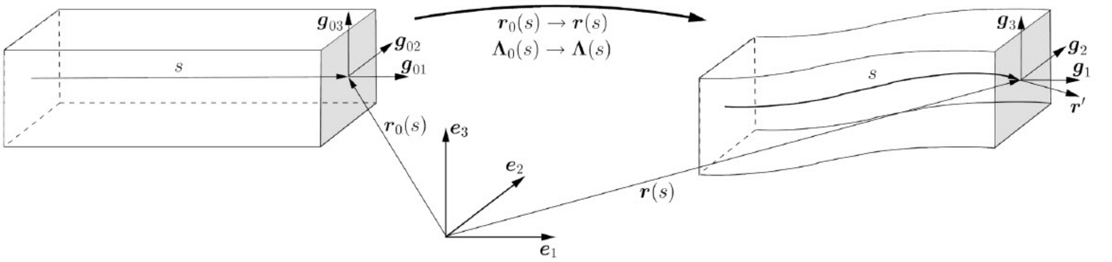

Figure 2.13: Kinematic quantities defining the initial and deformed configuration of the Simo-Reissner beam [20]

Initially, the beam's centreline, represented by the space curve $s \mapsto \boldsymbol{r}_0(s) \in \mathbb{R}^3$, connects the centroids of the cross-sections. Here, $s \in [0, l] := \Omega_l \subset \mathbb{R}$ serves as the arc-length parametrization, where $l \in \mathbb{R}$ is the beam's length in the initial configuration. The description of the initial state includes a set of right-handed orthonormal triads denoted by $s \mapsto \boldsymbol{g}_{01}(s), \boldsymbol{g}_{02}(s), \boldsymbol{g}_{03}(s) \in \mathbb{R}^3$, also known as *material triads*. These are affixed to the undeformable beam cross-sections, per the Bernoulli hypothesis. Here, $\boldsymbol{g}_{01}(s) = \boldsymbol{r}_0'(s)$ denotes the unit tangential vector to the initial centreline, while $\boldsymbol{g}_{02}(s)$ and $\boldsymbol{g}_{03}(s)$ align with the principal axes of inertia of the cross-section at s [20].

Nota bene: Some of the following derivations make use of the notation $SO(3)$, which represents the group of all rotations in the three-dimensional space with which we engineers are familiar. There is, however, a rich mathematical motivation to this formalism that unfortunately falls out of scope for this study. For the curious reader, the author recommends Hall's introductory text on Lie algebra [30].

The rotation from the global frame $\boldsymbol{e}_i$ on the initial frame $\boldsymbol{g}_{0i}$ can be described by the orthogonal transformation $s \mapsto \boldsymbol{\Lambda}_0(s) \in SO(3)$, which gives $s \mapsto C_0 := (\boldsymbol{r}_0(s), \boldsymbol{\Lambda}_0(\boldsymbol{\Psi}_0(s))) \in \mathbb{R}^3 \times SO(3)$. Similarly, for the deformed configuration at time $t \in \mathbb{R}$, $s, t \mapsto C := (\boldsymbol{r}(s,t), \boldsymbol{\Lambda}(\boldsymbol{\Psi}(s,t))) \in \mathbb{R}^3 \times SO(3)$. The orthogonal transformation $\boldsymbol{\Lambda}(\boldsymbol{\Psi}(s,t))$ maps from the global to the local frame, with $\boldsymbol{\Psi}$ representing the rotation vector. An important feature to highlight in the Simo-Reissner formulation is that, in the deformed configuration, base vector $\boldsymbol{g}_1(s,t) := \boldsymbol{g}_2(s,t) \times \boldsymbol{g}_3(s,t)$ is no longer necessarily tangential to the beam's deformed centreline.

Weak form
The strong form of the mechanical equilibrium equations for the Simo-Reissner beam formulation are written as [20]:

$$\boldsymbol{f}' + \tilde{\boldsymbol{f}} + \boldsymbol{f}_\rho = \boldsymbol{0} \tag{2.2a}$$

$$\boldsymbol{m}' + \boldsymbol{r}' \times \boldsymbol{f} + \tilde{\boldsymbol{m}} + \boldsymbol{m}_\rho = \boldsymbol{0} \tag{2.2b}$$

where quantities $\tilde{\boldsymbol{f}}$ and $\tilde{\boldsymbol{m}}$ denote external distributed forces and moments per unit length, respectively. $\boldsymbol{f}_\rho$ and $\boldsymbol{m}_\rho$ represent the forces and moments resulting from inertial effects, while $\boldsymbol{f}$ and $\boldsymbol{m}$ are the force and moment stresses acting on the beam's cross-sectional area. Standard variational techniques lead to the introduction of $\delta\boldsymbol{r}(s) \in \mathbb{R}^3$ as virtual displacements and $\delta\boldsymbol{\theta}(s) \in \mathbb{R}^3$ as virtual rotations. Applying the principle of virtual work to Equation 2.2, and then integrating by parts yields the following spatial weak form [20]:

$$\begin{aligned}&\int_0^l \left(\delta\boldsymbol{\theta}'^T\boldsymbol{m} + (\delta\boldsymbol{r}' - \delta\boldsymbol{\theta}\times\boldsymbol{r}')^T\boldsymbol{f} - \delta\boldsymbol{\theta}^T(\tilde{\boldsymbol{m}} + \boldsymbol{m}_\rho) - \delta\boldsymbol{r}^T(\tilde{\boldsymbol{f}} + \boldsymbol{f}_\rho)\right)\mathrm{d}s\\ &- \left[\delta\boldsymbol{r}^T\bar{\boldsymbol{f}}\right]_{\Gamma_\sigma} - \left[\delta\boldsymbol{\theta}^T\bar{\boldsymbol{m}}\right]_{\Gamma_\sigma} \doteq 0\end{aligned} \tag{2.3}$$

where $\bar{\boldsymbol{f}}$ and $\bar{\boldsymbol{m}}$ denote the external forces and moments at the NEUMANN boundary Γ_σ of a beam with length l. The triad $\boldsymbol{\Lambda}$ can then be used to write the objective spatial deformations [20]:

$$\boldsymbol{\gamma} = \boldsymbol{r}' - \boldsymbol{g}_1 \tag{2.4a}$$

$$\boldsymbol{\omega} = k - \boldsymbol{\Lambda}\boldsymbol{\Lambda}_0^T k_0 \tag{2.4b}$$

where k is the spatial curvature and subscript 0 denotes the initial configuration. From the objective deformations in Equation 2.4, the corresponding objective variations can be written as follows [20]:

$$\delta_0\boldsymbol{\gamma} = \delta\boldsymbol{r}' - \delta\boldsymbol{\theta}\times\boldsymbol{r}' \tag{2.5a}$$

$$\delta_0\boldsymbol{\omega} = \delta\boldsymbol{\theta}' \tag{2.5b}$$

The material counterparts of equations (2.4) and (2.5) can equivalently be derived with the use of material stress resultants $\boldsymbol{F} := \boldsymbol{\Lambda}^T\boldsymbol{f}$ and $\boldsymbol{M} := \boldsymbol{\Lambda}^T\boldsymbol{m}$. It is important to note that material (or LAGRANGIAN) quantities will be denoted by upper case Latin and Greek letters, while spatial (or EULERIAN) will be denoted by lower case letters. Thus, the objective material deformations are given by [20]:

$$\boldsymbol{\Gamma} = \boldsymbol{\Lambda}^T\boldsymbol{r}' - \boldsymbol{E}_1 \tag{2.6a}$$

$$\boldsymbol{\Omega} = \boldsymbol{K} - \boldsymbol{K}_0 \tag{2.6b}$$

and their variations are given by:

$$\delta\boldsymbol{\Gamma} = \boldsymbol{\Lambda}^T\left(\delta\boldsymbol{r}' + \boldsymbol{r}'\times\delta\boldsymbol{\theta}\right) \tag{2.7a}$$

$$\delta\boldsymbol{\Omega} = \boldsymbol{\Lambda}^T\delta\boldsymbol{\theta}' \tag{2.7b}$$

where $\boldsymbol{\Lambda}$ can be decomposed into axial tension and shear stresses and $\boldsymbol{\Omega}$ can be decomposed into torsion and bending stresses.

Constitutive law

The final consideration for defining the SIMO-REISSNER beam formulation is the constitutive law. To this end, a hyperelastic stored energy function is employed [20]:

$$\tilde{\Pi}_{int}(\boldsymbol{\Gamma},\boldsymbol{\Omega}) = \frac{1}{2}\boldsymbol{\Gamma}^T\boldsymbol{C}_F\boldsymbol{\Gamma} + \frac{1}{2}\boldsymbol{\Omega}^T\boldsymbol{C}_M\boldsymbol{\Omega} \tag{2.8}$$

with the following constitutive tensor definitions:

$$\boldsymbol{C}_F = \begin{bmatrix} EA & 0 & 0\\ 0 & G\bar{A}_2 & 0\\ 0 & 0 & G\bar{A}_3\end{bmatrix}_{\{\boldsymbol{E}_1,\boldsymbol{E}_2,\boldsymbol{E}_3\}} \tag{2.9a}$$

$$\boldsymbol{C}_M = \begin{bmatrix} GI_T & 0 & 0\\ 0 & EI_2 & 0\\ 0 & 0 & EI_3\end{bmatrix}_{\{\boldsymbol{E}_1,\boldsymbol{E}_2,\boldsymbol{E}_3\}} \tag{2.9b}$$

where E is the YOUNG's modulus, G is the shear modulus, A is the area of cross-section, $\bar{A}_2$ and $\bar{A}_3$ are the reduced cross-sectional areas, I_2 and I_3 are the principle moments of inertia (which are equal for circular cross-sections), and I_T is the torsional moment of inertia. Using Equation 2.8 then allows for the total forces and moments to be isolated as follows [20]:

$$\boldsymbol{F} = \frac{\partial \tilde{\Pi}_{int}}{\partial \boldsymbol{\Gamma}} = \boldsymbol{C}_F \cdot \boldsymbol{\Gamma} \tag{2.10a}$$

$$\boldsymbol{M} = \frac{\partial \tilde{\Pi}_{int}}{\partial \boldsymbol{\Omega}} = \boldsymbol{C}_M \cdot \boldsymbol{\Omega} \tag{2.10b}$$

Next, the kinetic energy of the beam as can be written as [20]:

$$\tilde{\Pi}_{kin} = \frac{1}{2}\boldsymbol{\Lambda}\boldsymbol{C}_\rho\boldsymbol{\Lambda}^T \tag{2.11}$$

where the material inertia tensor $\boldsymbol{C}_\rho$ is given by:

$$\boldsymbol{C}_\rho = \begin{bmatrix} I_p & 0 & 0 \\ 0 & \rho I_2 & 0 \\ 0 & 0 & \rho I_3 \end{bmatrix}_{\{\boldsymbol{E}_1,\boldsymbol{E}_2,\boldsymbol{E}_3\}} \tag{2.12}$$

Here, ρ is the mass density and I_p is the cross-section's polar moment of inertia. From (2.11), the length-specific linear $\tilde{\boldsymbol{l}}$ and angular $\tilde{\boldsymbol{h}}$ momenta may be obtained by differentiating with respect to linear velocity $\dot{\boldsymbol{r}}$ and angular velocity $\boldsymbol{w}$, respectively, yielding [20]:

$$\tilde{\boldsymbol{I}} := \frac{\partial \tilde{\Pi}_{kin}}{\partial \dot{\boldsymbol{r}}} = \rho A \dot{\boldsymbol{r}} \tag{2.13a}$$

$$\tilde{\boldsymbol{h}} := \frac{\partial \tilde{\Pi}_{kin}}{\partial \boldsymbol{w}} = \boldsymbol{\Lambda}\boldsymbol{C}_\rho \boldsymbol{W} \tag{2.13b}$$

Then, the total quantities for forces, moments and energies can simply be obtained by integrating along the beam [20]:

$$\boldsymbol{f}_{ext} := \int_0^l \tilde{\boldsymbol{f}}\, \mathrm{d}s + \left[\bar{\boldsymbol{f}}\right]_{\Gamma_\sigma} \tag{2.14a}$$

$$\boldsymbol{m}_{ext} := \int_0^l \left(\boldsymbol{r} \times \tilde{\boldsymbol{f}} + \tilde{\boldsymbol{m}}\right) \mathrm{d}s + \left[\boldsymbol{r} \times \bar{\boldsymbol{f}} + \bar{\boldsymbol{m}}\right]_{\Gamma_\sigma} \tag{2.14b}$$

$$\Pi_{int} := \int_0^l \tilde{\Pi}_{int}\, \mathrm{d}s \tag{2.14c}$$

$$\Pi_{kin} := \int_0^l \tilde{\Pi}_{kin}\, \mathrm{d}s \tag{2.14d}$$

$$\boldsymbol{I}a := \int_0^l \tilde{\boldsymbol{I}}\mathrm{d}s \tag{2.14e}$$

$$\boldsymbol{h} := \int_0^l \left(\tilde{\boldsymbol{h}} + \boldsymbol{r} \times \tilde{\boldsymbol{I}}\right) \mathrm{d}s \tag{2.14f}$$

From Equation 2.13, the inertia force $\boldsymbol{f}_\rho$ and moment $\boldsymbol{m}_\rho$ can be isolated as follows [20]:

$$-\boldsymbol{f}_\rho := \dot{\tilde{\boldsymbol{I}}} = \rho A \ddot{\boldsymbol{r}} \tag{2.15a}$$

$$-\boldsymbol{m}_\rho := \dot{\tilde{\boldsymbol{h}}} = \boldsymbol{\Lambda}\left[\boldsymbol{S}(\boldsymbol{W})\boldsymbol{C}_\rho\boldsymbol{W} + \boldsymbol{C}_\rho\boldsymbol{A}\right] = \boldsymbol{S}(\boldsymbol{w})\boldsymbol{c}_\rho\boldsymbol{w} + \boldsymbol{c}_\rho\boldsymbol{a} \tag{2.15b}$$

where $\boldsymbol{a} := \dot{\boldsymbol{w}}$ and $\boldsymbol{A} = \dot{\boldsymbol{W}}$. Additionally, the quantity $\boldsymbol{w}$ can be related to $\boldsymbol{\Psi}$ with the use of the inverse tangent operator $\boldsymbol{T}^{-1}$ by $\boldsymbol{w} = \boldsymbol{T}^{-1}\dot{\boldsymbol{\Psi}}$. Similarly, $\boldsymbol{a} = \dot{\boldsymbol{T}}^{-1}\dot{\boldsymbol{\Psi}} + \boldsymbol{T}^{-1}\ddot{\boldsymbol{\Psi}}$ [20].

This concludes the definitions required to express the weak form in Equation 2.3. The weak form Equation 2.3 is equivalent to the strong form Equation 2.2 when the appropriate boundary conditions are considered. Namely, the well-defined boundary value problem (BVP) can be formulated by supplementing Equation 2.2 with the following boundary conditions [20]:

$$\boldsymbol{r} = \boldsymbol{r}_u \quad \text{on } \Gamma_u \tag{2.16a}$$
$$\boldsymbol{\Psi} = \boldsymbol{\Psi}_u \quad \text{on } \Gamma_u \tag{2.16b}$$
$$\boldsymbol{f} = \bar{\boldsymbol{f}} \quad \text{on } \Gamma_\sigma \tag{2.16c}$$
$$\boldsymbol{m} = \bar{\boldsymbol{m}} \quad \text{on } \Gamma_\sigma \tag{2.16d}$$
$$\Gamma_u \cap \Gamma_\sigma = \emptyset \tag{2.16e}$$
$$\Gamma_u \cup \Gamma_\sigma = \{0, l\} \tag{2.16f}$$
$$\boldsymbol{r} = \boldsymbol{r}_0 \quad \text{at } t = 0 \tag{2.16g}$$
$$\dot{\boldsymbol{r}} = \boldsymbol{v}_0 \quad \text{at } t = 0 \tag{2.16h}$$
$$\boldsymbol{\Lambda} = \boldsymbol{\Lambda}_0 \quad \text{at } t = 0 \tag{2.16i}$$
$$\boldsymbol{w} = \boldsymbol{w}_0 \quad \text{at } t = 0 \tag{2.16j}$$

2.2.4. Kirchhoff-Love beam

All formulae in this section have been adapted from Meier *et al.*'s seminal text on their geometrically exact KIRCHHOFF-LOVE beam formulation [31].

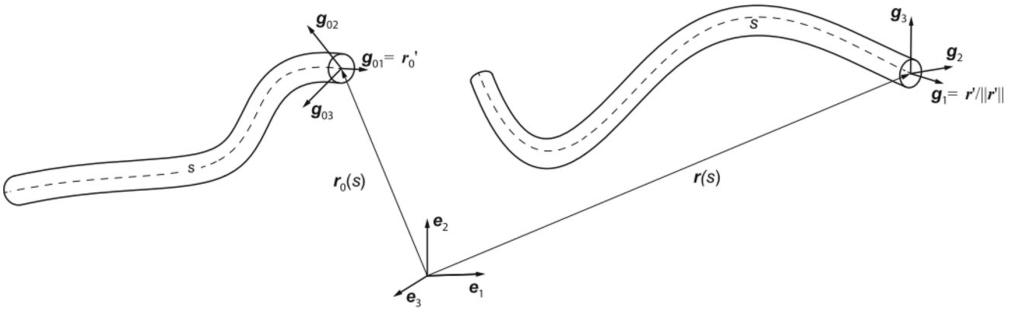

Figure 2.14: Kinematics quantities for a KIRCHHOFF-LOVE beam in its initial (left) and current configuration (right) [32]

Kinematics

The same parametrization of the SIMO-REISSNER beam introduced in Subsection 2.2.3 can be applied to the discussion of the KIRCHHOFF-LOVE beam. As illustrated in Figure 2.14, the initial (straight) configuration of the beam is described by the space curve $s \mapsto \boldsymbol{r}_0(s) \in \mathbb{R}^3$. As in the case of the SIMO-REISSNER beam, $s \in [0, l] \subset \mathbb{R}$ is an arc-length parametrization of the curve and $l \in \mathbb{R}$ is the beam length in the initial configuration. The description of the initial configuration is completed by a field of right-handed orthonormal base vectors $s \mapsto \boldsymbol{g}_{01}(s), \boldsymbol{g}_{02}(s), \boldsymbol{g}_{03}(s) \in \mathbb{R}^3$. A key feature of the selected basis is that the first base vector $\boldsymbol{g}_{01}(s)$ coincides with the initial unit tangent vector, *i.e.*,

$$\boldsymbol{g}_{01} \equiv \boldsymbol{r}_0' \quad \text{with } \|\boldsymbol{r}_0'\| = 1 \tag{2.17}$$

and $\boldsymbol{g}_{02}(s), \boldsymbol{g}_{03}(s)$ coincide with the principal axes of inertia of the cross-section (or the axes of a circle in the case of a cylindrical beam). The orthogonal transformation $s \mapsto \boldsymbol{\Lambda}_0(s) \in SO(3)$ rotates the global frame into the initial local frame $\boldsymbol{g}_{0i}$ with [31] :

$$\boldsymbol{g}_{0i} = \boldsymbol{\Lambda}_0(s)\boldsymbol{E}_i(s) \quad \text{for } i = 1, 2, 3 \quad \text{with } \boldsymbol{\Lambda}_0(s) = \boldsymbol{g}_{0j}(s) \otimes \boldsymbol{E}_j \tag{2.18}$$

Following the assumption of vanishing shear strains, which holds for long slender rods, a constraint that keeps the beam's cross-section perpendicular to the centreline may be enforced. Defining said tangent as $\boldsymbol{t}(s) := \boldsymbol{r}'(s)$ leads to [31]:

$$g_1(s) \equiv \frac{\boldsymbol{t}(s)}{||\boldsymbol{t}(s)||} \quad \text{or} \tag{2.19a}$$

$$g_2(s) \cdot \frac{\boldsymbol{t}(s)}{||\boldsymbol{t}(s)||} \equiv 0 \quad \text{and} \quad g_3(s) \cdot \frac{\boldsymbol{t}(s)}{||\boldsymbol{t}(s)||} \equiv 0 \tag{2.19b}$$

Equation 2.19 is identified as the KIRCHHOFF constraint. To obtain a parametrization comprised of four degrees of freedom, let $(\boldsymbol{r}(s), \phi(s))$ with $s \mapsto \phi(s) \in \mathbb{R}$ be the new parametrization which fulfills the KIRCHHOFF constraint in a strong manner. Meier *et al.* present a method for doing this by introducing a local field of right-handed orthonormal triads called the *reference triads*, where $s \mapsto g_{ref,1}(s), g_{ref,2}(s), g_{ref,3}(s)$ are characterized by the following conditions [31]:

$$g_{ref,1}(s) = \frac{\boldsymbol{t}(s)}{||\boldsymbol{t}(s)||} \tag{2.20a}$$

$$g_{ref,2}(s) = f_2(\boldsymbol{r}(s), \boldsymbol{r}'(s), \boldsymbol{r}''(s)) \tag{2.20b}$$

$$g_{ref,3}(s) = f_3(\boldsymbol{r}(s), \boldsymbol{r}'(s), \boldsymbol{r}''(s)) \tag{2.20c}$$

In Equation 2.20, the first reference triad is set equal to the unit tangent of the centreline, while the second and third triads are some arbitrary functions of the primary variable $\boldsymbol{r}(s)$ (and its first and second derivates). Then, Equation 2.19 and Equation 2.20 can be combined into the material frame by rotating the reference triad with respect to the tangent [31]:

$$g_1(s) = g_{ref,1} \tag{2.21a}$$

$$g_2(s) = g_{ref,2}(s)\cos\phi(s) + g_{ref,3}(s)\sin\phi(s) \tag{2.21b}$$

$$g_3(s) = g_{ref,3}(s)\cos\phi(s) - g_{ref,2}(s)\sin\phi(s) \tag{2.21c}$$

$$\tag{2.21d}$$

According to Equation 2.21, the newly introduced quantity $\phi(s)$ can be considered as an angle representing the rotation between the reference and material frames. The definitions of the reference triad and the associated analytical formulations of quantities f_1 and f_2 have been introduced in a general sense. While the motivation for this approach is well documented by Meier *et al.*, it is sufficient to consider this abstract presentation for the present application. Readers are encouraged to consult the proof if they wish to delve deeper [31]. With the abstract definition of the reference triad established, the next step is to obtain the constrained rotation vector variation, $\delta\boldsymbol{\theta}(s)$. The variation of the constrained vector is implicitly known via [31]:

$$\delta g_i(s) = \delta\boldsymbol{\theta}(s) \times g_i(s) \tag{2.22}$$

Then, further use of the KIRCHHOFF constraint (Equation 2.19) can be applied to derive [31]:

$$\delta\boldsymbol{\theta}(s) = \delta\alpha(s)\frac{\boldsymbol{t}(s)}{||\boldsymbol{t}(s)||} + \frac{\boldsymbol{r}'(s) \times \delta\boldsymbol{r}'(s)}{||\boldsymbol{r}'(s)||^2} \tag{2.23}$$

where $s \mapsto \delta\boldsymbol{r}(s) \in \mathbb{R}^3$ describes the kinematically admissible variations of $\boldsymbol{r}(s)$. The quantity $\delta\alpha(s)$ will be regarded as an independent variational degree of freedom [31]. The significance of this term will later be seen in Subsection 2.2.5.

Weak form

Note that the dependence on parameter s has been dropped for ease of notation for the remainder of this section. Beginning from the familiar equations of static equilibrium [31]:

$$\boldsymbol{f}' + \tilde{\boldsymbol{f}} = \boldsymbol{0} \tag{2.24a}$$

$$\boldsymbol{m}' + \boldsymbol{r}' \times \boldsymbol{f} + \tilde{\boldsymbol{m}} = \boldsymbol{0} \tag{2.24b}$$

where $\tilde{\boldsymbol{f}}$ and $\tilde{\boldsymbol{m}}$ are respectively the distributed external forces and moments applied to the beam. Since shear forces are neglected by construction, the force in Equation 2.24 can be split into components parallel and perpendicular to the tangent [31]:

$$\boldsymbol{f} = \boldsymbol{f}_{\parallel} + \boldsymbol{f}_{\perp} = f_{\parallel} \cdot \frac{\boldsymbol{t}}{||\boldsymbol{t}||} + \boldsymbol{f}_{\perp} \tag{2.25}$$

With some algebraic manipulation and following the elimination of shear forces in Equation 2.25, the new system of equations becomes:

$$\left(\frac{\boldsymbol{t}}{||\boldsymbol{t}||}\right)^T (\boldsymbol{m}' + \tilde{\boldsymbol{m}}) = 0 \tag{2.26a}$$

$$\boldsymbol{f}'_{\parallel} + \left[\frac{\boldsymbol{r}'}{||\boldsymbol{r}'||^2} \times (\boldsymbol{m}' + \tilde{\boldsymbol{m}})\right]' + \tilde{\boldsymbol{f}} = 0 \tag{2.26b}$$

Equation 2.26a and Equation 2.26b now represents a system of four differential equations in the variables $\boldsymbol{r}$ and ϕ. The variation process is completed by multiplying Equation 2.26a by virtual twist rotation $\delta\alpha$ and Equation 2.26b by virtual displacement $\delta\boldsymbol{r}$. Following standard integral calculus, the following weak form is recovered [31]:

$$\begin{aligned} R(\boldsymbol{r}, \phi, \delta\alpha, \delta\boldsymbol{r}) = \int_0^l &\left[\delta\boldsymbol{\theta}'^T \boldsymbol{m} + \delta\boldsymbol{r}'^T \left(\frac{\boldsymbol{t}}{||\boldsymbol{t}||}\right) f_{\parallel} - \delta\boldsymbol{r}^T \tilde{\boldsymbol{f}} - \delta\boldsymbol{\theta}^T \tilde{\boldsymbol{m}}\right] \mathrm{d}s \\ &- \left[\delta\boldsymbol{r}^T \bar{\boldsymbol{f}} + \delta\boldsymbol{\theta}^T \bar{\boldsymbol{m}}\right]_{\Gamma_\sigma} = 0 \end{aligned} \tag{2.27a}$$

$$\delta\boldsymbol{\theta} = \delta\alpha \frac{\boldsymbol{t}}{||\boldsymbol{t}||} + \frac{\boldsymbol{r}' \times \delta\boldsymbol{r}'}{||\boldsymbol{r}'||^2} \tag{2.27b}$$

With the desired constrained variation of $\boldsymbol{\theta}$ now given by Equation 2.27b, the derivation of the weak form for the general KIRCHHOFF-LOVE beam is concluded.

Constitutive law

By employing the assumption of vanishing shears in the KIRCHHOFF-LOVE model, simplifications can be made to the constitutive law that was previously presented for SIMO-REISSNER formulation. The contribution of the moment stress resultant is a slight modification to SIMO-REISSNER case, while the omission of $\boldsymbol{f}_{\perp}$ now simplifies the definition of the force resultant considerably. Accordingly, the constitutive relations for the general KIRCHHOFF-LOVE beam are as follows [31]:

$$\boldsymbol{m} = \boldsymbol{c}_m \cdot \boldsymbol{\omega} \tag{2.28a}$$

$$f_{\parallel} = EA\epsilon \tag{2.28b}$$

where $\epsilon = ||\boldsymbol{r}'|| - 1$, E is the YOUNG's modulus and A is the cross-sectional area of the beam. Moreover, $\boldsymbol{\omega}$ is given by [31]:

$$\boldsymbol{\omega} = \begin{bmatrix} \boldsymbol{g}'_{ref,2} \cdot \boldsymbol{g}_{ref,3} + \phi' - \boldsymbol{g}'_{ref,02} \cdot \boldsymbol{g}_{ref,03} - \phi'_0 \\ (\boldsymbol{g}_2 \cdot \boldsymbol{\kappa}) - (\boldsymbol{g}_{02} \cdot \boldsymbol{\kappa}_0) \\ (\boldsymbol{g}_3 \cdot \boldsymbol{\kappa}) - (\boldsymbol{g}_{03} \cdot \boldsymbol{\kappa}_0) \end{bmatrix}_{\boldsymbol{g}_i} \tag{2.29}$$

with $\boldsymbol{\kappa} = \frac{\boldsymbol{r}' \times \boldsymbol{r}''}{||\boldsymbol{r}'||}$. The constitutive tensor is given by [31]:

$$\boldsymbol{c}_m = \begin{bmatrix} GI_T & 0 & 0 \\ 0 & EI_2 & 0 \\ 0 & 0 & EI_3 \end{bmatrix}_{\boldsymbol{g}_i} \tag{2.30}$$

This concludes the discussion on the general KIRCHHOFF–LOVE beam formulation.

2.2.5. Geometrically exact torsion-free Kirchhoff-Love beam

It is assumed that the beam undergoes isotropic bending, meaning the principal moments of inertia of the cross-section are equal ($I_1 = I_2 = I$), a condition intrinsically met by cylindrical beams. Additionally, it is assumed that there are no torsional components in the distributed and discrete external moments acting on the beam. This is formally expressed as [31]:

$$\left(\frac{\boldsymbol{t}}{||\boldsymbol{t}||}\right) \cdot \tilde{m} = \tilde{m}_{||} \equiv 0 \quad \text{and} \quad \left[\left(\frac{\boldsymbol{t}}{||\boldsymbol{t}||}\right) \cdot \bar{\boldsymbol{m}}\right]_{\Gamma_\sigma} = \left[\bar{m}_{||}\right]_{\Gamma_\sigma} = 0 \tag{2.31}$$

It has also been shown by Meier *et al.* that the torsional component $m_{||}$ of the moment stress resultant m is constant in this case (see [20] for a full derivation), thus:

$$m'_{||} = 0 \tag{2.32}$$

According to Equation 2.31, $m_{||}$ is zero along the entire beam, hence the so-called *torsion-free reduced model*. Moreover, the model is further simplified by eliminating the degrees of freedom associated with torsional deformation modes, thereby rendering the weak form only dependent on the primary variable $\boldsymbol{r}$ (and its variation)[31]:

$$\begin{aligned} R(\boldsymbol{r}, \delta\boldsymbol{r}) = \int_0^l & \left[\delta\boldsymbol{r}^T \tilde{\boldsymbol{f}} - \delta\boldsymbol{r}'^T \left(EA\boldsymbol{h_1} + EI\boldsymbol{h_2} + \frac{\boldsymbol{r}'}{||\boldsymbol{r}'||^2} \times \tilde{\boldsymbol{m}}\right) - \delta\boldsymbol{r}''^T EI\boldsymbol{h_3}\right] \mathrm{d}s \\ & + \left[\delta\boldsymbol{r}^T \bar{\boldsymbol{f}} - \delta\boldsymbol{r}'^T \left(\frac{\boldsymbol{r}'}{||\boldsymbol{r}'||^2} \times \bar{\boldsymbol{m}}\right)\right]_{\Gamma_\sigma} = 0 \end{aligned} \tag{2.33}$$

where E and I are the modulus of elasticity and cross-sectional moment of inertia, respectively. Moreover, the shorthands $\boldsymbol{h_1}$, $\boldsymbol{h_2}$, and $\boldsymbol{h_3}$ are defined as:

$$\boldsymbol{h_1} := \boldsymbol{r}' \left(1 - \frac{1}{||\boldsymbol{r}'||}\right) \tag{2.34a}$$

$$\boldsymbol{h_2} := \frac{2\boldsymbol{r}' \left(\boldsymbol{r}'^T \boldsymbol{r}''\right)^2}{||\boldsymbol{r}'||^6} - \frac{\boldsymbol{r}' \left(\boldsymbol{r}''^T \boldsymbol{r}''\right) + \boldsymbol{r}'' \left(\boldsymbol{r}'^T \boldsymbol{r}''\right)}{||\boldsymbol{r}'||^4} \tag{2.34b}$$

$$\boldsymbol{h_3} := \frac{\boldsymbol{r}''}{||\boldsymbol{r}'||^2} - \frac{\boldsymbol{r}' \left(\boldsymbol{r}'^T \boldsymbol{r}''\right)}{||\boldsymbol{r}'||^4} \tag{2.34c}$$

The torsion-free assumption also allows for a simplifcation in the constitutive law previously introduced for the nominal SIMO-REISSNER and general KIRCHHOFF-LOVE formulations. Assuming hyperelastic behaviour in the material, the constitutive laws relating internal axial forces and bending moments to their respective strain quantities reduce to [31]:

$$\boldsymbol{m}_\perp = EI\boldsymbol{\kappa} \tag{2.35a}$$

$$f_{||} = EA\boldsymbol{\epsilon} \tag{2.35b}$$

where the fields of axial strain $\boldsymbol{\epsilon}$ and the curvature $\boldsymbol{\kappa}$ remain unchanged from the general KIRCHHOFF-LOVE formulation. Here, the $\boldsymbol{c}_m$ tensor has been reduced to a single constant, EI, which is a material property of the cylindrical beam [31].

Special consideration should be given to Equation 2.35a in this step. Since introducing the isotropic bending and torsion-free assumptions, the constitutive relation for the moment stress resultant no longer depends on the reference triad, the quantity $\phi(s)$, nor the variational degree of freedom $\delta\alpha$. This means that $\delta\boldsymbol{\theta}$ previously defined in Equation 2.23 can be simplified to:

$$\delta\boldsymbol{\theta}(s) = \delta\boldsymbol{\theta}_\perp(s) = \frac{\boldsymbol{r}'(s) \times \delta\boldsymbol{r}'(s)}{||\boldsymbol{r}'(s)||^2} \tag{2.36}$$

This formulation involves fewer degrees of freedom than the general model in section Subsection 2.2.4, naturally improving computationally efficient. Additionally, the torsion-free model does not require rotational degrees of freedom, simplifying standard procedures such as spatial discretization, linearization, and time integration. This model is particularly well-suited for investigating structures comprised of highly slender members. Unlike other slender beam formulations, which often require artificial bending terms to stabilize compressional modes, the proposed torsion-free formulation naturally provides stabilization with mechanically consistent bending terms [31]. This yields accurate results according to the KIRCHHOFF beam theory, provided the conditions in Equation 2.31 are met.

2.2.6. Conclusions on the beam theory literature review

A discussion on various beam theories has been presented, showcasing the key characteristics of each theory. The EULER-BERNOULLI and TIMOSHENKO beam theories were introduced as simple formulations suitable for small deflections. Next, the general SIMO-REISSNER model was introduced with the notion of geometrically exact beams and shown to be the most accurate, yet complex theory, as it fully captures the degrees of freedom associated with shear and torsion. The general KIRCHHOFF–LOVE formulation was presented as a simplification of its SIMO-REISSNER predecessor, foregoing shear under the slender beam assumption. Lastly, a reduced KIRCHHOFF-LOVE variant, using isotropic bending and torsion-free assumptions, presents the most practical of the geometrically exact beam theories.

2.3. Contact mechanics

Computational contact mechanics has its roots in the broader field of computational mechanics, which emerged in the mid-20th century with the advent of numerical methods like FEM [33]. The need to understand and predict the behaviour of contacting surfaces in engineering applications has driven the evolution of this specialized domain. Initial efforts in contact mechanics were often limited by the analytical solutions available for simple geometries and loading conditions. However, the development of computational techniques has significantly expanded the ability to handle complex, real-world problems involving contact.

The formulation of a *weak form* of the contact system is a critical step in the computational treatment of contact problems. This approach involves expressing the governing equations, which are partial differential equations (PDEs), in an integral form. The weak form pertaining to a contact problem must accommodate the inherent nonlinearities associated with contact. By carefully constructing a weak form that captures contact, numerical methods like FEM can be applied to approximate the solutions to contact problems with greater flexibility and accuracy.

Enforcing contact constraints accurately and efficiently is one of the foremost challenges in computational contact mechanics. Over the years, several techniques have been developed to address this issue. Early methods, such as the penalty method, introduce artificial stiffness to the system in order to satisfy contact constraints. However, this approach could lead to ill-conditioning of the system and is inherently undesirable due to the impossibility of determining the correct penalty parameter *a priori*. LAGRANGE multiplier methods were subsequently developed, providing a more rigorous way to impose constraints without altering the original problem's conditioning. Nevertheless, these methods require the introduction of additional unknowns to the system and increase computational effort, which is not always justifiable for certain element formulations. [33]

To present a concise overview, the most relevant contact enforcement methods for beam elements in the literature shall be reviewed. Said methods may be categorized into two main families: *penalty* and LAGRANGE *multiplier methods*. It is important to note that, for the scope of this thesis, only the cases of frictionless and elastic contact are considered. Additionally, plasticity in the beams is not considered. Instead, a hyperelastic material model is used to capture large deformations.

2.3.1. The contact boundary value problem

Before discussing the methods of contact enforcement, it is necessary to first look at the general case of elastic bodies in contact and the associated weak form given some generic boundary conditions. Note that the presentation of theory and equations in this section is adapted from Wriggers' textbook on computational contact mechanics [33]. Consider the unilateral contact case presented in Figure 2.15 below:

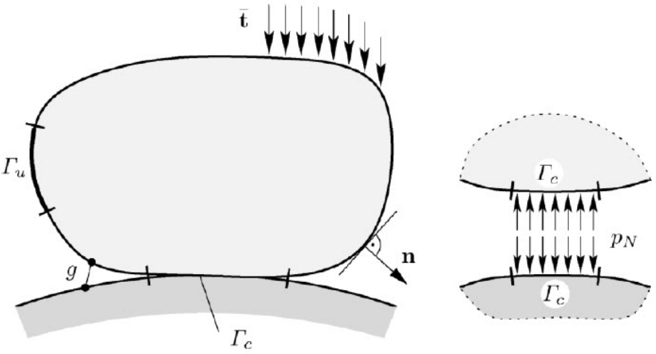

Figure 2.15: Unilateral contact of an elastic solid [33]

where $\bar{\boldsymbol{t}}$ is a distributed traction on the body $\mathcal{B}$, $\boldsymbol{n}$ is a unit vector normal to the surface of the body, Γ_u is the boundary of the body on which DIRICHLET boundary conditions apply, g is the so-called *gap function*, Γ_c is the contact boundary and, p_N is the contact pressure. Not shown in Figure 2.15 are the the following additional parameters: the displacement field $\boldsymbol{u}$, the stress tensor $\boldsymbol{\sigma}$, the boundary Γ_σ, and the distributed force vector $\bar{\boldsymbol{f}}$. According to these quantities, the linear elastic equilibrium equation may be written as as [33]:

$$\text{div}\boldsymbol{\sigma} = \bar{\boldsymbol{f}} \quad \text{in } \mathcal{B} \tag{2.37}$$

Assuming a linear strain field, the displacement gradient of the GREEN-LAGRANGE strain tensor can be employed, where [33]:

$$\boldsymbol{\epsilon} = \frac{1}{2}\left(\nabla\boldsymbol{u} + \nabla\boldsymbol{u}^T\right) \tag{2.38}$$

Then using HOOKE's linear law, the constitutive relation is defined as:

$$\boldsymbol{\sigma} = \mathbb{C}\boldsymbol{\epsilon} \tag{2.39}$$

where $\mathbb{C}$ is the linear constitutive tensor. Then the DIRICHLET, NEUMANN, and contact boundary conditions for this simplified problem may respectively be written as [33]:

$$\boldsymbol{u} = \boldsymbol{0} \quad \text{on } \Gamma_u \tag{2.40a}$$
$$\boldsymbol{\sigma}\boldsymbol{n} = \bar{\boldsymbol{t}} \quad \text{on } \Gamma_\sigma \tag{2.40b}$$
$$u_N - g \leq 0 \quad \text{on } \Gamma_c \tag{2.40c}$$
$$p_N \leq 0 \quad \text{on } \Gamma_c \tag{2.40d}$$
$$(u_N - g)p_N = 0 \quad \text{on } \Gamma_c \tag{2.40e}$$

where Equation 2.40a is the non-penetration condition, Equation 2.40b is the non-positive normal stress condition, and Equation 2.40c - Equation 2.40e are collectively called the complementarity conditions as they were initially defined in the SIGNORINI problem [34][35]. Accordingly, let $\boldsymbol{u}$ be the solution to SIGNORINI's problem and $\mathcal{V}$ be the space of vector-valued, real functions defined on $\mathcal{B}$. Then the weak form can be stated as follows: Find $\boldsymbol{u} \in \mathcal{V}$ such that for all $\boldsymbol{v} \in \mathcal{V}$ [33]:

$$\int_V \boldsymbol{\sigma} \cdot \boldsymbol{\epsilon}(\boldsymbol{u} - \boldsymbol{v})\mathrm{d}V = \int_V \bar{\boldsymbol{f}} \cdot (\boldsymbol{u} - \boldsymbol{v})\mathrm{d}V + \int_{\Gamma_\sigma} \bar{\boldsymbol{t}} \cdot (\boldsymbol{u} - \boldsymbol{v})\mathrm{d}\Gamma + \int_{\Gamma_c} p_N(\boldsymbol{u})(u_N - v_N)\mathrm{d}\Gamma \tag{2.41}$$

The variational formulation in Equation 2.41 is equivalent to the following statement: the *virtual work* produced by the stresses times the *virtual strains* is equal to the sum of the virtual work of the body forces and external loads [33].

Here, $\sigma = \sigma(u)$ is a function of the displacement defined in Equation 2.39. The final term in Equation 2.41 can be rewritten using Equation 2.40e as [33]:

$$p_N(u_N - v_N) = p_N(v_N - g) \geq 0 \tag{2.42}$$

Given the inequality appearing above, the solution to the SIGNORINI problem must satisfy:

$$\int_V \boldsymbol{\sigma} \cdot \boldsymbol{\epsilon}(\boldsymbol{u} - \boldsymbol{v})\mathrm{d}V \geq \int_V \bar{\boldsymbol{f}} \cdot (\boldsymbol{u} - \boldsymbol{v})\mathrm{d}V + \int_{\Gamma_\sigma} \bar{\boldsymbol{t}} \cdot (\boldsymbol{u} - \boldsymbol{v})\mathrm{d}\Gamma \tag{2.43}$$

As expected, the solution to problems of the SIGNORINI type are characterized by a variational inequality due to the contact constraint. This is different from typical solid mechanics problems where solutions satisfy variational equations. It is thus apparent how the inequality constraint on the deformation field makes the contact problem *nonlinear*, even in the static and linearly elastic regime.

It is important to recognize that the presence of friction adds complexity to the problem by introducing inequality constraints in the normal direction and specific constitutive behaviour in the tangential direction at the contact interface. This behaviour encompasses transitions from a state of sticking, where tangential contact stresses arise from stick conditions, to a state of sliding, where tangential stresses are determined by a constitutive equation. These factors introduce additional mathematical challenges concerning the existence and uniqueness of solutions to frictional contact problems. [33]

This exposition underscores the need for specialized algorithms to address the inherent nonlinearities in contact problems, as demonstrated even in the simplest case of SIGNORINI's problem.

2.3.2. Contact constraints for hyperelastic materials

Since the intended application in this study necessitates the modelling of impacts on lattices comprised of compliant struts, the contact problem must be defined dynamically for finite elasticity. To formulate the general case of two bodies coming into contact, consider the momentum equations [33]:

$$\mathrm{div}\boldsymbol{P}^\gamma + \bar{\boldsymbol{f}}^\gamma = \boldsymbol{0} \tag{2.44}$$

where γ is 1 for the first body and 2 for the second body. Moreover, $\boldsymbol{P}$ is the first PIOLA-KIRCHHOFF stress tensor and $\bar{\boldsymbol{f}}$ are the body forces. Accordingly, the boundary conditions for the deformation and stress fields are respectively given by their corresponding known quantities:

$$\phi^\gamma = \bar{\phi}^\gamma \quad \text{on } \Gamma^\gamma_\phi \tag{2.45a}$$

$$\boldsymbol{t}^\gamma = \bar{\boldsymbol{t}}^\gamma \quad \text{on } \Gamma^\gamma_\sigma \tag{2.45b}$$

By restricting the problem to frictionless normal contact, the contact conditions on Γ_c are stated as [33]:

$$\begin{aligned} g_N &\geq 0 \\ p_N &\leq 0 \\ g_N p_N &= 0 \end{aligned} \tag{2.46}$$

The constitutive law for hyperelastic solids can be written in general as [33]:

$$\boldsymbol{P}^\gamma = \hat{\boldsymbol{P}}\left(\boldsymbol{X}^\gamma, \boldsymbol{F}^\gamma, t\right) \tag{2.47}$$

where $\boldsymbol{X}$ is the position of a particle in the reference configuration and $\boldsymbol{F}$ is the deformation gradient. For illustrative purposes, consider a NEO-HOOKEAN material. Then the second PIOLA-KIRCHHOFF stress as can be written as [33]:

$$\boldsymbol{S} = \lambda^\gamma \left(J - 1\right)\boldsymbol{I} + 2\mu\left(\boldsymbol{b}^\gamma - \boldsymbol{I}\right) \tag{2.48}$$

where the $J = \mathrm{det}\boldsymbol{F}$ and λ and μ are known as the Lamé parameters.

Similarly to the process in Equation 2.43, the weak form inequality can be written based on the known boundary conditions given by Equation 2.45 and Equation 2.46 [33]:

$$\sum_{\gamma=1}^{2} \int_{V^{\gamma}} \tau^{\gamma} \cdot \nabla \left(\boldsymbol{\eta}^{\gamma} - \boldsymbol{\phi}^{\gamma}\right) \mathrm{d}V \geq \sum_{\gamma=1}^{2} \int_{V^{\gamma}} \bar{\boldsymbol{f}}^{\gamma} \cdot \left(\boldsymbol{\eta}^{\gamma} - \boldsymbol{\phi}^{\gamma}\right) \mathrm{d}V - \int_{\Gamma_{\sigma}^{\gamma}} \bar{\boldsymbol{t}}^{\gamma} \cdot \left(\boldsymbol{\eta}^{\gamma} - \boldsymbol{\phi}^{\gamma}\right) \mathrm{d}\Gamma \tag{2.49}$$

where $\tau = \boldsymbol{P}\boldsymbol{F}^{T}$ is the KIRCHHOFF stress tensor. Per Equation 2.49, the deformation fields $\boldsymbol{\phi}^{\gamma} \in \boldsymbol{K}$ can be now be found such that Equation 2.49 is satisfied $\forall\, \boldsymbol{\eta}^{\gamma} \in \boldsymbol{K}$, noting that [33]:

$$\boldsymbol{K} = \left\{ \left(\boldsymbol{\eta}^{1}, \boldsymbol{\eta}^{2}\right) \in \mathcal{V} \mid \left[\boldsymbol{\eta}^{2} - \hat{\boldsymbol{\eta}}^{1}\left(\bar{\xi}^{1}, \bar{\xi}^{2}\right) \bar{\boldsymbol{n}}_{1}\right] \geq 0 \right\} \tag{2.50}$$

This formalism ensures that the above formulation is valid for arbitrary constitutive equations. This is relevant since any of the previously discussed constitutive laws from Section 2.2 can be applied. A feature of using a hyperelastic material is that the problem can be formulated in terms of an optimization with inequality constraints. Specifically, the goal is to minimize the total potential energy given by the difference between the *strain energy function* $W(\boldsymbol{C})$ (where $\boldsymbol{C}$ is the right CAUCHY-GREEN strain tensor) and the sum of the body forces with the tractions. Mathematically, the total potential energy is thus written as [33]:

$$\Pi^{\gamma} = \int_{V^{\gamma}} W^{\gamma}(\boldsymbol{C}) \mathrm{d}V - \int_{V^{\gamma}} \bar{\boldsymbol{f}}^{\gamma} \cdot \phi^{\gamma} \mathrm{d}V - \int_{\Gamma_{\sigma}^{\gamma}} \bar{\boldsymbol{t}}^{\gamma} \cdot \phi^{\gamma} \mathrm{d}A \tag{2.51}$$

and its minimization is given by [33]:

$$\frac{\partial \Pi^{\gamma}}{\partial \phi^{\gamma}} = 0 \quad \text{subject to } g_{N} \geq 0 \quad \text{on } \Gamma_{c} \tag{2.52}$$

Given that the contact interface is known, the final weak form can be formulated by minimizing the total potential energy, now including an additional term, Π_c, which represents the contact constraint. This results in an equality expressed as follows [33]:

$$\sum_{\gamma=1}^{2} \left\{ \int_{V^{\gamma}} W^{\gamma}(\boldsymbol{C}) \mathrm{d}V - \int_{V^{\gamma}} \bar{\boldsymbol{f}}^{\gamma} \cdot \phi^{\gamma} \mathrm{d}V - \int_{\Gamma_{\sigma}^{\gamma}} \bar{\boldsymbol{t}}^{\gamma} \cdot \phi^{\gamma} \mathrm{d}A \right\} + \delta \Pi_{c} = 0 \tag{2.53}$$

The energy formulation presented in Equation 2.53 lays the groundwork for accurately capturing the effects of contact on the mechanical system. The next step is to address how to formulate the contact potential, which will be explored in the following section.

2.3.3. Techniques for enforcing contact constraints

Now, moving on to the question of enforcing contact constraints. Several approaches exist to apply the contact constraints in variational form. As previously mentioned, the foremost methods for applying the contact constraint in the context of FEM are the LAGRANGE multiplier and penalty methods. LAGRANGE multipliers introduce additional variables to enforce the contact constraints exactly by adding these constraints to the system of equations, prohibiting penetration between contacting surface in an exact sense. Alternatively, the penalty method enforces contact constraints approximately by adding a penalty term to the potential energy of the system, which imposes a force proportional to the amount of penetration, thus discouraging interpenetration but allowing for some controlled constraint violation. In general, LAGRANGE multiplier methods are the most successful with regards to accuracy when resolving problems involving contact, however, they suffer from a high computational cost on account of introducing additional primal variables to the system. Conversely, penalty methods can be highly efficient, but their approximate nature can lead to inaccuracy and instability [36]. Subsection 2.3.5 and Subsection 2.3.4 provide a more in-depth discussion of the traditional approaches introduced here, while Subsection 2.3.6 provides an overview of an alternative method of handling contact constraints called the DCR method.

2.3.4. Lagrange multiplier methods

The LAGRANGE multiplier is a powerful tool for solving constrained optimization problems [37]. To further elucidate this claim, consider the mathematical definition as it is presented by Marsden in his textbook on vector calculus and shown graphically by the example in Figure 2.16 below [37]:

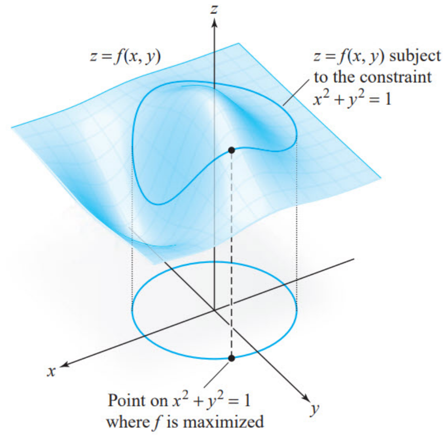

Figure 2.16: The geometric meaning of maximizing f subject to the constraint $x^2 + y^2 = 1$ [37]

Suppose that $f : U \subset \mathbb{R}^n \mapsto \mathbb{R}$ and $g : U \subset \mathbb{R}^n \mapsto \mathbb{R}$ are C^1-continuous and real-valued functions. Let $\boldsymbol{x}_0 \in U$ and $g(\boldsymbol{x}_0) = c$. Then let S be the level set for g with a value c. It can be shown, assuming $\nabla g(\boldsymbol{x}_0) \neq \boldsymbol{0}$, that if f is restricted to S has a local maximum or minimum on S at $\boldsymbol{x}_0$, then there exists a real number λ such that

$$\nabla f(\boldsymbol{x}_0) = \lambda \nabla g(\boldsymbol{x}_0) \tag{2.54}$$

where λ is the so-called LAGRANGE multiplier. From Equation 2.54, it can be deduced that the partial derivatives of f ought to be proportional to those of g, where λ acts as the constant of proportionality. In other words, the problem can be evaluated by simultaneously solving the following system of equations [37]:

$$\begin{aligned}\frac{\partial f}{\partial x_1}(x_1, x_2, x_3) &= \lambda \frac{\partial g}{\partial x_1}(x_1, x_2, x_3)\\ \frac{\partial f}{\partial x_2}(x_1, x_2, x_3) &= \lambda \frac{\partial g}{\partial x_2}(x_1, x_2, x_3)\\ \frac{\partial f}{\partial x_3}(x_1, x_2, x_3) &= \lambda \frac{\partial g}{\partial x_3}(x_1, x_2, x_3)\\ g(x_1, x_2, x_3) &= c\end{aligned} \tag{2.55}$$

λ in Equation 2.55 can alternatively be viewed as an additional variable in the system, yielding the following auxiliary equation [37]:

$$h(x_1, x_2, x_3, \lambda) = f(x_1, x_2, x_3) - \lambda\,[g(x_1, x_2, x_3) - c] \tag{2.56}$$

The constrained extrema of f can then be extracted by evaluating Equation 2.56 at the critical points of h, hence [37]:

$$\begin{aligned}0 &= \frac{\partial h}{\partial x_1} = \frac{\partial f}{\partial x_1} - \lambda \frac{\partial g}{\partial x_1} \\ 0 &= \frac{\partial h}{\partial x_2} = \frac{\partial f}{\partial x_2} - \lambda \frac{\partial g}{\partial x_2} \\ 0 &= \frac{\partial h}{\partial x_3} = \frac{\partial f}{\partial x_3} - \lambda \frac{\partial g}{\partial x_3} \\ 0 &= \frac{\partial h}{\partial \lambda} = g - c\end{aligned} \tag{2.57}$$

Concerning the example depicted in Figure 2.16, solving the constrained optimization problem is equivalent to finding extremum (the maximum in this case) of the z surface whose x and y values fall coincident with a unit circle.

This concept can now be put into the context of contact mechanics. Key concepts will first be described in the setting of rigid body impacts, however, it should be noted that all subsequent contact enforcement techniques in this section can be extended to deformable bodies. The connection between constrained optimization in the pure mathematical sense and the applied case of contact is the presence of an inequality constraint which prohibits penetration between bodies. In a contact-integrated dynamic system, an analogy can be drawn to the example provided in Figure 2.16 above. Here, the system's energy serves as f, and the contact constraint functions as g. Extending this analogy, consider a slight modification to the constraint function to better align with the mathematical role of the impenetrability constraint. Instead of seeking a maximum *on* the unit circle, an inequality constraint seeks the solution *within* the circle.

To expand upon the abstract definition of this concept to its application in enforcing contact, consider the example of a spring-mass system given by Wriggers [33]. This simple case involves a point mass m suspended at height h by a spring with the spring constant k and subject to gravity g. This is shown schematically in Figure 2.17 below.

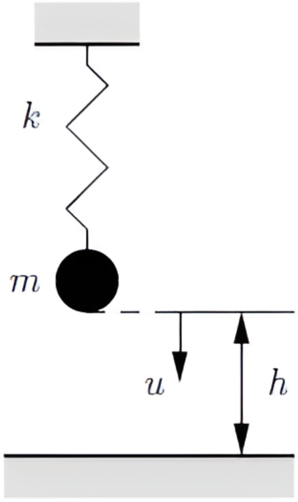

Figure 2.17: Point mass supported by a spring [33]

Then the energy of the system can simply be written as:

$$\Pi(u) = \frac{1}{2}ku^2 - mgu \tag{2.58}$$

whose variation is:

$$\delta\Pi(u) = ku\delta u - mg\delta u = 0 \tag{2.59}$$

Since the mass will eventually *collide* with a rigid support below it, the permissible domain of motion can be described in terms of u with the following inequality [33]:

$$c(u) = h - u \geq 0 \tag{2.60}$$

Hence, $c(u)$ describes the *gap* between the mass and the contact surface. It follows that the virtual displacement is restricted by $\delta u \leq 0$ at $u = h$. Combining this with Equation 2.59 leads to the following variational inequality [33]:

$$ku\delta u - mg\delta u \geq 0 \tag{2.61}$$

By formulating the problem in this way, the solution to the minimization problem no longer necessarily occurs at $u = \frac{mg}{k}$, but is rather defined by a new space of admissible solutions and is denoted by Π^c_{min}. This is illustrated graphically in Figure 2.18 below.

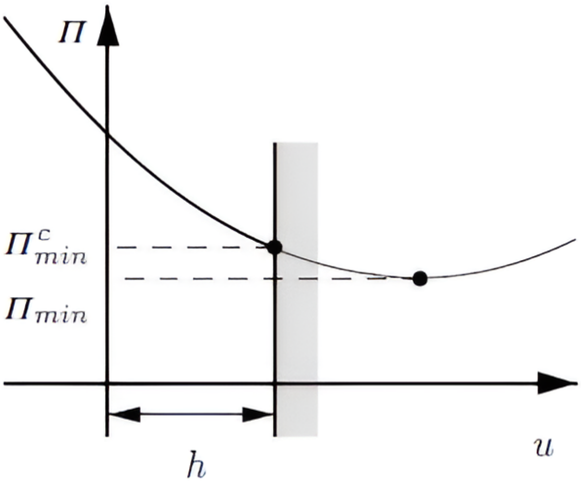

Figure 2.18: Energy of the mass spring system [33]

The variational inequality given by Equation 2.61 introduces a nonlinearity to the governing equation of the mechanical system which cannot be solved directly, even in the simplest cases. It is precisely this feature of the underlying mathematics that motivates the need for special techniques to handle contact. Two such techniques are the LAGRANGE multiplier and the penalty approaches.

The method of the LAGRANGE multiplier can be used to modify Equation 2.61 with the constraint described by Equation 2.60. This leads to the following energy equation [33]:

$$\Pi(u, \lambda) = \frac{1}{2}ku^2 - mgu + \lambda c(u) \tag{2.62}$$

The addition of the new and independent LAGRANGE multiplier means that variational principles can be applied to yield the following system of equations [33]:

$$ku\delta u - mg\delta u - \lambda\delta u = 0 \tag{2.63a}$$
$$c(u)\delta\lambda = 0 \tag{2.63b}$$

Equation 2.63a represents the equilibrium for the point mass when it comes into contact with the rigid support, and Equation 2.63b states the fulfillment of the kinematic constraint defined by Equation 2.60. In this way, λ can be directly solved. In this simple example, λ evaluates to the reaction force at the contact surface.

From this brief example, the LAGRANGE multiplier method is quite enticing as a means of capturing contact. The LAGRANGE multiplier ensures strict adherence to contact constraints, leading to accurate solutions. Nevertheless, these techniques necessitate solving implicit augmented systems of equations, which can be highly resource-intensive for large-scale problems. Furthermore, the implicit nature of these methods poses significant challenges for parallel implementation [1]. The need for higher computational efficiency in modelling complex contact problems gave rise to the so-called *penalty* method.

2.3.5. Penalty methods

The ease of implementation and high degree of efficiency have made penalty methods the leading contact algorithm in the computational modelling of beam contact. This section will provide the necessary exposition on the method, highlighting its advantages and disadvantages.

To begin, consider the spring-mass example introduced previously in Subsection 2.3.4 and adapted from Wriggers [33]. The penalty method can be thought of as an approximation to what was being exactly solved with a LAGRANGE multiplier. To highlight this, recall the energy balance in Equation 2.62. Suppose the exact enforcement of non-penetration is replaced with a weaker version of the constraint that can still be expressed in terms of the primary variable u. A simple solution would be to imagine that the support is not rigid, but rather acts as a very stiff spring, as shown in Figure 2.19.

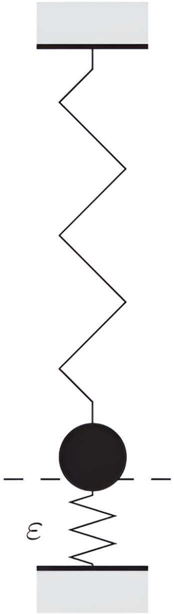

Figure 2.19: Spring mass system including a penalty spring in place of the support [33]

Thus, the penalty version of Equation 2.62 can be rewritten to include the spring energy of the penalty spring:

$$\Pi(u) = \frac{1}{2}ku^2 - mgu + \frac{1}{2}\epsilon\,[c(u)]^2\,, \quad \epsilon > 0 \tag{2.64}$$

and its variation:

$$ku\delta u - mg\delta u - \epsilon c(u)\delta u = 0 \tag{2.65}$$

which finally gives the solution:

$$u = \frac{mg + \epsilon h}{k + \epsilon} \tag{2.66}$$

From Equation 2.66, it is evident that the solution is dependent on the penalty stiffness ϵ. The penetration distance, and thus the penalty force, is proportional to the magnitude of the spring stiffness, highlighting the importance of properly selecting ϵ. Additionally, it should be noted that in the limit $\epsilon \to \infty$ recovers the exact solution found directly with the LAGRANGE multiplier method. In other words, the penalty approach is an approximation of the *exact* constraint enforcement of a LAGRANGE multiplier.

For the simple mass-spring example, selecting a large stiffness ϵ poses no issue in recovering the approximate solution. In the context of finite element implementations, however, the stiffness of the system is of great importance for numerical stability. Selecting a large penalty stiffness can lead to significant convergence issues for finite element contact problems [36]. Moreover, tuning this parameter to approximate an appropriate penalty force is unique to every problem and can only be determined *a posteriori*. While the penalty approach boasts high computational performance when compared to the LAGRANGE multiplier method, its use is to be exercised with caution.

2.3.6. Decomposition contact response (DCR) method

A third contact algorithm, that falls under neither the LAGRANGE multiplier nor penalty categorizations, is the so-called DCR method. It was originally proposed by Cirak and West in their 2005 paper of the same name [1]. In their paper, Cirak and West lay out a novel explicit contact algorithm originally tailored for solid and shell elements, with both smooth and non-smooth geometries. The DCR method employs a predictor-corrector type algorithm for time integration, where impenetrability constraints and momentum exchanges between impacting bodies are enforced independently after each predictor step. The correction of geometrically inadmissible penetrations is achieved using closest point projections, and penetration is measured using the appropriate geometric formulation of the gap between contacting elements [1].

A significant advantage of the DCR method is its ability to provide a closed-form solution for the instantaneous velocity changes that occur during an impact event. The algorithm is explicit, which simplifies its implementation and enhances computational efficiency, while also ensuring excellent momentum and energy conservation characteristics. This allows for superior stability performance compared to parameter-sensitive penalty methods and enhanced efficiency compared to LAGRANGE multiplier methods. [1]

Deriving the impact equations

The self-equilibrating impulses applied during contact events are derived using a non-smooth variational mechanics framework. While the topic variational collision integrators in discrete mechanics falls out of scope for this thesis, a formal proof for the simplecticity and momentum-conserving properties of the framework applied in the DCR method is provided by Fetecau *et al.* [38]. Moreover, further reading of Marsden and West's historically motivated synopsis of variational integrators provides a foundation for understanding discrete mechanics from the HAMILTONIAN viewpoint [39]. These aforementioned impulses, resulting from an elastic collision, maintain the system's kinetic energy and momenta, while frictional impulses cause energy dissipation without altering the system's total linear or angular momenta. Unlike traditional contact enforcement methods, the impulse magnitudes in this context are independent of penetration depth. In frictional contact, tangential forces should directly depend on normal pressures, and any non-physical assumptions about these pressures can compromise the numerical solution's accuracy [1].

The discrete impact equations can be derived from first defining the LAGRANGIAN of the system and integrating it over time, *i.e.*, the action integral. Considering a hyperelastic element undergoing a single impact event, the action integral is written as [1]:

$$S(\boldsymbol{x}, \dot{\boldsymbol{x}}, t_c) = \int_0^{t_c} L(\boldsymbol{x}, \dot{\boldsymbol{x}})\mathrm{d}t + \int_{t_c}^{T} L(\boldsymbol{x}, \dot{\boldsymbol{x}})\mathrm{d}t \tag{2.67}$$

where t_c is the unknown impact time, T is the end of the time step, and L is the semi-discrete LAGRANGIAN [1]:

$$L(\boldsymbol{x}, \dot{\boldsymbol{x}}) = \dot{\boldsymbol{x}}^T \boldsymbol{M} \dot{\boldsymbol{x}} - W(\boldsymbol{x}) + \boldsymbol{f}_{\text{ext}} \cdot \boldsymbol{x} \tag{2.68}$$

Here, $\boldsymbol{M}$ is the mass matrix of the local system, W is the internal energy, $\boldsymbol{x}$ is the deformed nodal position, and $\boldsymbol{f}_{\text{ext}}$ is the external force vector [1].

Consider now the admissible set of deformations given contact, denoted A. If Q is the set of all geometrically admissible deformations on $\boldsymbol{x}$, the constrained case may be written as $A = \{\boldsymbol{x} \in Q | g(\boldsymbol{x}) \leq 0\}$, with $A \subset Q$. The *constraint function* $g(\boldsymbol{x})$ is a purely geometric manifestation of the impenetrability condition. At the boundary ∂A, the admissible deformations are those for which contact has occurred without penetration [1]. Herein lies the strength of the DCR algorithm. Since the constraint function only serves the role of a binary checker for penetration based on the geometry of the system, its definition is arbitrary. For solid elements, Cirak and West propose using the signed volume of the tetrahedron formed by the interpenetration of contacting elements. For shell elements, the signed area of a triangle can be used [1]. In the case of 1D beam elements, the constraint function can simply be viewed as the gap function. Recalling the definition of equilibrium, the action integral can be set to zero when stationary [1]:

$$\delta S(\boldsymbol{x}, \dot{\boldsymbol{x}}, t_c) = \frac{\partial S}{\partial \boldsymbol{x}} \cdot \delta \boldsymbol{x} + \frac{\partial S}{\partial \dot{\boldsymbol{x}}} \cdot \delta \dot{\boldsymbol{x}} + \frac{\partial S}{\partial t_c} \delta t_c = 0 \tag{2.69}$$

Applying the EULER-LAGRANGE equation of standard variational calculus leads to [1]:

$$\delta S(\boldsymbol{x}, \dot{\boldsymbol{x}}, t_c) = \int_0^T \left(\frac{\partial L}{\partial \boldsymbol{x}} - \frac{\mathrm{d}}{\mathrm{d}t} \frac{\partial L}{\partial \dot{\boldsymbol{x}}} \right) \cdot \delta \boldsymbol{x} \mathrm{d}t - \left[\frac{\partial L}{\partial \dot{\boldsymbol{x}}} \cdot \delta \boldsymbol{x} + L \delta t_c \right]_{t_c^-}^{t_c^+} = 0 \tag{2.70}$$

where the superscripts (−) and (+) denote the instant immediately before and after impact, respectively. The first integral term in Equation 2.70 is sufficient for determining the general solution for the equation of motion, namely [1]:

$$\boldsymbol{M} \ddot{\boldsymbol{x}} + \frac{\partial W(\boldsymbol{x})}{\partial \boldsymbol{x}} = \boldsymbol{f}_{\text{ext}} \tag{2.71}$$

To solve the latter half of Equation 2.70 responsible for primary variables at the moment of impact, the variation of the impenetrability constraint must first be evaluated [1]:

$$\delta g \left[\boldsymbol{x}(t_c) \right] = \nabla g \cdot \left[\delta \boldsymbol{x}(t_c) + \dot{\boldsymbol{x}}(t_c) \delta t_c \right] = 0 \tag{2.72}$$

to find two independent combinations of virtual displacements $\delta \boldsymbol{x}$ and impact time variations δt_c [1]:

$$\delta \boldsymbol{x} = -\dot{\boldsymbol{x}}(t_c) \delta t_c \tag{2.73a}$$

$$\delta \boldsymbol{x} \cdot \nabla g = 0 \quad \text{for} \quad \delta t_c = 0 \tag{2.73b}$$

Both Equation 2.73a and Equation 2.73b, or any linear combination thereof, span the space of admissible impact variations. Inserting Equation 2.73a and Equation 2.73b into the last term of Equation 2.70 results in [1]:

$$\left[\frac{\partial L}{\partial \dot{\boldsymbol{x}}} \cdot \dot{\boldsymbol{x}} - L \right]_{t_c^-}^{t_c^+} = 0 \tag{2.74a}$$

$$\left[\frac{\partial L}{\partial \dot{\boldsymbol{x}}} \cdot \delta \boldsymbol{x} \right]_{t_c^-}^{t_c^+} = 0 \tag{2.74b}$$

Equation 2.74b therefore implies that the jump in $\frac{\partial L}{\partial \dot{\boldsymbol{x}}}$ across t_c must be parallel to ∇g. Mathematically, this is stated as [1]:

$$\left[\frac{\partial L}{\partial \dot{\boldsymbol{x}}} \right]_{t_c^-}^{t_c^+} = \lambda \nabla g \quad \lambda \in \mathbb{R} \tag{2.75}$$

Recalling the LAGRANGIAN of the system defined in Equation 2.68, Equation 2.74a and Equation 2.75 may be respectively rewritten as:

$$\left[\boldsymbol{p}^T \boldsymbol{M}^{-1} \boldsymbol{p}\right]_{t_c^-}^{t_c^+} = 0 \tag{2.76a}$$

$$[\boldsymbol{p}]_{t_c^-}^{t_c^+} = \lambda \nabla g \tag{2.76b}$$

where $\boldsymbol{p} = \boldsymbol{M}\dot{\boldsymbol{x}}$ is the momentum vector of the system. Therefore, if the momenta prior to impact are known, Equation 2.76a and Equation 2.76a may be used to solve for the post-impact momenta. Per this framework, the resulting post-impact momentum conserves both kinetic energy and the total linear and angular momenta [1]. With knowledge of the nodal masses, it is possible to directly extract the post-impact velocities from the momentum.

In addition to extracting post-impact velocities, the DCR method also requires a removal of detected contact intersections. This step depends on the selected geometric constraint function, but always serves the purpose of removing the interpenetration via a closest point projection. The process of projecting back the edges and nodes clearly results in an increase in internal energy. This increase can be accounted for by incorporating the work done into the energy balance. In the context of finite element, the work that ought to be subtracted from the internal energy of the system is approximately equal to the dot product of the nodal force with the artificial displacement corresponding to the intersection removal [1]:

$$W_{\text{proj}} = (\boldsymbol{f}_{\text{int}} - \boldsymbol{f}_{\text{ext}})\left(\boldsymbol{x}^- - \boldsymbol{x}^+\right) \tag{2.77}$$

While this correction factor is technically necessary for energy conservation, it need not be enforced, provided that certain criteria are met. Given sufficiently small time steps and considering the small radii of the beams, the additional work introduced by this correction is negligible compared to other forms of energy in the system, such as kinetic and internal strain energy. Additionally, if no external forces are involved in downstream applications, incorporating the energy correction from Equation 2.77 into the weak form is deemed unnecessary.

Frictionless and perfectly elastic contact

With the general framework of the DCR method now established and the impact equations derived, the next step is to apply these concepts to a more concrete application — the case of frictionless and elastic contact. In this example, specific element types and the exact form of the constraint function are not relevant. Instead, consider the fundamental quantities of mass and momentum in a generic manner to illustrate the process. To begin, the momentum of the system is decomposed into its normal and tangential components, where the normal direction is defined by the gradient of the constraint function:

$$\boldsymbol{p} = \boldsymbol{p}_{\text{norm}} + \boldsymbol{p}_{\text{tang}} \tag{2.78}$$

Since the normal component of the momentum is defined as the orthogonal projection of the resultant momentum vector onto the span of ∇g, Cirak and West show that [1]:

$$\boldsymbol{p}_{\text{norm}} = (\nabla g)^T \boldsymbol{M}^{-1} \boldsymbol{p} \left[(\nabla g)^T \boldsymbol{M} (\nabla g)\right]^{-1} \nabla g \tag{2.79}$$

Let the decomposed pre-impact momentum be defined as follows:

$$\boldsymbol{p}^- = \boldsymbol{p}_{\text{norm}}^- + \boldsymbol{p}_{\text{tang}}^- \tag{2.80}$$

and similarly, the post-impact momentum as:

$$\boldsymbol{p}^+ = \boldsymbol{p}_{\text{norm}}^+ + \boldsymbol{p}_{\text{tang}}^+ \tag{2.81}$$

To obtain post impact momenta, the process begins with the tangential component $\boldsymbol{p}_{\text{tan}}^+$. Recalling Equation 2.76b, it is evident that across contact, the momentum jump is restricted to the direction of ∇g, thereby implying that the tangential component *must* remain the same. Next, allow the jump in normal momentum to be modified by some scalar. For elastic frictionless contact, this scalar is $-e$, where e is the coefficient of restitution ($e = 1$ being fully elastic and $e = 0$ being fully inelastic). Finally, the momentum components across the jump are defined as [1]:

$$\boldsymbol{p}^{+}_{\text{tang}} = \boldsymbol{p}^{-}_{\text{tang}} \tag{2.82a}$$

$$\boldsymbol{p}^{+}_{\text{norm}} = -e\boldsymbol{p}^{-}_{\text{norm}} \tag{2.82b}$$

The final step is to recover the sum of the momentum's components post-impact, namely:

$$\boldsymbol{p}^{+} = \boldsymbol{p}^{+}_{\text{tang}} - \boldsymbol{p}^{+}_{\text{norm}} \tag{2.83}$$

Equation 2.83 then allows for the extraction of the velocity vector $\dot{\boldsymbol{x}}$. This, in combination with the updated position following the interpenetration removal, comprises a complete picture of the kinematic quantities of the momentum-conserving system post-impact. These quantities may now be fed into the explicit solver prior to the corrector step. An overview of the time-stepping scheme shall be discussed next.

Integration with an explicit solver

The DCR method was designed for implementation with an explicit solver [1]. Perhaps the most common among such solvers in the realm of structural dynamics is the NEWMARK (sometimes called the NEWMARK-beta) algorithm. To begin the discussion on time discretization, consider the following semi-discrete equations of motion:

$$\boldsymbol{M}\ddot{\boldsymbol{x}} + \boldsymbol{F}_{\text{int}} = \boldsymbol{F}_{\text{ext}} \tag{2.84}$$

where $\boldsymbol{M}\ddot{\boldsymbol{x}}$ is the inertial term, $\boldsymbol{F}_{\text{int}}$ are the internal bulk forces of the system, and $\boldsymbol{F}_{\text{ext}}$ are the external forces on the system. The *special lumping technique* so-called by Hughes and initially introduced by Hinton is used to reduce the computational cost by foregoing the need to solve a linear system for acceleration [40] [41]. As opposed to the nodal quadrature or row-sum lumping techniques, the special lumping technique *always* produces positive masses. This is achieved by enforcing that the entries of the lumped-mass matrix $\boldsymbol{M}$ be proportional to the diagonal entries of the consistent mass matrix. A constant of proportionality is determined such that it conserves the total element mass [40].

The key time-stepping feature of the second order NEWMARK method is the use of numerical parameters β and γ to control the numerical integration process. The method updates the displacement and velocity at each time step n using the following recursive formulae [42]:

$$\dot{\boldsymbol{x}}_{n+1} = \dot{\boldsymbol{x}}_{n} + (1-\gamma)\,\Delta t\ddot{\boldsymbol{x}}_{n} + \gamma\Delta t\ddot{\boldsymbol{x}}_{n+1} \tag{2.85a}$$

$$\boldsymbol{x}_{n+1} = \boldsymbol{x}_{n} + \Delta t\dot{\boldsymbol{x}}_{n} + \left(\frac{1}{2}-\beta\right)\Delta t^{2}\ddot{\boldsymbol{x}}_{n} + \beta\Delta t^{2}\ddot{\boldsymbol{x}}_{n+1} \tag{2.85b}$$

β and γ are parameters that dictate the accuracy and stability of the method [42]. The current implementation of the method sets $\beta = 0$ and $\gamma = \frac{1}{2}$, thus recovering the explicit central difference scheme. Figure 2.20 below illustrates the integration of the DCR method with the explicit NEWMARK solver.

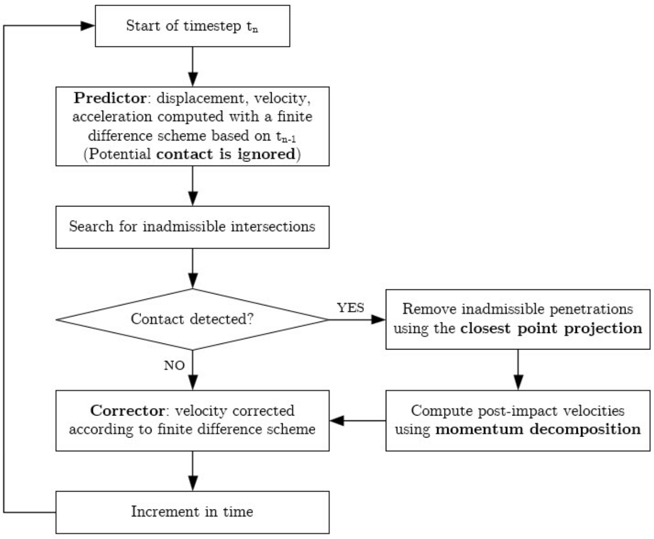

Figure 2.20: DCR-integrated time-stepping algorithm (adapted from [1])

The DCR method's compatibility with explicit solvers like the NEWMARK algorithm makes it an efficient and robust choice for capturing contact dynamics without the need for penalty parameters or additional degrees of freedom.

2.3.7. Other methods

Another method for modelling contact within the finite element framework, which neither falls under the LAGRANGE multiplier nor the penalty approach categorizations, is the so-called NITSCHE method. Several improvements have been made since the original formulation proposed by NITSCHE [43], such as the inclusion of friction [44] [45] and numerical stability improvements to its FEM implementation [46]. However, the underlying principle of the method has remained the same.

The selling point of the NITSCHE method is that it eliminates the need for LAGRANGE multipliers and is formulated only in terms of the primary displacement variables [33]. The NITSCHE approach makes use of an interface stress field that is approximated by averaging the stress fields of the bodies in contact. The contact contribution to the weak form, originally presented in Equation 2.53, can be expressed as [33]:

$$\Pi_c^N = -\int_{\Gamma_c} \frac{1}{2}\left(p_N^1 + p_N^2\right) g_N \mathrm{d}A + \frac{1}{2}\int_{\Gamma_c} \epsilon g_N^2 \mathrm{d}A \tag{2.86}$$

where the standard notation for contact pressure, the value of the gap, the interface domain, and the penalty parameter are given by p_N, g_N, Γ_c, and ϵ respectively. Important to note here is that while a penalty term is present in Equation 2.86, the solution does not depend on the value of ϵ. The penalty term is merely added as a means of preconditioning the global system of equations, and since the constraint presented in Equation 2.86 is enforced in an exact sense, the penalty term is rendered inactive [33].

In the context of linear elasticity, the contact pressures on bodies 1 and 2 can readily be expressed in terms of the displacement field using their respective traction and normal vectors (via the CAUCHY stress tensor). This means that the variation of Equation 2.86 can be computed with ease and recovers an expression that depends solely on primary displacement variables. A key limitation of the NITSCHE method is that the simple variation of the stress tensors only works nicely in the linearly elastic case. For nonlinear materials, the variation of the traction vectors becomes more difficult to compute than LAGRANGE multipliers [33]. The NITSCHE method is thus deemed not suitable for the purposes of this thesis.

Penalty, LAGRANGE multiplier, DCR, and NITSCHE methods are by no means the only contact enforcement techniques that exist in the realm of FEM. They merely represent the most relevant state-of-the art techniques that were researched in this thesis.

2.3.8. Modelling beam-to-beam contact using Lagrange multiplier method and the penalty method

Thus far, computational contact mechanics has been explored within a broad framework. To refine the focus, contact mechanics is considered specifically within the context of one-dimensional finite elements, particularly beams. Contact between beams includes some particularities due to their curve parametrizations [33]. Nevertheless, they remain the most suitable candidate for modelling truss-based architected materials. This section will serve the purpose of defining the contact problem in the context of beam elements suitable for large deformations. This section examines a formulation of the problem described in detail by Meier *et al.* and originally derived for frictionless contact by Wriggers and Zavarise [12] [47].

Consider a pair of elements described by the element parameters $\xi \in [-1,1]$ and $\eta \in [-1,1]$, respectively. Their kinematic quantities are described in Figure 2.21 below:

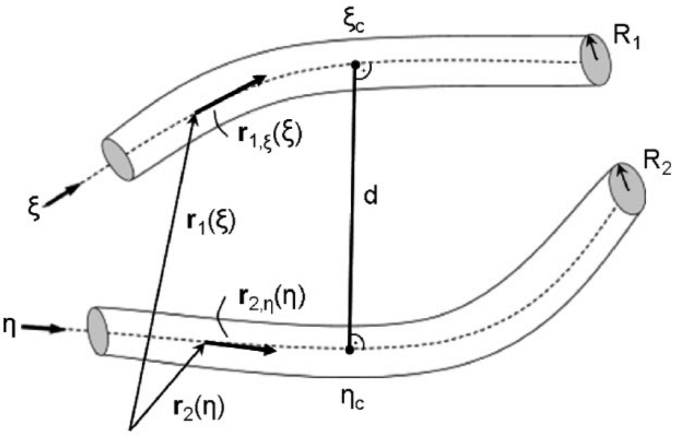

Figure 2.21: Kinematic quantities for contacting beams [12]

where the positions are given in parametric form by $\boldsymbol{r}_1(\xi)$ and $\boldsymbol{r}_2(\eta)$. Moreover, $\boldsymbol{r}_{1,\xi}(\xi)$ and $\boldsymbol{r}_{2,\eta}(\eta)$ denote the tangents of these curves at points ξ and η, respectively. R_1 and R_2 are the radii of the two beams. Under this formulation, contact is said to occur when the EUCLIDEAN distance between points on the two elements is orthogonal to *both* centrelines. This is known as the *bilateral minimum distance* problem, denoted as [12]:

$$d_{bl} := \min_{\xi,\eta} ||\boldsymbol{r}_1(\xi) - \boldsymbol{r}_2(\eta)|| \tag{2.87}$$

Equation 2.87 leads to a pair of orthogonality conditions which constrain the possible solution, namely [12]:

$$\begin{aligned} p_1(\xi_c, \eta_c) &\doteq 0 \\ p_2(\xi_c, \eta_c) &\doteq 0 \end{aligned} \tag{2.88}$$

The subscript c denotes contact and p_1 and p_2 are given by $\boldsymbol{r}^T_{1,\xi}(\xi)\,[\boldsymbol{r}_1(\xi) - \boldsymbol{r}_2(\eta)]$ and $\boldsymbol{r}^T_{2,\eta}(\eta)\,[\boldsymbol{r}_1(\xi) - \boldsymbol{r}_2(\eta)]$, respectively. Accordingly, the impenetrability condition can be formulated in terms of the solution to Equation 2.87 and the sum of the radii:

$$g \geq 0 \quad \text{with } g := d_{bl} - (R_1 + R_2) \tag{2.89}$$

A key feature of the orthogonality condition introduced in Equation 2.88 is that the resulting system can be inherently nonlinear, depending on the choice of the beams' shape functions. In order to recover a unique solution for ξ_c and η_c, the appropriate technique must be employed. Expanding Equation 2.88 and linearizing yields the following system of equations [47]:

$$\begin{aligned}&\begin{bmatrix}-\boldsymbol{r}_{1,\xi}(\xi)\cdot\boldsymbol{r}_{1,\xi}(\xi)+[\boldsymbol{r}_2(\eta)-\boldsymbol{r}_1(\xi)]\cdot\boldsymbol{r}_{1,\xi\xi}(\xi) & \boldsymbol{r}_{1,\xi}(\xi)\cdot\boldsymbol{r}_{2,\eta}(\eta)\\ -\boldsymbol{r}_{1,\xi}(\xi)\cdot\boldsymbol{r}_{2,\eta}(\eta) & \boldsymbol{r}_{2,\eta}(\eta)\cdot\boldsymbol{r}_{2,\eta}(\eta)+[\boldsymbol{r}_2(\eta)-\boldsymbol{r}_1(\xi)]\cdot\boldsymbol{r}_{2,\eta\eta}(\eta)\end{bmatrix}\begin{bmatrix}\xi_c\\ \eta_c\end{bmatrix}\\ &=-\begin{bmatrix}[\boldsymbol{r}_2(\eta)-\boldsymbol{r}_1(\xi)]\cdot\boldsymbol{r}_{1,\xi}(\xi)\\ [\boldsymbol{r}_2(\eta)-\boldsymbol{r}_1(\xi)]\cdot\boldsymbol{r}_{2,\eta}(\eta)\end{bmatrix}\end{aligned} \tag{2.90}$$

Wriggers and Zavarise, who initially formulated the system in Equation 2.90, also detailed the solution procedure for solving it [47]. It is possible to solve for ξ_c and η_c using an iterative NEWTON-RAPHSON scheme in the form of $x_{n+1} = x_n + \Delta x_{n+1}$ where x represents both element parameters ξ_c and η_c [47].

The technique described above works for a wide range of beam configurations in contact, demonstrating excellent convergence performance. However, it is not without its limitations. Meier *et al.* aptly point out a key limitation in this point-to-point formulation. They prove that a unique solution may not exist for all arbitrary configurations of the two beams, highlighting that this is the case when contacting beams have small contact angles. Specifically, Equation 2.90 can only be guaranteed to have a unique solution if the resulting contact angle α obeys the following condition [12]:

$$\alpha \dot{>} \sqrt{[1+2\bar{\kappa}_1 R_1\cos(\beta_1)]\,[1-2\bar{\kappa}_2 R_2\cos(\beta_2)]} \tag{2.91}$$

where $\bar{\kappa}_1$ and $\bar{\kappa}_2$ represent the magnitude of the curvature of the two beams. Parameters β_1 and β_2 represent the angle between the contact normals and their respective FRENET-SERRET vector normals. To circumvent this shortcoming of the point-to-point formulation, Meier *et al.* propose a line-to-line formulation that is based on a weaker geometric constraint than Equation 2.88. Rather than enforcing a contact force at a single point when the bilateral minimum distance problem is solved, their novel approach uses a distributed line load when the *unilateral minimum distance* problem is solved. This constraint only requires that the distance vector be orthogonal to one of the beam centrelines. The line-to-line approach is a more versatile approach than the point-to-point approach, however, it introduces additional complexity to the problem. This complexity comes in the form of added computational cost because the bounds of the quadrature segments needed for GAUSS integration must be dynamically defined [12]. To address this added complexity, Meier *et al.* proposed a hybrid approach in a follow-up publication. Their solution is to use the original point-to-point formulation when large contact angles are detected, then switch to the line-to-line approach when small contact angles are detected, thereby reducing computational cost and ensuring that any arbitrary configuration of the beams can always be solved. This technique has been dubbed the all-angles beam contact (ABC) method [48].

Meier *et al.*'s line-to-line approach features the use of *mortaring* techniques. In the context of beam contact, the mortar method decouples element discretization from contact integration [12]. This means that the contact residual contribution to the weak form does not need to be integrated along the same boundary as the GAUSSIAN integration used for other contributions. This technique is particularly useful for enforcing the unilateral orthogonality condition inherent in line-to-line methods, which has been proven to be variationally consistent in multiple studies [12] [49] [50]. It should be noted that mortaring techniques still rely on the use of either a penalty method or a LAGRANGE multiplier to capture the contact contribution as a distributed penalty load. However, the flexibility of integration segments allows for the capture of small contact angles that are otherwise missed in the point-to-point alternative.

Having revised the manner in which the contact distance is determined, the discussion can now move on to the contact contribution to the weak form in the context of the point-to-point approaches. The angle bracket notation $\langle . \rangle$ is introduced to denote the binary operator defined as:

$$\langle x\rangle = \begin{cases} x, & \text{if } x \leq 0\\ 0, & \text{if } x > 0\end{cases} \tag{2.92}$$

Now equipped with the gap function included in the variational equation as a part of the penalty potential, the contact contribution can be formulated using a LAGRANGE multiplier as [12]:

$$\begin{aligned} \Pi_{c\lambda} &= \lambda g \\ \lambda &\geq 0 \\ g &\geq 0 \\ \lambda g &= 0 \end{aligned} \tag{2.93}$$

If employing a direct penalty approach, the contribution of contact in the form of a potential is given by [12]:

$$\Pi_{c\epsilon} = \frac{1}{2}\epsilon\langle g\rangle^2 \tag{2.94}$$

where ϵ is the penalty parameter. State-of-the-art point-to-point contact algorithms pass the contribution of contact into the weak form via a *penalty force* [12] [48]. This penalty contact force is defined as [12]:

$$f_{c\epsilon} = -\epsilon\langle g\rangle \frac{r_1(\xi_c) - r_2(\eta_c)}{||r_1(\xi_c) - r_2(\eta_c)||} \tag{2.95}$$

2.3.9. Conclusions on the contact mechanics literature review

A review of standard computational contact enforcement techniques was presented, identifying the strengths and weaknesses of the LAGRANGE multiplier and penalty methods. The general DCR method for shell-shell or solid-solid contact was discussed and shown to neither depend on additional degrees of freedom in the form of LAGRANGE multipliers nor require a penalty parameter. Lastly, the NITSCHE method was presented as an alternative possessing similar strengths to the general DCR method but considerably limited in hyperelastic material implementations.

Both the LAGRANGE multiplier and penalty approaches were further explored by discussing their beam-to-beam implementations. In Chapter 3, a novel approach will be proposed for modelling beam-to-beam contact using the DCR method.

3

Methodology

Implicit in the primary objective of capturing the contact stiffening effect in compressed architected materials within the context of a FEM framework is the auxiliary objective of examining the feasibility and performance of the DCR method for enforcing beam-to-beam contact. To this end, the present chapter serves as a comprehensive review of the methodology applied to model experiments involving compressed architected materials.

In Section 2.2, a review of various beam element formulations was presented. Subsequently, Section 3.1 of this chapter shall motivate the selection of the torsion-free KIRCHHOFF–LOVE beam for modelling truss-based architected materials. Subsection 2.3.6 provided a review of contact mechanics and a summary of the generic DCR method. In Section 3.2 of this chapter, the theory will be applied to develop a novel formulation for beam-to-beam contact via the DCR method, encompassing the relevant topics of continuum formulation, spatial discretization, contact detection, the applied integration scheme, beam buckling considerations, and lattice joint idealizations. Subsequently, Section 3.3 provides a high-level overview of the computational framework developed for this study. Lastly, the supplementary Section 3.4 reviews an alternative method for removing contact in conjunction with the DCR method. Although not implemented, this method has been investigated and prototyped, laying a foundation for future development.

3.1. Selecting a beam element for truss-based architected materials

Having reviewed the most pertinent state-of-the-art beam models for slender structures in Section 2.2, it is now possible to synthesize their key characteristics. Considered in the comparison are each respective beam formulation's ability to capture (1) geometric nonlinearities, (2) curvature in the undeformed state, (3) anisotropic bending (*i.e.*, $I_1 \neq I_2 \neq I$), and the deformation modes of (4) tension, (5) shear, (6) bending, and (7) torsion. Table 3.1 below presents an assessment of each beam formulation regarding the aforementioned properties.

Table 3.1: Overview of beam elements (adapted from [20])

Formulations	Geometric nonlinearity	Initial curvature	Anisotropic bending	Tension	Shear	Bending	Torsion
EULER-BERNOULLI	×	×	✓	✓	×	✓	✓
TIMOSHENKO	×	×	✓	✓	✓	✓	✓
SIMO-REISSNER	✓	✓	✓	✓	✓	✓	✓
KIRCHHOFF-LOVE	✓	✓	✓	✓	×	✓	✓
Torsion-free KIRCHHOFF-LOVE	✓	×	×	✓	×	✓	×
Torsion-free SIMO-REISSNER	✓	×	×	✓	✓	✓	×

To justify the formulation choice, the requirements of the problem definition must be addressed. Given that an insideBCC lattice will be deformed well beyond its initial state when modelling compression, it is essential to incorporate geometrically nonlinear capabilities to capture large deformations and buckling. Since the lattice consists of initially straight struts, there is no need to consider initial curvature. For simplicity, the struts can be modelled with circular cross-sections, thereby eliminating the need to handle anisotropic bending.

Compression of the structure will induce significant tensile loads in the members, necessitating the inclusion of tension in the model. Given the high slenderness of the beams, a shear-free formulation is selected to simplify the problem. Bending is, of course, a crucial aspect to consider, as it is the most dominant deformation mode in this context. Finally, torsion is neglected. This assumption significantly simplifies the problem by reducing the number of degrees of freedom, thus increasing computational efficiency. Although this assumption is commonly employed for modelling cables and other highly slender beams ([12], [51], [52]), it remains a potential source of error in this study.

By assessing the requirements for modelling architected materials under compression, combined with the information provided in Table 3.1 above, the appropriate beam element type can be selected. Therefore, the remainder of this work is conducted using the torsion-free KIRCHHOFF–LOVE beam.

3.2. Development of a novel beam-to-beam contact model

To develop a novel beam-to-beam contact formulation, various FEM principles must be carefully considered. This section details the critical features taken into account throughout the development of the DCR beam-to-beam contact model.

3.2.1. Continuum formulation

With the selection of the torsion-free KIRCHHOFF–LOVE beam formulation, the weak form provided by Meier *et al.* for their point-to-point formulation may be repurposed, excluding the penalty potential contribution [12]. This selection of beam element type can be wholly described by a three-dimensional curve given by $\boldsymbol{r}(s,t) \in \mathbb{R}^3$ with $s \in [0,l] \subset \mathbb{R}$ and $l \in \mathbb{R}$ describing the arc parametrization in the initial configuration. t is simply the independent time variable. Next, a shorthand is introduced for the differential operator with respect to s as $(.)' = \frac{\partial}{\partial s}(.) = (.)_{,s}$ and with respect to t as $\dot{(.)} = \frac{\partial}{\partial t}(.) = (.)_{,t}$. For slender torsion-free KIRCHHOFF–LOVE beams, it is a reasonable assumption to neglect rotational inertia contributions [31]. Therefore, the kinetic and hyperelastic stored energies are stated as [12]:

$$\begin{aligned} \Pi_{kin} &= \int_0^l \frac{1}{2}\rho A v^2 \mathrm{d}s \\ \Pi_{int} &= \int_0^l \left[\frac{1}{2}EA\epsilon^2 + \frac{1}{2}EI\kappa^2\right] \mathrm{d}s \end{aligned} \tag{3.1}$$

where ρ is the mass density, A is the cross-sectional area, I is the moment of inertia and E is the YOUNG's modulus, v is the material velocity field, ϵ is the field of axial tension, and finally, κ is the field of bending curvature. Recall that the constitutive laws employed here were previously derived in Equation 2.35 for the isotropic bending and torsion-free KIRCHHOFF–LOVE reduced formulation. The fields in Equation 3.1 can also be expressed in terms of the current configuration, with:

$$v = ||\dot{\boldsymbol{r}}|| \tag{3.2a}$$

$$\epsilon = ||\boldsymbol{r}'|| - 1 \tag{3.2b}$$

$$\boldsymbol{\kappa} = \frac{||\boldsymbol{r}' \times \boldsymbol{r}''||}{||\boldsymbol{r}'||^2} \tag{3.2c}$$

$$\kappa = ||\boldsymbol{\kappa}|| \tag{3.2d}$$

Using the terms defined in Equation 3.1, it is possible to construct the weak form of the dynamic balance equations. The weak form derived by Meier *et al.* can be assembled as [12]:

$$\int_0^l \left[\delta\epsilon EA\epsilon + \delta\boldsymbol{\kappa} EI\boldsymbol{\kappa} + \delta\boldsymbol{r}^T \rho A \ddot{\boldsymbol{r}}\right] \mathrm{d}s - \int_0^l \left[\delta\boldsymbol{r}^T \tilde{\boldsymbol{f}} + \delta\boldsymbol{\theta}_\perp^T \tilde{\boldsymbol{m}}_\perp\right] \mathrm{d}s - \int_0^l \left[\delta\boldsymbol{r}^T \bar{\boldsymbol{f}} + \delta\boldsymbol{\theta}_\perp^T \bar{\boldsymbol{m}}_\perp\right] \mathrm{d}s \tag{3.3}$$

Where $\tilde{(.)}$ denotes distributed quantities and $\bar{(.)}$ denotes discrete quantities on the NEUMANN boundary Γ_σ. Moreover, it is noted that only the components of moments perpendicular to the beam's centreline are considered. This is a consequence of the torsion-free formulation of the beam element [12]. Lastly, $\boldsymbol{\theta}_\perp$ is the degree of freedom associated with rotation and the variations included in Equation 3.3 expand as:

$$\delta\epsilon = \frac{\delta\boldsymbol{r}'^T \boldsymbol{r}'}{||\boldsymbol{r}'||} \tag{3.4a}$$

$$\delta\boldsymbol{\kappa} = \frac{||\boldsymbol{r}'||^2 \left(\delta\boldsymbol{r}' \times \boldsymbol{r}'' + \boldsymbol{r}' \times \delta\boldsymbol{r}''\right) - 2\left(\delta\boldsymbol{r}'^T \boldsymbol{r}'\right)\left(\boldsymbol{r}' \times \boldsymbol{r}''\right)}{||\boldsymbol{r}'||^4} \tag{3.4b}$$

$$\delta\boldsymbol{\theta}_\perp = \frac{\boldsymbol{r}' \times \delta\boldsymbol{r}'}{||\boldsymbol{r}'||^2} \tag{3.4c}$$

This concludes the presentation of the weak form which will be employed for the remainder of the report.

3.2.2. Spatial discretization

Recalling that $\boldsymbol{r} \in \mathcal{S} \subset \mathbb{R}^3$ and $\delta r \in \mathcal{V} \subset \mathbb{R}^3$, it is now possible to replace the continuous formulation with a spatially discretized one. In adherence to the BUBNOV-GALERKIN method, the approximate solution to Equation 3.3 can be achieved when allowing $\boldsymbol{r} \approx \boldsymbol{r}_h \in \mathcal{S}_h \subset \mathcal{S}$ and $\delta\boldsymbol{r} \approx \delta\boldsymbol{r}_h \in \mathcal{V} \subset \mathcal{V}$. Accordingly, the discretized beam centreline formulation follows as [12]:

$$\mathbf{r}_h(\xi) = \sum_{i=1}^{2} N_x^i(\xi)\hat{\boldsymbol{x}}^i + \frac{l}{2}\sum_{i=1}^{2} N_t^i(\xi)\hat{\boldsymbol{t}}^i =: \mathbf{N}(\xi)\mathbf{x} \tag{3.5a}$$

$$\delta\mathbf{r}_h(\xi) = \sum_{i=1}^{2} N_x^i(\xi)\delta\hat{\boldsymbol{x}}^i + \frac{l}{2}\sum_{i=1}^{2} N_t^i(\xi)\delta\hat{\boldsymbol{t}}^i =: \mathbf{N}(\xi)\delta\mathbf{x} \tag{3.5b}$$

Here, $\hat{\boldsymbol{x}}^i$ represents the position of the nodes at each end of the beam. Similarly, $\hat{\boldsymbol{t}}^i$ represents the tangents at either node of the beam. The quantity l is the length of the element in its original undeformed configuration. Lastly, $\xi \in [-1, 1]$ is the element parameter. The centreline can be entirely described in the manner of Equation 3.5a via the element JACOBIAN which, thanks to the arc length parametrization $s(\xi)$ evalues to $\frac{l}{2}$. To complete the spatial discretization, third-order polynomial shape functions (also called HERMITE shape functions) are selected to match the formulation of Meier *et al.* [53] [12]:

$$\begin{gathered} N_x^1(\xi) = \frac{1}{4}(2+\xi)(1-\xi)^2, \;\; N_x^2(\xi) = \frac{1}{4}(2-\xi)(1+\xi)^2 \\ N_t^1(\xi) = \frac{1}{4}(1+\xi)(1-\xi)^2, \;\; N_t^2(\xi) = -\frac{1}{4}(1-\xi)(1+\xi)^2 \end{gathered} \tag{3.6}$$

Equation 3.6 are C^1-continuous and are instrumental in formulating an appropriate constraint function for the DCR method, which shall be covered in Subsection 3.2.4. Finally, the fully discretized version of Equation 3.3 may be written in terms of the residual contributions of the inertia, internal energies, and external forces:

$$\boldsymbol{R}_{tot} = \boldsymbol{M}\ddot{\boldsymbol{X}} + \boldsymbol{R}_{int}(\boldsymbol{X}) - \boldsymbol{R}_{ext}(\boldsymbol{X}) = \mathbf{0} \tag{3.7}$$

where the quantity $\boldsymbol{X}$ represents the assembled global vector of primary variables, and $\boldsymbol{M}$ is the lumped mass matrix. A derivation of the residual contributions at the element level $\boldsymbol{r}_{int}$ and $\boldsymbol{r}_{ext}$ can be found in [12]. These residual contributions are assembled using a three-point GAUSS quadrature rule. Finally, the time discretization scheme used to solve Equation 3.7 is the NEWMARK method previously described by Equation 2.85.

3.2.3. Contact detection

A contact event occurs between two beams when the impenetrability condition, as derived in Subsection 2.3.8 and restated in Equation 3.8, is violated.

$$g = d_{bl} - (R_1 + R_2) \geq 0 \tag{3.8}$$

To evaluate a given pair of elements' admissibility to the impenetrability condition, a linear nearest-neighbour search is employed. A visual summary of the nearest-neighbour algorithm is presented in Figure 3.1 below.

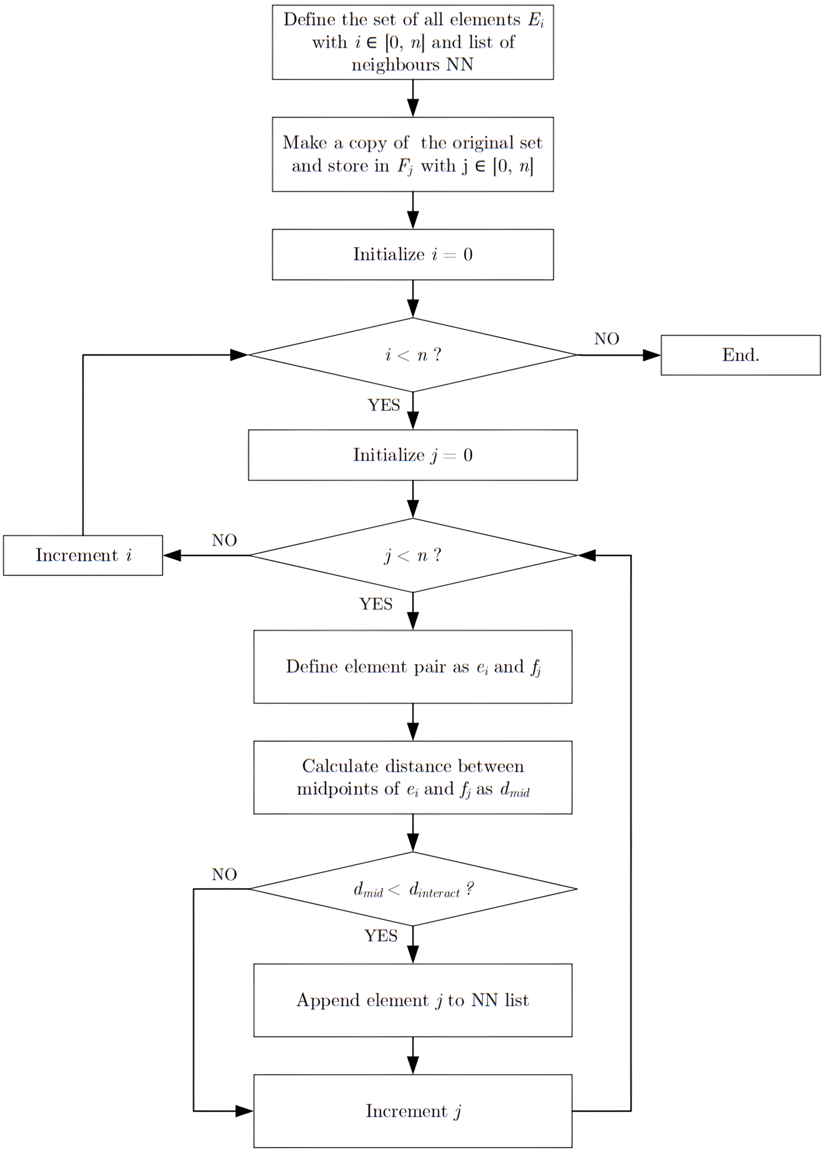

Figure 3.1: Nearest-neighbour algorithm flowchart

The interaction distance between elements is defined as $d_{interact} = h_{max} + (R_i + R_j)$, where h_{max} is the maximum element length determined by the mesh. The search process outlined in Figure 3.1 reduces the search space for prospective contact pair candidates. The nearby pairs in the completed nearest-neighbour list are then tested against the condition stated in Equation 3.8. If this condition is violated, then the beam pair is found to be in contact and the algorithm proceeds with the DCR method, which will be elaborated upon in Subsection 3.2.4. This entire procedure is executed at every time step.

3.2.4. Implementation

First research sub-task

Modelling beam-to-beam contact using the DCR method.

Once contact has been detected between two beams, with the *leader* denoted by subscript ξ and the *follower* by subscript η, the DCR process commences. Consider the following collision scenario:

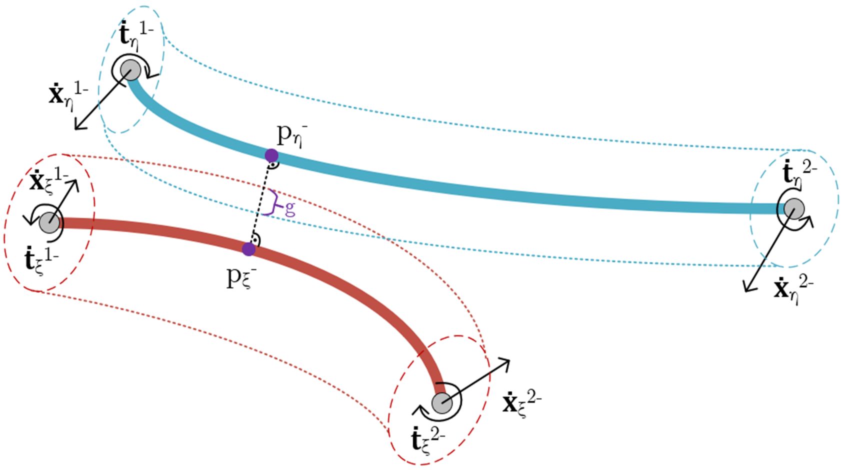

Figure 3.2: Kinematic quantities for a follower-leader beam pair in contact

As shown in Figure 3.2 above, each node has a linear velocity $\dot{\boldsymbol{x}}_{\xi,\eta}^{1,2}$ and tangent time derivative $\dot{\boldsymbol{t}}_{\xi,\eta}^{1,2}$ at the moment before impact. The gap function $\boldsymbol{g}$ is a vector corresponding to the amount of interpenetration occurring between the beams. $\boldsymbol{g}$ is therefore coincident with the bilateral minimum distance vector. Note that each node also has a mass m and moment of inertia I associated with it.

It should be noted that the terms *mass* and *moment of inertia* are not strictly accurate due to the special mass lumping technique employed. Given that each node has six degrees of freedom, mass lumping approximates the continuous mass distribution ρ as discrete quantities. These can be further divided into concentrated mass-like quantities that resist linear motion and concentrated moment-of-inertia-like quantities that resist angular motion about the node. For clarity, these values will be referred to using the terminology of their continuous analogs. The velocity vector and mass matrix now fully define the input for the DCR method.

The intended output of the DCR procedure is twofold. Firstly, the system is modified such that the intersection is removed. This is accomplished by rigidly translating the follower beam by $\boldsymbol{g}$ (a proposed alternative approach for removing the intersection is presented in Section 3.4). Secondly, the post impact velocities are calculated according to the momentum decomposition procedure previously outlined in Subsection 2.3.6. This procedure begins with the assembly of the pre-impact momenta in order to first find the normal component of the post-impact momentum. In accordance with Equation 2.79, the pre-impact momentum vector, the mass matrix, and the gradient of the constraint function must first be assembled.

The pre-impact momentum $\boldsymbol{p}_{\text{tot}}^{-}$ is defined as $\boldsymbol{M}\dot{\boldsymbol{x}}$, where the mass matrix is given by:

$$\boldsymbol{M} = \begin{bmatrix} m_\xi^1 & 0 & 0 & 0 & 0 & 0 & 0 & 0 \\ 0 & I_\xi^1 & 0 & 0 & 0 & 0 & 0 & 0 \\ 0 & 0 & m_\xi^2 & 0 & 0 & 0 & 0 & 0 \\ 0 & 0 & 0 & I_\xi^2 & 0 & 0 & 0 & 0 \\ 0 & 0 & 0 & 0 & m_\eta^1 & 0 & 0 & 0 \\ 0 & 0 & 0 & 0 & 0 & I_\eta^1 & 0 & 0 \\ 0 & 0 & 0 & 0 & 0 & 0 & m_\eta^2 & 0 \\ 0 & 0 & 0 & 0 & 0 & 0 & 0 & I_\eta^2 \end{bmatrix} \tag{3.9}$$

and the velocity vector is given by:

$$\dot{\boldsymbol{x}} = \begin{bmatrix} \dot{\boldsymbol{x}}_\xi^1 & \dot{\boldsymbol{t}}_\xi^1 & \dot{\boldsymbol{x}}_\xi^2 & \dot{\boldsymbol{t}}_\xi^2 & \dot{\boldsymbol{x}}_\eta^1 & \dot{\boldsymbol{t}}_\eta^1 & \dot{\boldsymbol{x}}_\eta^2 & \dot{\boldsymbol{t}}_\eta^2 \end{bmatrix}^T \tag{3.10}$$

Next, the gradient function is defined as the difference between the solution of the bilateral minimum distance function and the sum of the radii:

$$g(\boldsymbol{x}_\xi^1, \boldsymbol{t}_\xi^1, \boldsymbol{x}_\xi^2, \boldsymbol{t}_\xi^2, \boldsymbol{x}_\eta^1, \boldsymbol{t}_\eta^1, \boldsymbol{x}_\eta^2, \boldsymbol{t}_\eta^2) = d_{bl} - (R_1 + R_2) \tag{3.11}$$

where d_{bl} was previously defined in Equation 2.87. Inserting Equation 2.87 into Equation 3.11 yields:

$$g(\boldsymbol{x}) = \left\| \left(\sum_{i=1}^{2} N_x^i(\eta_c)\boldsymbol{x}^i + \frac{l}{2} \sum_{i=1}^{2} N_t^i(\eta_c)\boldsymbol{t}^i \right) - \left(\sum_{i=1}^{2} N_x^i(\xi_c)\boldsymbol{x}^i + \frac{l}{2} \sum_{i=1}^{2} N_t^i(\xi_c)\boldsymbol{t}^i \right) \right\| - (R_1 + R_2) \tag{3.12}$$

Taking the gradient of Equation 3.12 with respect to each degree of freedom gives the following vector:

$$\nabla g = \alpha \begin{bmatrix} -N_x^1(\xi_c) \\ -\frac{l}{2}N_t^1(\xi_c) \\ -N_x^2(\xi_c) \\ -\frac{l}{2}N_t^2(\xi_c) \\ N_x^1(\eta_c) \\ \frac{l}{2}N_t^1(\eta_c) \\ N_x^2(\eta_c) \\ \frac{l}{2}N_t^2(\eta_c) \end{bmatrix} \tag{3.13}$$

where $N_x^{1,2}$ and $N_t^{1,2}$ correspond to the HERMITE shape functions previously defined in Equation 3.6. Additionally, differentiation results in a constant α which expands to:

$$\alpha = \frac{1}{2\sqrt{[\boldsymbol{r}_1(\xi_c) - \boldsymbol{r}_2(\eta_c)] \cdot [\boldsymbol{r}_1(\xi_c) - \boldsymbol{r}_2(\eta_c)]}} \tag{3.14}$$

Inserting $\boldsymbol{p}_{\text{tot}}^{-}$, $\boldsymbol{M}$, and ∇g into Equation 2.79 gives the normal component of the system's momentum prior to impact. The tangential component can readily be calculated using equation Equation 2.80. These can then be added together to represent the total system momentum prior to impact.

Since the system has now effectively been reduced to a one-dimensional problem, the next step is to use the concepts of momentum and kinetic energy conservation for a perfectly elastic collision between particles ξ and η. The calculation of the total system momentum after impact is given by:

$$\begin{bmatrix} \boldsymbol{p}_\xi^+ \\ \boldsymbol{p}_\eta^+ \end{bmatrix} = \frac{1}{m_\xi + m_\eta} \begin{bmatrix} m_\xi - m_\eta & 2m_\xi \\ 2m_\eta & m_\eta - m_\xi \end{bmatrix} \begin{bmatrix} \boldsymbol{p}_\xi^- \\ \boldsymbol{p}_\eta^- \end{bmatrix} \tag{3.15}$$

Finally, the post-impact velocities $\dot{\boldsymbol{x}}^+$ are obtained by dividing out the nodal masses from the total post-impact momentum. The velocities computed from the DCR method are subsequently used in the corrector step of the solver, as illustrated in Figure 2.20. Upon completing these steps, the final state of the contact pair at the end of the time step features momentum-conserving post-impact velocities and the elimination of interpenetration, as shown in Figure 3.3 below:

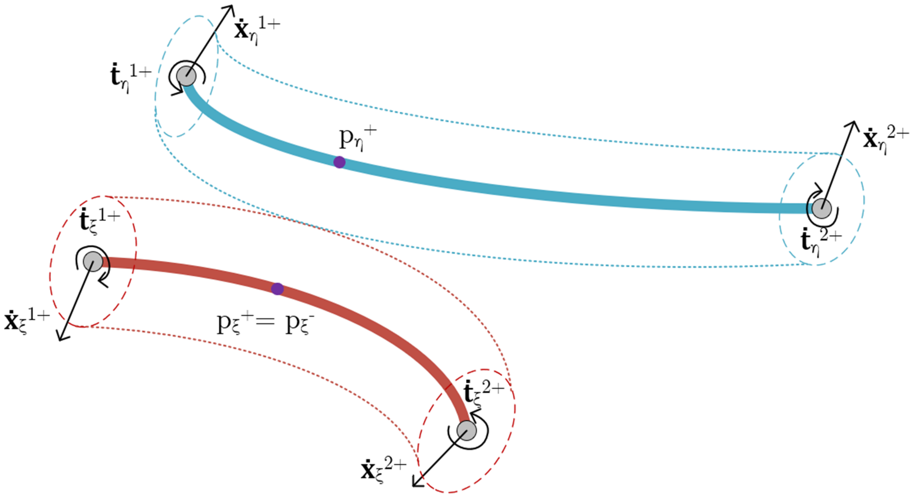

Figure 3.3: Post-impact kinematic quantities for a follower-leader beam pair in contact via DCR

3.2.5. Nonlinear buckling

Since the target application of this study is for soft truss-based lattices, the buckling and post-buckling behaviour of struts in compression is of great importance. The selection of a hyperelastic constitutive model means that beams can undergo large elastic deformations, including recoverable buckling [6]. Since the expected outcome of the main use case — a compliant insideBCC cell being compressed — both geometric and material nonlinearities are anticipated.

Consider the following unit insideBCC cell subject to displacement-controlled compression:

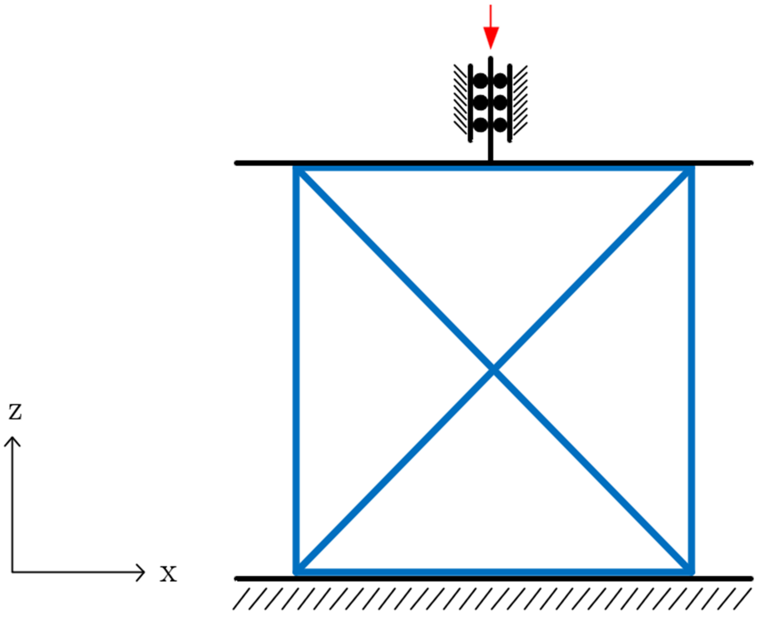

Figure 3.4: Front orthogonal view representation of the boundary conditions on a unit insideBCC cell with side length L = 10 cm

As shown in Figure 3.4 above, the nodes on the bottom beams are fully clamped, while the nodes on the top beams are displacement controlled via a roller which restricts lateral displacement. To enable nonlinear buckling in this scenario, small imperfections were randomly introduced directly on the mesh. This was accomplished by randomly displacing each node of the mesh by a perturbation δ in the plane normal to the beam's axis. For instance, the nodes on the vertical beams (whose axes are parallel to the z coordinate axis), can either be displaced in x or y. The magnitude of the imperfections is on the order of 10^{-7} m. This value was empirically determined by running static compression tests with increasing imperfections until buckling was observed. Randomness was generated via a pseudo-random number generator. The resulting imperfection distribution is uniform and consequently does not favour any specific buckling mode, as in the case in linear buckling analyses. In this example, the loading rate was set to 2 mm/s in the negative z direction and the unit cell was compressed to 90% of its original height. The results of this simulation are shown below in Figure 3.5.

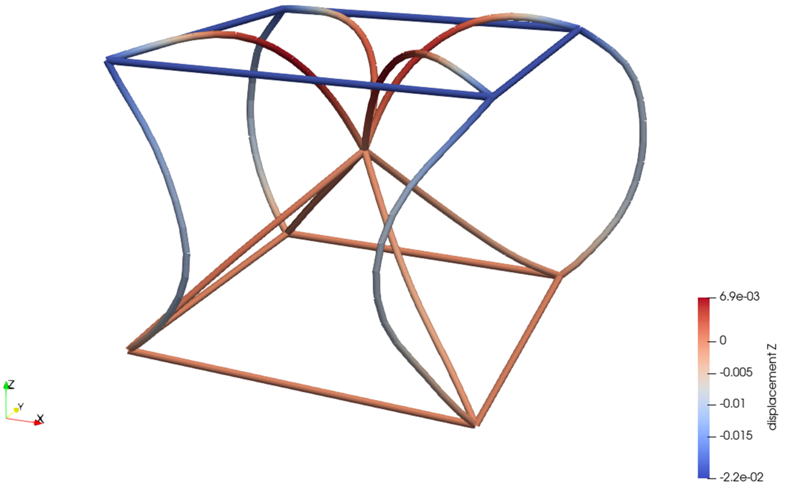

Figure 3.5: z-displacement colour map for a buckled insideBCC cell

From Figure 3.5, it is apparent that most of the beams have buckled. As expected for a relatively slow loading rate, the beams exhibiting buckling fall into their first mode shape. It should be noted that the material of these beams is quite compliant (E = 1 GPa). A key feature to note in Figure 3.5 is the out-of-plane buckling direction taken by the vertical beams. Each vertical beam buckles in a different direction, confirming that the random imperfection distribution did not affect the buckling shape. The resulting force-displacement curve for this simulation is shown below in Figure 3.6.

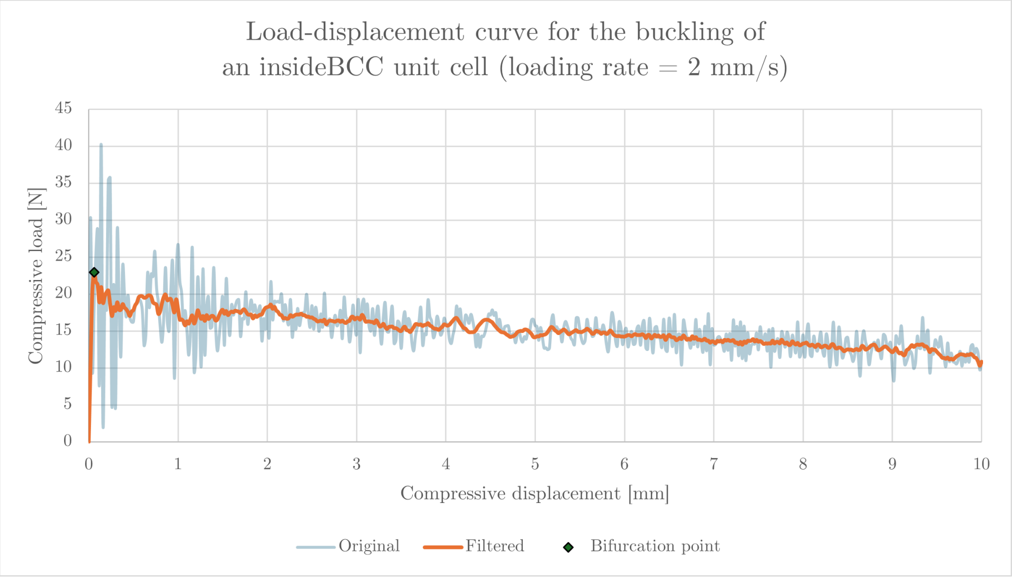

Figure 3.6: Load-displacement curve for a unit insideBCC cell subject to a compressive loading of 2 mm/s

The response shown in Figure 3.6 displays the characteristic buckling response of thin beams. A clear bifurcation point can be noted almost immediately. The highly compliant vertical beams settle into their post-buckling equilibrium state and the force following this point remains nearly constant. It should be noted that, due to the dynamic loading at a rate of 2 mm/s, the force response to the displacement-controlled simulation is quite noisy. For this reason, the signal was filtered with a moving average over 10 loading steps.

3.2.6. Modelling lattice joints

Since the focal point of this thesis is to assess the feasibility and performance of a proposed new contact algorithm for thin beams, the complex topic of joint-modelling has been deferred to subsequent iterations. The importance of capturing the stiffness of joints was highlighted in Subsection 2.1.2, however, the implementation of such joints is not trivial. Instead, lattice structures in this study are modelled with simple pin joints.

A pin joint *ties* beam elements together in a manner that does not restrict rotation. At the solver level, a group of n elements which share a node are perceived as one *parent* node and $n - 1$ *child* nodes. Child nodes inherit kinematic quantities from their parent node. This means that an element connected to a joint shares the same position, velocity, and acceleration as all other elements connected to the same joint at that node. A key point to note is that the selected beam formulation is also characterized by the nodal tangent. For a simple pin, these tangents are not shared by the parent node to its children. Therefore, the rotational degree of freedom is not prescribed, which then allows elements to rotate around a joint if they so please.

The use of pin joints is an obvious limitation when modelling truss-based architected materials, which of course have stiff joints. This represents a significant deficit in the structural stability of a lattice modelled with pin joints and must be scrutinized when analyzing the response of said structure to any load. To mitigate this flaw in the lattice modelling, only load paths aligned with the orthogonal planes of the lattice are considered.

Another important assumption regarding the joints of the studied lattices is that elements with a joint node are excluded from contact consideration. This decision was motivated by observations in early iterations of the model, where non-physical contact was detected at the joints. When contact was identified at a joint, the DCR algorithm attempted to reposition the beams to eliminate the contact, which contradicts the fundamental purpose of the joint — to connect and fix the beams' positions. This scenario, analogous to an immovable object encountering an unstoppable force, inevitably led to the solver's immediate failure.

A temporary solution was implemented whereby elements with one or more joint nodes are flagged, and if a given element pair has a flagged element, it is excluded from contact consideration. This is shown schematically in an example of a beam coming into contact with a simple cubic lattice in Figure 3.7 below.

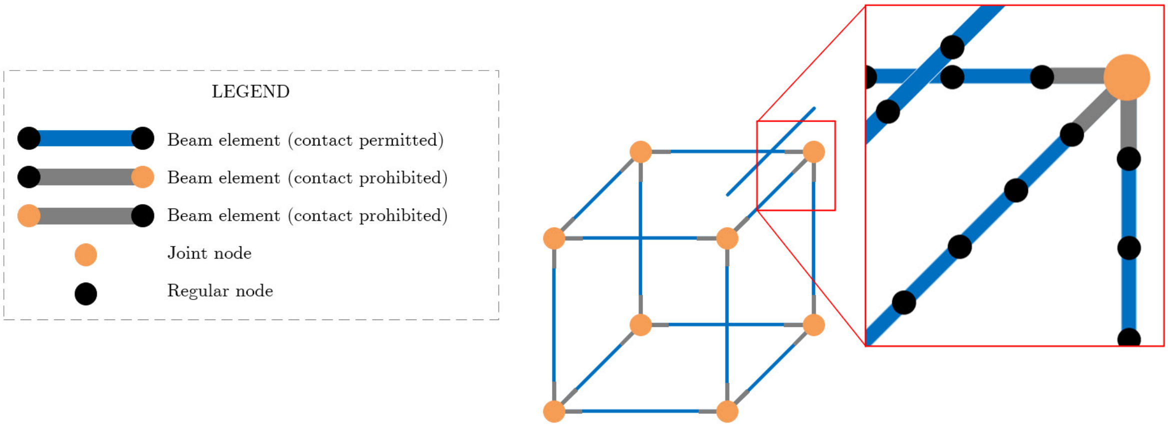

Figure 3.7: Contact inclusion convention for elements near lattice joints

In Figure 3.7, the grey elements indicate those identified as having a joint and, therefore, will be excluded from the contact search algorithm. This is a major assumption that renders the DCR implementation vulnerable to missed contact events. However, with a suitably fine mesh, the likelihood of true contact events occurring at these locations can be significantly minimized. Nonetheless, this simplification remains a potential source of error and should be further investigated and improved in future iterations.

3.2.7. Key assumptions

To better contextualize the applied methodology of this work, the following list delineates the key assumptions made. Listing these assumptions prior to the presentation of results is vital for better comprehension of the findings. Accordingly, the DCR method for modelling contact between slender beams is based on the following major assumptions and idealizations. Note that a reference to the subsection that motivates these assumptions is provided in parentheses for each item.

- The beam elements are considered as slender continua and follow the torsion-free Kirchhoff–Love formulation (Section 3.1).
- A hyperelastic constitutive law is used to model compliant media resembling elastomers (Subsection 2.2.5).
- The chosen time step is assumed to be sufficiently small, ensuring that any work introduced into the system by removing intersections is negligible (Subsection 2.3.6).
- All contact events are perfectly elastic, *i.e.*, $e = 1$ (Subsection 2.3.6).
- All contact events are frictionless (Subsection 2.3.6).
- Material imperfections are randomly distributed throughout the continuum. The magnitude of these imperfections was empirically selected to be approximately 0.01% of the beam's radius (Subsection 3.2.5).
- All joints are modelled as perfect pins (Subsection 3.2.6).
- Beam elements that have one node coinciding with a joint a prohibited from participating in contact (Subsection 3.2.6).

3.3. Code development

All tools developed in this study were done so within the context of the *summit* code base. The summit finite element framework was originally written in C++ and built by researchers at the Massachusetts Institute of Technology, then further developed by Dr. Bianca Giovanardi for use in her computational mechanics research team at TU Delft. Among its many notable applications present in the literature are the use of the discontinuous Galerkin method for modelling nonlinear mechanics [54], fluid-structure interactions [55], and parallel computing [56].

Summit's wide-ranging applications leverage the many benefits of object-oriented programming (OOP) afforded by C++. OOP is highly advantageous for team-based software development due to its modularity and code reuse features like classes and inheritance. Its performance and efficiency make it ideal for high-speed, resource-demanding applications. Moreover, summit's prominent use of C++ allows cross-platform compatibility and portability. While a comprehensive explanation of summit's entire architecture is complex and beyond the scope of this report, the novel contributions of this thesis will be illustrated in the context of the broader system. Figure 3.8 below provides a simplified overview of the code architecture and highlights modules that have been modified.

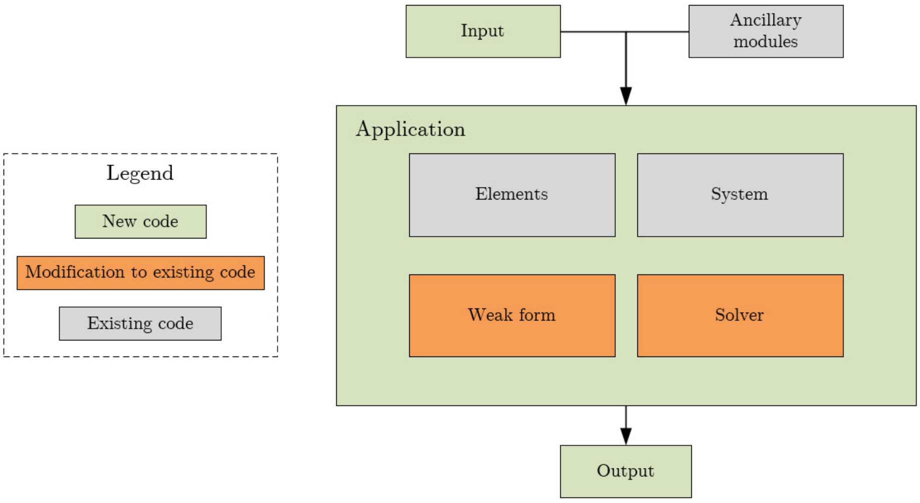

Figure 3.8: High-level overview of summit framework

A brief summary of the modules mentioned in Figure 3.8 are provided below:

- *Input* represents the all pre-processing steps such as meshing, material definitions, and other system parameters.
- *Ancillary systems* represents all support code needed for a summit application to run.
- *Elements* provides the definition for the selected element type in the application.
- *System* defines the type of physical system (*e.g.*, dynamic with contact) used in the application.
- *Weak form* contains all the code necessary to represent the mechanics of the system and to construct the weak form of the governing equations.
- *Solver* is responsible for the implementation of the desired numerical solver.
- *Output* is the unprocessed data resulting from the application's execution.

As indicated by the legend key in Figure 3.8, much of the code has been repurposed, while some modules required heavy modification to accomplish the novel implementation. The three applications that have been built over the course of this study make use of the novel DCR beam-to-beam contact method.

3.4. An alternative intersection removal approach

The process for eliminating intersections between contacting elements, detailed in Subsection 3.2.4 and hereinafter referred to as the *rigid translation* method, is adopted for the rest of this study. A novel approach was also investigated and tested in a prototype, however, it was not implemented in the final formulation due to time constraints. This section serves to shed more light on this proposed approach for its potential use in future applications. The new approach, called the *polynomial interpolation* method, offers a higher-fidelity alternative to handling element intersections. Rather than displacing nodal positions, this method seeks to modify only the tangents of the nodes on the follower element. This is accomplished by first rigidly translating the contact point, then fitting the follower beam's centreline with the newly displaced contact point by modifying the endpoint tangents.

To illustrate the novelty of the proposed method, consider an arbitrary pair of beams that are in contact:

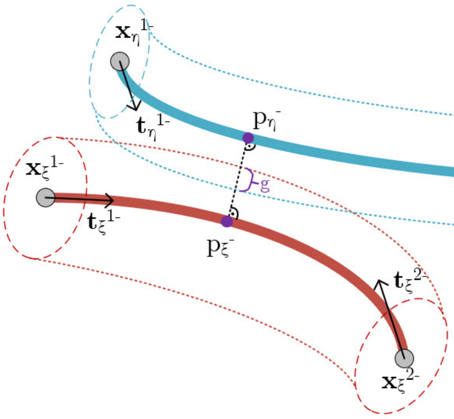

Figure 3.9: Pre-DCR configuration of a leader-follower (red-blue) beam pair in contact

Applying the conventional rigid translation approach to remove intersections results in a post-DCR system wherein only the nodal positions of the follower beam, $\boldsymbol{x}_\eta^1$ and $\boldsymbol{x}_\eta^2$ are modified in the process. In Figure 3.10 below, the quantities depicted in orange represent those that have been modified by the application of DCR.

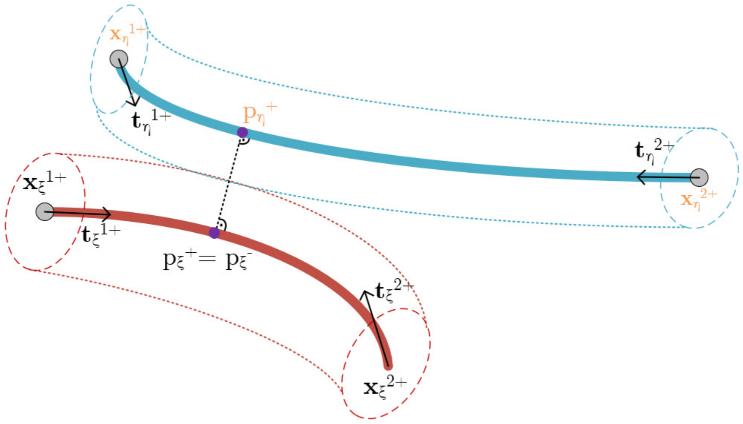

Figure 3.10: Post-DCR configuration of a leader-follower (red-blue) beam pair in contact using the rigid translation removal technique

Applying the so-called polynomial interpolation method to the contact system given by Figure 3.9 results in a slightly different post-DCR scenario than the one depicted in Figure 3.10. Instead of modifying $\boldsymbol{x}_\eta^1$ and $\boldsymbol{x}_\eta^2$ to accommodate the new contact point p_η^+, the tangents on the follower beam, $\boldsymbol{t}_\eta^1$ and $\boldsymbol{t}_\eta^2$ receive the update. This is reflected in Figure 3.11 below, with the updated quantities again highlighted in orange.

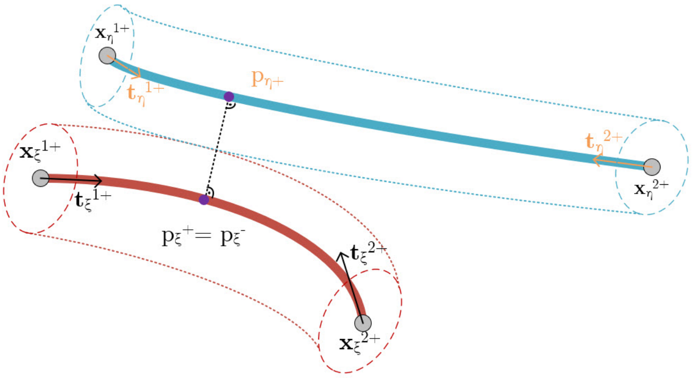

Figure 3.11: Post-DCR configuration of a leader-follower (red-blue) beam pair in contact using the polynomial interpolation removal technique

This polynomial interpolation technique is facilitated by the fact that the displacement field across the beam domain is described by a third-order polynomial via HERMITE shape functions. This means that the curve representing the beam's centreline can be entirely described by the positions and tangents at the endpoints. Recall that any point p along the length of an element can be described in terms of the element parameter $\xi \in [-1, 1]$:

$$p = \sum_{i=1}^{2} N_x^i(\xi) \cdot \boldsymbol{x}^i + \frac{l}{2} \sum_{i=1}^{2} N_t^i(\xi) \cdot \boldsymbol{t}^i \tag{3.16}$$

The generic definition for any cubic polynomial as a function of parameter τ can be written in terms of the following parametric equation:

$$p(\tau) = a_3\tau^3 + a_2\tau^2 + a_1\tau + a_0 \tag{3.17}$$

where the coefficients $a_i, b_i, c_i \in \mathbb{R}$ are scalar values. For simplicity, the domain of τ is set to match that of ξ. If four such points are known to reside on this curve, Equation 3.17 can be assembled in matrix form and re-written as:

$$\begin{bmatrix} p_1 \\ p_2 \\ p_3 \\ p_4 \end{bmatrix} = \begin{bmatrix} \tau^3 & \tau^2 & \tau & 1 \\ \tau^3 & \tau^2 & \tau & 1 \\ \tau^3 & \tau^2 & \tau & 1 \\ \tau^3 & \tau^2 & \tau & 1 \end{bmatrix} \begin{bmatrix} a_3 \\ a_2 \\ a_1 \\ a_0 \end{bmatrix} \tag{3.18}$$

$$\boldsymbol{p} = \boldsymbol{V}\boldsymbol{a}$$

If the coordinates of the four points are known in Equation 3.18, then the coefficient vector can be obtained by simply inverting $\boldsymbol{V}$ and multiplying by the vector $\boldsymbol{p}$.

Now consider the scenario previously introduced in Figure 3.11. Under the proposed framework, the objective is to update the system by modifying only the quantities of the follower beam (blue) that are highlighted in orange. The point $\boldsymbol{p}_\eta^+$ can be readily computed by translating $\boldsymbol{p}_\eta^-$ by the gap vector $\boldsymbol{g}$. By virtue of knowing $\boldsymbol{p}_\eta^+$, the corresponding element parameter η is also known, and hence τ is known. Additionally, notice that the endpoints of the follower beam, $\boldsymbol{x}_\eta^{1+}$ and $\boldsymbol{x}_\eta^{1+}$, are already known. Then, using the form introduced in Equation 3.18, a system of equations could be assembled such that each known point is set equal to the VANDERMONDE matrix $\boldsymbol{V}$ multiplied by the coefficients vector $\boldsymbol{a}$:

$$\begin{bmatrix} p_\eta^+ \\ x_\eta^{1+} \\ x_\eta^{2+} \end{bmatrix}_i = \begin{bmatrix} \tau^3 & \tau^2 & \tau & 1 \\ \tau^3 & \tau^2 & \tau & 1 \\ \tau^3 & \tau^2 & \tau & 1 \end{bmatrix}_i \begin{bmatrix} a_3 \\ a_2 \\ a_1 \\ a_0 \end{bmatrix}_i \tag{3.19}$$

$$\boldsymbol{p}_i = \boldsymbol{V}_i \boldsymbol{a}_i \quad \text{for } i = x, y, z$$

If solved independently in dimensions x, y, z, Equation 3.19 can be used to obtain the unknown coefficients via $\boldsymbol{a}_i = \boldsymbol{V}_i^{-1}\boldsymbol{p}_i$ for $i = x, y, z$. Since only three control points are known for the desired interpolation, the VANDERMONDE matrix is rectangular, and hence, uninvertible. Without a fourth control point, Equation 3.19 represents an underdetermined system, *i.e.*, there are more unknowns than equations. This implies that there is no unique solution for $\boldsymbol{\tau}$ which satisfies the linear system of equations. Fortunately, there is a mathematical technique that can be applied to recover a unique solution to this equation by imposing an extra constraint. This technique is the so-called *least-squares* method. It has been proven by Penrose that the best solution to this underdetermined system is the one that minimizes the norm of $\boldsymbol{a}$ [57]. This can alternatively be formulated using the *pseudo-inverse* of $\boldsymbol{V}$, denoted $\boldsymbol{V}^{\dagger}$. The pseudo-inverse operation on $\boldsymbol{V}$ results in a matrix $\boldsymbol{V}^{\dagger}$ which is square, hence the modified system becomes independent and consistent [57]:

$$\boldsymbol{a}_i = \boldsymbol{V}_i^{\dagger}\boldsymbol{p} \tag{3.20}$$

If the $\boldsymbol{a}$ vectors in Equation 3.20 can be obtained, then they may be transformed into the corresponding HERMITE form using simple algebraic manipulation. In doing so, the post-impact tangents of the follower beam would be known, and hence the intersection removal process would be concluded. The challenge, however, lies in the numerical implementation of an appropriate method to solve Equation 3.20.

Several methods exist for solving the least-squares approximation, *i.e.*, taking the pseudo-inverse of a rectangular matrix $\boldsymbol{V}_{mxn}$ where $m < n$. Among the most popular techniques is by using the singular value decomposition (SVD) of $\boldsymbol{V}$ [58]. SVD works by decomposing $\boldsymbol{V}$ into the form $\boldsymbol{Q_1 \Sigma Q_2}$, where $\boldsymbol{Q_{1,2}}$ are orthogonal matrices, while $\boldsymbol{\Sigma}$ is a diagonal matrix (for further information on the method, the author recommends consulting the proof presented by Strang) [58]. The main drawback of using SVD to recover the pseudo-inverse of $\boldsymbol{V}$ is that the method necessitates the use of an eigenvalue analysis. This fact presents an obstacle from the perspective of numerical implementation. One possible technique for obtaining the eigenvalues is via JACOBI or GAUSS-SEIDEL iteration methods [58]. Although these methods are relatively simple in their implementation, they are, in general, unstable and do not guarantee convergence. Therefore, further investigation into the robustness of the least-squares approach to fitting the cubic polynomial should be conducted before applying it in the context of intersection removal for DCR.

4

Verification

Second research sub-task

Verifying that the DCR formulation accurately and consistently conforms to the laws of contact mechanics.

Two verification cases are selected to demonstrate the performance of the novel DCR method for contact between torsion-free KIRCHHOFF–LOVE beams. The purpose of verification in this case is threefold. First, it is necessary to confirm the mathematical accuracy of the solution by comparing the finite element results with a known analytical solution. Second, verification is crucial for demonstrating software functionality and ensuring that the novel method operates as intended without any bugs. Third, it serves to evaluate the convergence and stability of the newly developed algorithm.

4.1. Case I: collision between untethered beams

The first verification case is meant to emulate an elastic collision between particles. It has been established in Subsection 3.2.4 that the DCR beam-to-beam algorithm reduces to a particle collision at the element level. If this is true, then a simple collision between stiff beams should match the results of a particle collision with the same masses and initial velocities. The initial setup in Figure 4.1 shows the two beams with free ends prior to contact.

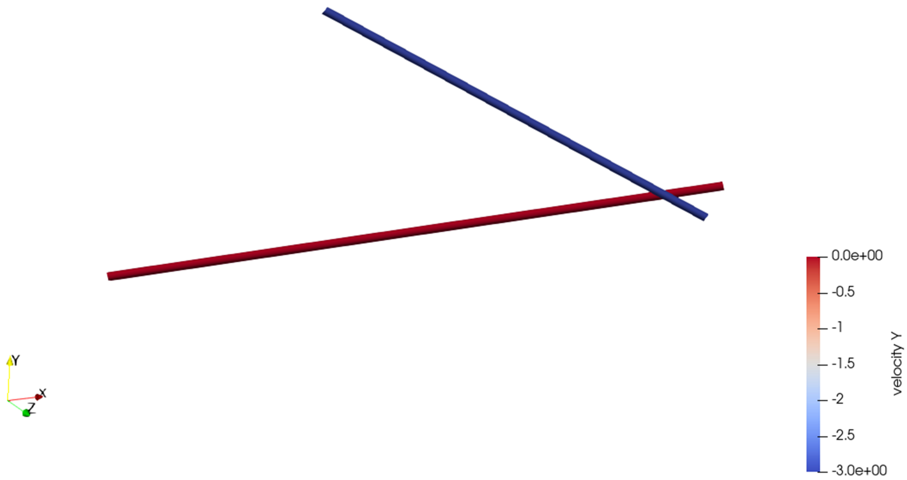

Figure 4.1: Setup of verification case I displaying initial y-velocity

The key features of this simulation are summarized below in Table 4.1.

Table 4.1: Case I system properties at its initial state

Beam	Beam length [m]	Radius [m]	Mass density [kg/m^3]	YOUNG's modulus [GPa]	Initial z-velocity [m/s]
Cantilever	1.0	0.01	1000	200	0
Impactor	1.0	0.01	500	200	-3.0

Note that a time step of 1.0e-6 seconds was used for all verification runs. Furthermore, all simulations in this section have a mesh resolution of 20 elements per beam. It has been verified that these spatial and temporal resolutions result in a converging solution.

For a frictionless elastic collision between particles, the conservation of momentum and kinetic energy can be applied to solve post-impact velocities. Consider a system with two particles where, prior to impact, the first particle is stationary, and the second particle is travelling at 3 m/s toward the first particle. Let the mass of the second particle be half that of the first. In a perfectly elastic collision, this scenario would result in the first particle having a final velocity of 2 m/s in the same direction that the second particle was initially travelling, while the second particle would change directions and have a velocity of 1 m/s. This scenario is summarized schematically in Figure 4.2

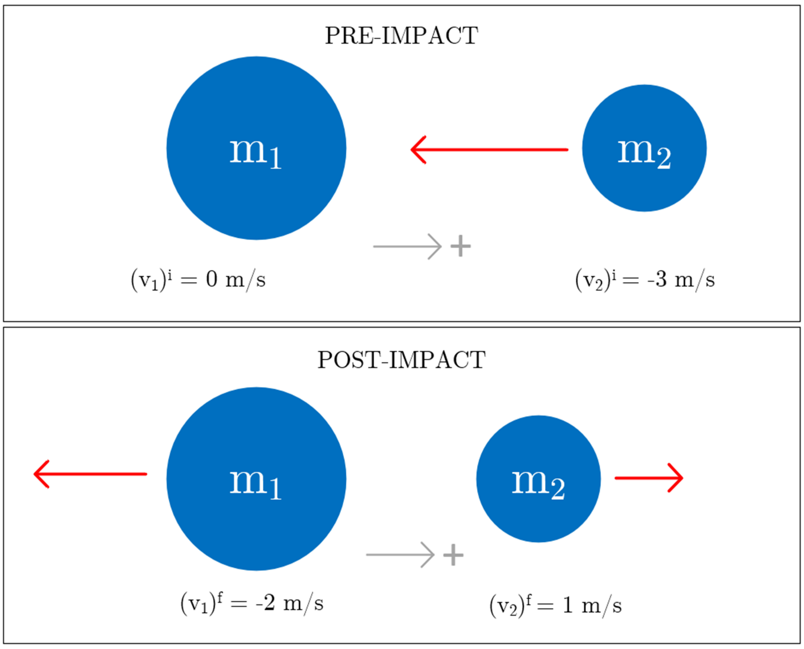

Figure 4.2: Example of an elastic collision between particles in one dimension

The first verification case is designed to emulate the scenario described in Figure 4.2. Observing the state of the system post-impact (see Figure 4.3) reveals that the contact algorithm correctly resolves the post-impact quantities predicted by the particle analog. This is to be expected, since the DCR algorithm's post-impact velocities have been derived from the particle collision. Moreover, since the stiffness of the beams has been set to a large value (E = 200 GPa), the inertial effects of bending do not significantly affect the post-impact velocities.

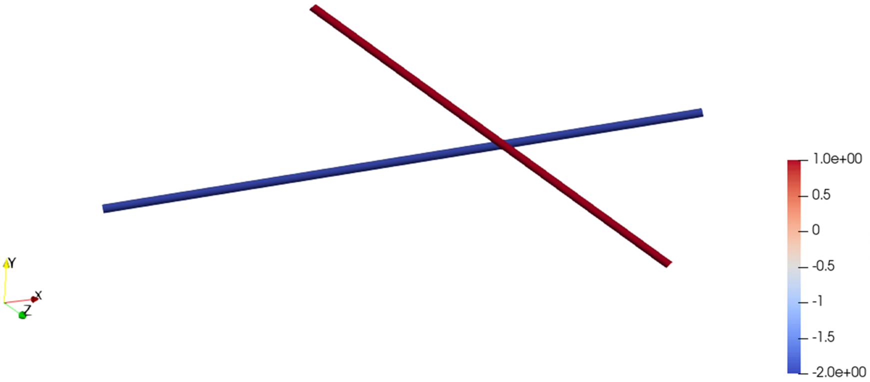

Figure 4.3: Results of verification case I displaying final y-velocity

4.2. Case II: cantilever response to impact

The purpose of case II is to evaluate beam contact in a slightly more complex setting. Since DCR does not work by imposing a contact force, the verification process is limited to measurable kinematic quantities, namely, velocities. Suppose a cantilever beam is struck by a mass at half its span. The DCR method dictates that the velocity at the point of contact post-impact should be updated in a manner that conserves momentum. Therefore, if the vibration response of the cantilever matches the analytical case and the direct initial velocity simulation, then the contact enforcement method is verified. The method of direct initial velocity simulation captures the response of the cantilever to an initial condition imposed on the nodes of the beam, which corresponds to the expected post-impact velocity. In this case, the initial velocity is set to -2 m/s.

To begin the setup of case II, case I is modified to have one end of the stationary beam fixed (previously shown as the blue beam in Figure 4.1), thus making it a cantilever. The impactor (red) is unchanged from Figure 4.1's setup and both beams retain the same properties introduced in Table 4.1. The simple cantilever beam is shown schematically in Figure 4.4 below.

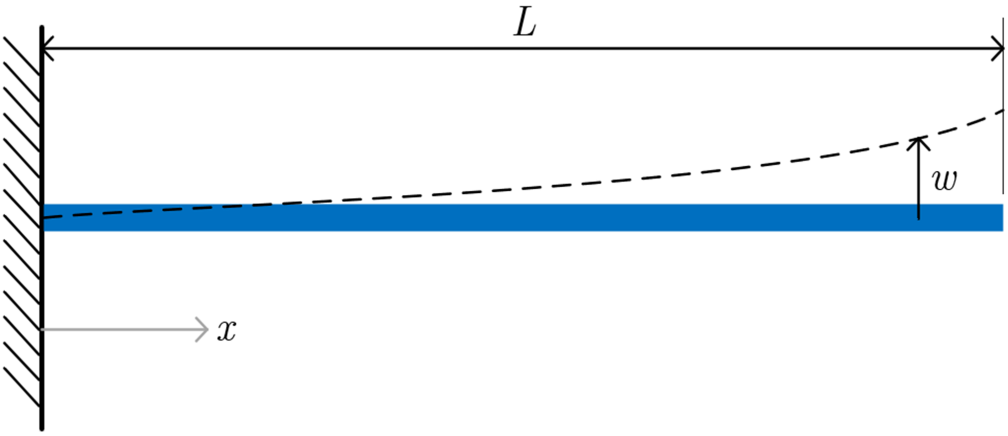

Figure 4.4: Schematic of a cantilever beam showing deflection w

When the simulation is run with the DCR method, the momentum-preserving velocity changes are implemented at the time step corresponding to impact. This is confirmed visually by Figure 4.5, which shows the velocity contours on both beams at the time step immediately following contact. This scenario is hereinafter denoted case IIa. To set up the comparison, which is to follow in the next section, the initial velocity response and analytical responses are denoted case IIb and case IIc, respectively.

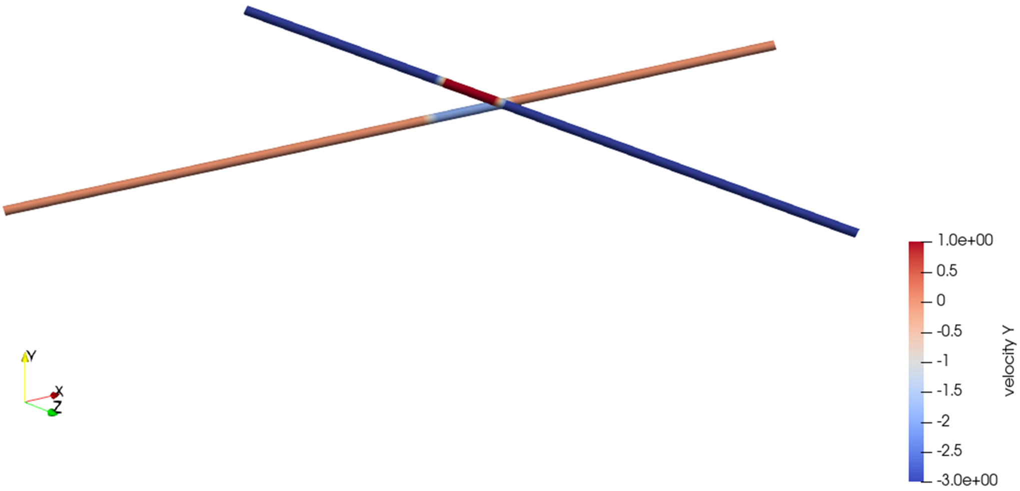

Figure 4.5: y-velocities at the moment immediately following impact (case IIa)

On the cantilever beam (lower), a localized region near the impact zone is shown to have a value of -2 m/s, while the impactor displays a velocity of 1 m/s at the moment immediately following impact. To analyze the resulting displacement response for case II, the analytical solution must first be derived.

4.2.1. Analytical solution

There exists an analytical solution that describes the response of a cantilever beam when an initial velocity is specified at any point along its span [59]. If the assumption of small deflections is made, then EULER-BERNOULLI beam theory can be applied to describe vibrations with the following classical PDE:

$$EI\frac{\partial^4}{\partial x^4}w(x,t) + \rho A\frac{\partial^2}{\partial t^2}w(x,t) = 0 \tag{4.1}$$

where $w(x,t)$ is the transverse displacement, quantity EI is the flexural rigidity, ρ is the mass density, and A is the cross-sectional area of the beam. When boundary conditions are provided for both ends of the beam, it is well known that the solution to the resulting initial value problem (IVP) can be written in the form [59]:

$$w(x,t) = \sum_{m=1}^{\infty} X_m(x)\left(A_m \sin \omega_m t + B_m \cos \omega_m t\right) \tag{4.2}$$

where $X_m(x)$ are the free vibration mode shapes, each harmonically oscillating at their respective modal natural frequency ω_m [59]. Each X_m is thus an eigenfunction, which can be expressed in terms of nondimensional length $\xi = \frac{L}{2}$ and eigenvalues β_m:

$$X_m = \left(\cosh \beta_m \xi - \cos \beta_m \xi\right) - \gamma_m \left(\sinh \beta_m \xi - \sin \beta_m \xi\right) \tag{4.3}$$

Here, γ_m represents the ratio between amplitudes for the m^{th} eigenfunction. Now suppose the system is excited by a known displacement or velocity at $t = 0$. These initial values can be generalized as:

$$w(\xi,0) = f(\xi) \tag{4.4a}$$

$$\frac{\partial}{\partial t}w(\xi,0) = g(\xi) \tag{4.4b}$$

It follows that the coefficients A_m and B_m in Equation 4.2 can be written in terms of the initial displacement and velocity functions Equation 4.4a and Equation 4.4b, giving:

$$A_m = \frac{\int_0^L g(\xi) X_m(\xi) \mathrm{d}\xi}{\omega_m \int_0^L X_m^2(\xi) \mathrm{d}\xi} \tag{4.5a}$$

$$B_m = \frac{\int_0^L f(\xi) X_m(\xi) \mathrm{d}\xi}{\int_0^L X_m^2(\xi) \mathrm{d}\xi} \tag{4.5b}$$

Assuming that the problem does not include an initial displacement, but is given an initial velocity at $x = \frac{L}{2}$, the solution in Equation 4.2 reduces to:

$$w\left(\frac{L}{2}, t\right) = \sum_{m=1}^{\infty} X_m \left(\frac{L}{2}\right) \left(\frac{\int_0^L g\left(\frac{1}{2}\right) X_m\left(\frac{1}{2}\right) \mathrm{d}\xi}{\omega_m \int_0^L X_m^2\left(\frac{1}{2}\right) \mathrm{d}\xi} \right) \sin \omega_m t \tag{4.6}$$

Given the system's material properties and initial excitation, it was determined via trial-and-error that a sum to the fifth mode is sufficient for capturing an accurate response for the analytical case. A comparison of verification case II is presented in Subsection 4.2.2 below.

4.2.2. Response comparison

The three responses, from the DCR impact simulation (case IIa), the initial velocity simulation (IIb), and the analytical solution (case IIc), are combined in Figure 4.6 below.

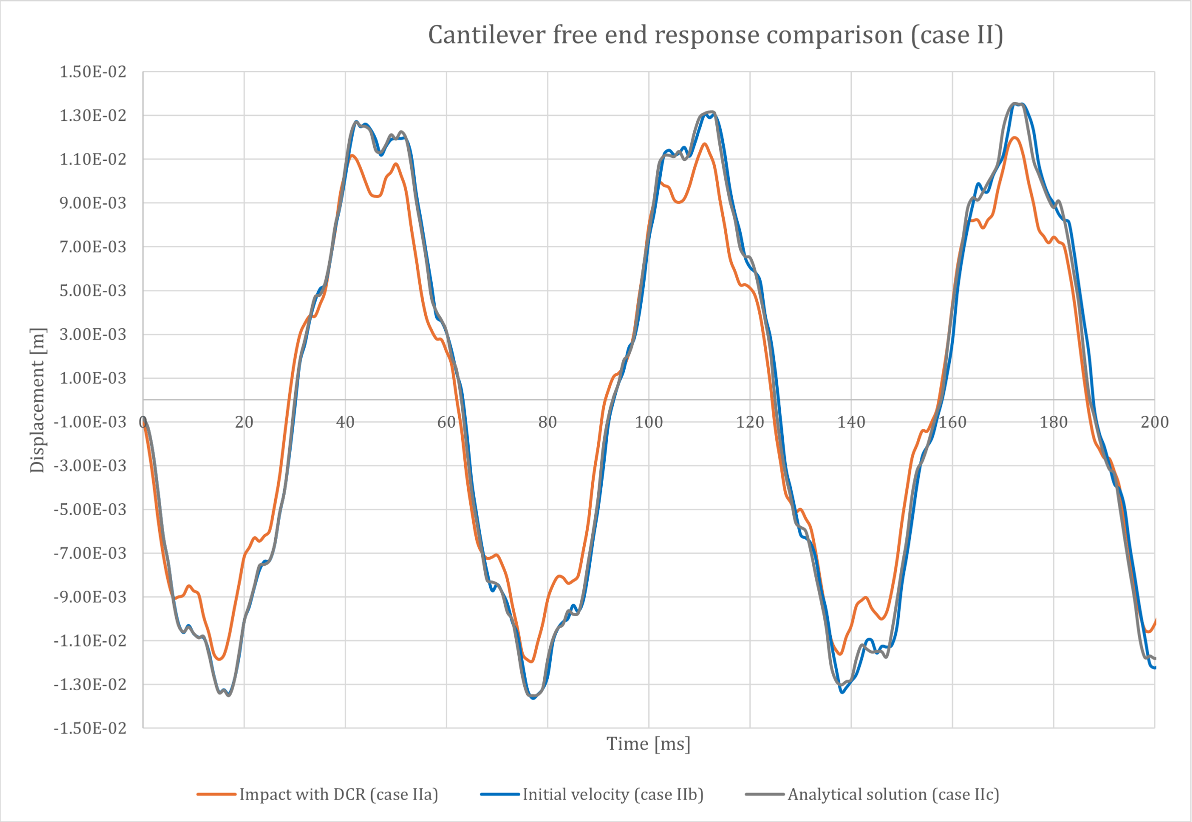

Figure 4.6: Verification case II response comparison

As expected, Figure 4.6 shows that the case IIb and case IIc responses measured from the free end are nearly identical. This confirms the accuracy of the FEM implementation and dynamic solver. However, when examining the impact case IIa, there is a noticeable discrepancy in amplitude compared to the initial velocity response. This difference cannot be explained by the graph alone but becomes clear by visual inspection of the simulation results. Unlike verification case I, the cantilever beam in case II is fixed at one end. The resulting oscillations on the cantilever have a greater amplitude than the linear velocity of the impactor post-impact. Consequently, subsequent contact events are possible. This is exactly what the simulation shows when the contact events are printed at each time step. Following the first impact, several succeeding impacts occur before the impactor moves out of range of the oscillating cantilever. This behaviour is reflected by the smaller amplitude seen for the orange curve in Figure 4.6.

To verify the momentum-preserving properties of the applied DCR method, the total system momentum can be extracted at each time step. To accomplish this, the elemental momenta can be obtained with the use of the following formula:

$$\boldsymbol{p}_{elem} = \int_{-1}^{1} \rho A \left[N_x^1(\xi)\dot{\boldsymbol{x}}^1 + N_x^2(\xi)\dot{\boldsymbol{x}}^2 + \frac{l}{2}N_t^1\dot{\boldsymbol{t}}^1 + \frac{l}{2}N_t^2\dot{\boldsymbol{t}}^2 \right] \frac{l}{2}\mathrm{d}\xi \tag{4.7}$$

Here, the quantities $N_{x,t}^{1,2}$ are the Hermite shape functions previously introduced in Equation 3.6 and l is the length of a given element. The total system momentum at each time step can be computed by simply summing the elemental momenta over all elements in the system as:

$$\boldsymbol{p}_{sys} = \sum_{i=1}^{N} ||\boldsymbol{p}_{elem,i}|| \tag{4.8}$$

where N is the total number of elements in the system. It should be noted that applying the shape functions in Equation 4.7 implies the use of a consistent mass matrix at the system level. This is, of course, not the case since introducing a lumped mass approach. However, it remains a good approximation since the beams have a uniform and undeformable cross-section. Moreover, the discretization, which has exhibited mesh independence, implies a reasonable idealization of continuous mass distribution. Using this approach, it is therefore possible to verify if the DCR-facilitated scenario in case II conserves momentum. Combining Equation 4.7 and Equation 4.8 to the output of case II yields the following total momentum plot:

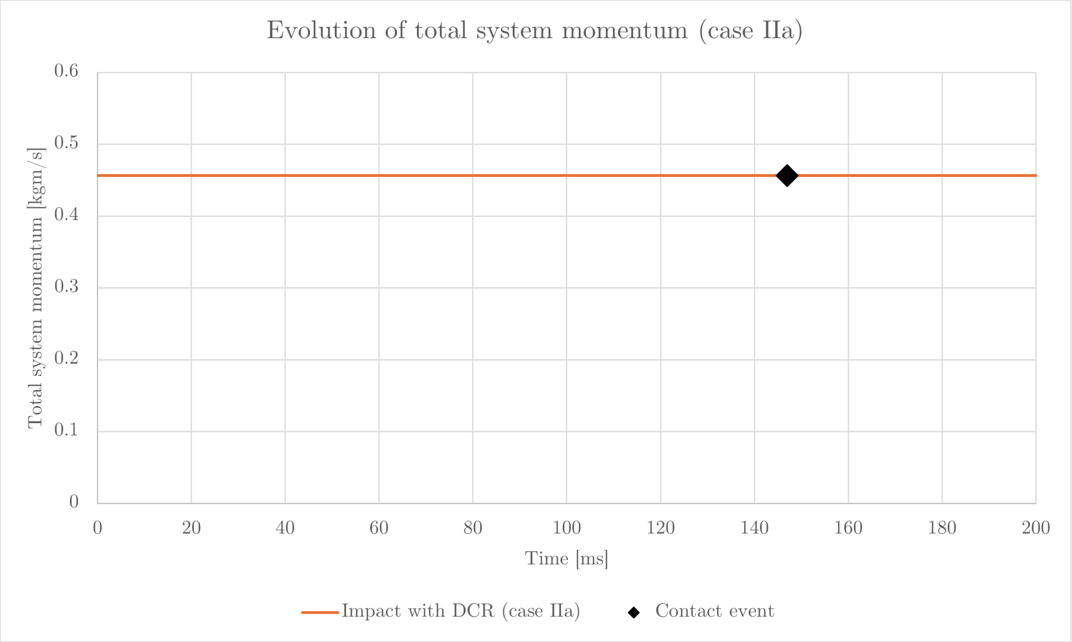

Figure 4.7: Verification case II momentum conservation

As evidenced by the plot in Figure 4.7, the total system momentum remains constant through time in case IIa. This result is to be expected since no dissipative forces are present in the system.

4.3. Penalty approach sensitivity study

As discussed earlier in Subsection 2.3.5, the impetus for developing a DCR-based method for beam-to-beam contact is partly motivated by the shortcomings of LAGRANGE multiplier and penalty methods. LAGRANGE multiplier methods were ruled out due to their expensive computational cost, while penalty methods were identified as problematic due to their dependence on a penalty parameter. Therefore, this section serves as a demonstration of how sensitive the contact formulation can be to the choice of a penalty parameter. Note that while the penalty parameter is analogous to a spring, the convention is to represent it as nondimensional since it is an artificial quantity used to approximate the contact force.

To illustrate the sensitivity of the penalty approach to the choice of penalty parameter ϵ, case II was rerun with the penalty formulation introduced in Subsection 2.3.5, now denoted by case IId. The responses for four different values of ϵ are presented in Figure 4.8 below.

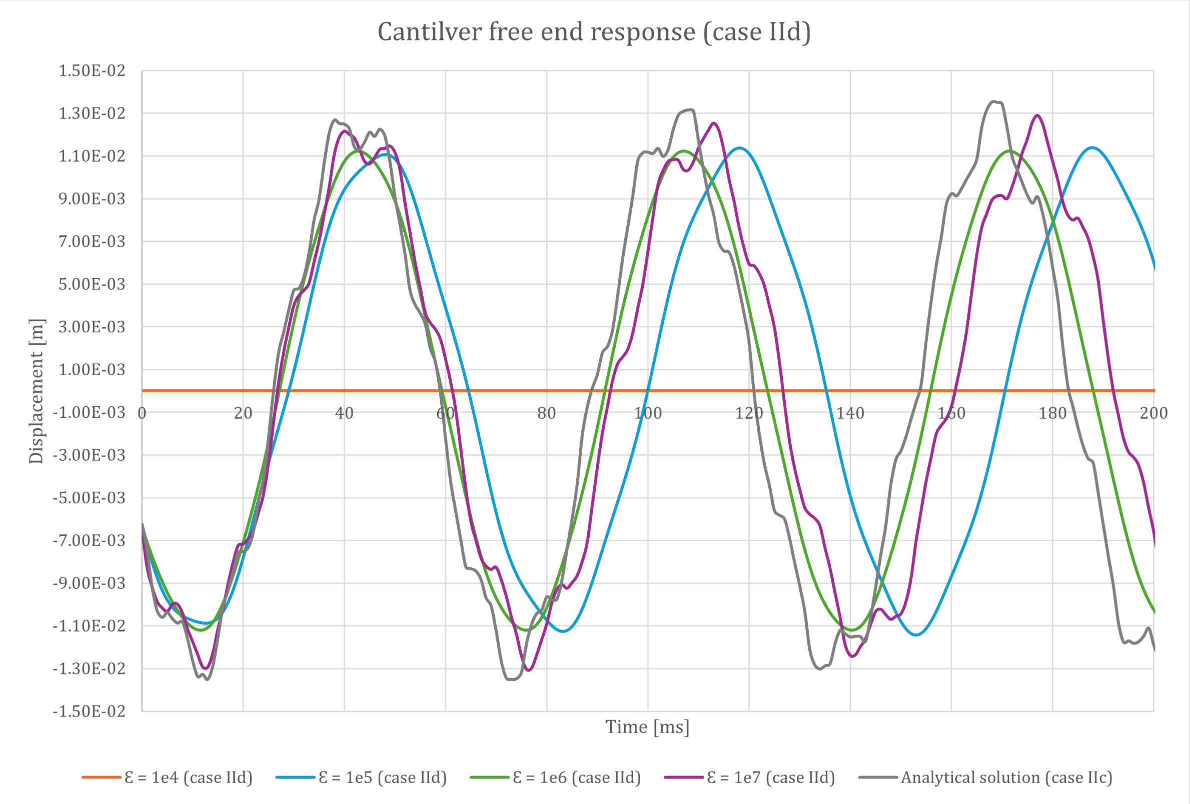

Figure 4.8: Cantilever response to penalty-modelled impact with various values of penalty parameter ϵ (case IId)

As indicated by Figure 4.8, the response is highly dependent on the value of ϵ. For the lowest value, $\epsilon = 1.0e4$, the response is near-zero. The simulation revealed that in this case, the penalty force was not sufficient for enforcing contact and the impactor continued at an unchanged velocity through the cantilever. At $\epsilon = 1.0e5$ and $\epsilon = 1.0e6$, the response amplitudes are the correct order of magnitude, but the higher order modes are not captured. Moreover, a slight phase shift is also present, indicating that the dynamics of the system have not been accurately reproduced. At $\epsilon = 1.0e7$, the response approaches the analytical response, but still exhibits a phase drift over time. The final version of case IId that was tested corresponds to $\epsilon = 1.0e8$. At this high value of ϵ, the system becomes unstable, thus rendering the results meaningless (hence its omission from Figure 4.8). The observed instability suggest that at some value of $\epsilon \in (1.0e7, 1.0e8]$, the penalty stiffness contribution to the system becomes irreconcilable by the chosen time step, necessitating a reduction in the time step size. This highlights the benefit of the DCR formulation, as it does not require tuning of such a parameter ϵ.

The combined results of verification case I and case II provide a solid theoretical foundation for confirming the physical and computational reliability of the novel beam-to-beam DCR method.

5

Results and discussion

To assess the performance of the newly developed DCR method for torsion-free geometrically exact KIRCHHOFF–LOVE beams, three distinct simulation scenarios were analyzed, each aimed at providing new insights into different aspects of this novel technique. The first scenario models the response of a unit insideBCC cell, representing an idealized architected material, when impacted by a projectile. The second scenario examines a more complex situation where two unit insideBCC cells collide, assessing the method's ability to handle simultaneous contact events. The third scenario involves dynamically compressing a 2x2x2 supercell with an insideBCC structure, with the goal of replicating tests from the literature to identify the contact stiffening effect.

5.1. Unit insideBCC impacted by a beam

Third research sub-task (application 1)

Using DCR method to model a simple beam-to-beam impact scenario.

The first set of simulations is that of the unit insideBCC cell being impacted by a beam. A beam is selected as the impactor for convenience, since it can be modelled using the same element type as the struts that comprise the lattice. To study the response of the structure to impact, two scenarios were devised. In the first of these scenarios, the stiffness of the cube is set to be much lower than that of the impactor. Alternatively in the second scenario, the stiffness of the beam projectile is much lower than the cube that it impacts. Apart from the varying stiffness of the two bodies, all other parameters, including the mesh, are unchanged. A visual representation of the simulation setup is provided in Figure 5.1 below.

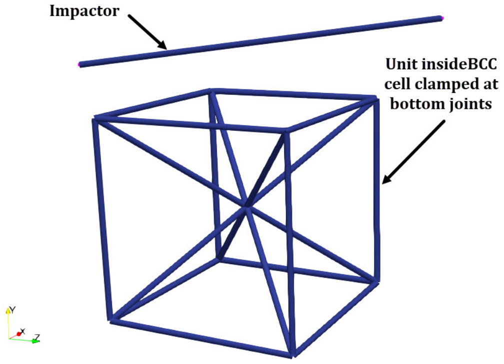

Figure 5.1: Impactor and cube setup

As shown above in Figure 5.1, the impactor is set at an initial height such that it is not in contact with the cube. Its length extends beyond the cube boundaries on both sides in the z-direction and is slightly skewed in the y-direction. This skewing ensures a sequential contact, where the end of the impactor closest to the beam strikes first, thus isolating the contact events. The velocity of the impactor is set to -3 m/s in the y-direction. This initial velocity is applied to all nodes on the impactor.

5.1.1. $E_{cube} < E_{impactor}$

The simulation parameters for this scenario are summarized below in Table 5.1.

Table 5.1: Simulation parameters for cube and beam impact ($E_{cube} < E_{impactor}$)

Parameter	Cube	Impactor
E [MPa]	0.5	10
r [m]	0.001	0.001
ρ [kg/m^3]	1000	1000
Nº elements per strut	5	8
Δt [s]	1.0e-5	
t_{final} [s]	2	

Several frames were extracted from the simulation results and are shown below in Figure 5.2.

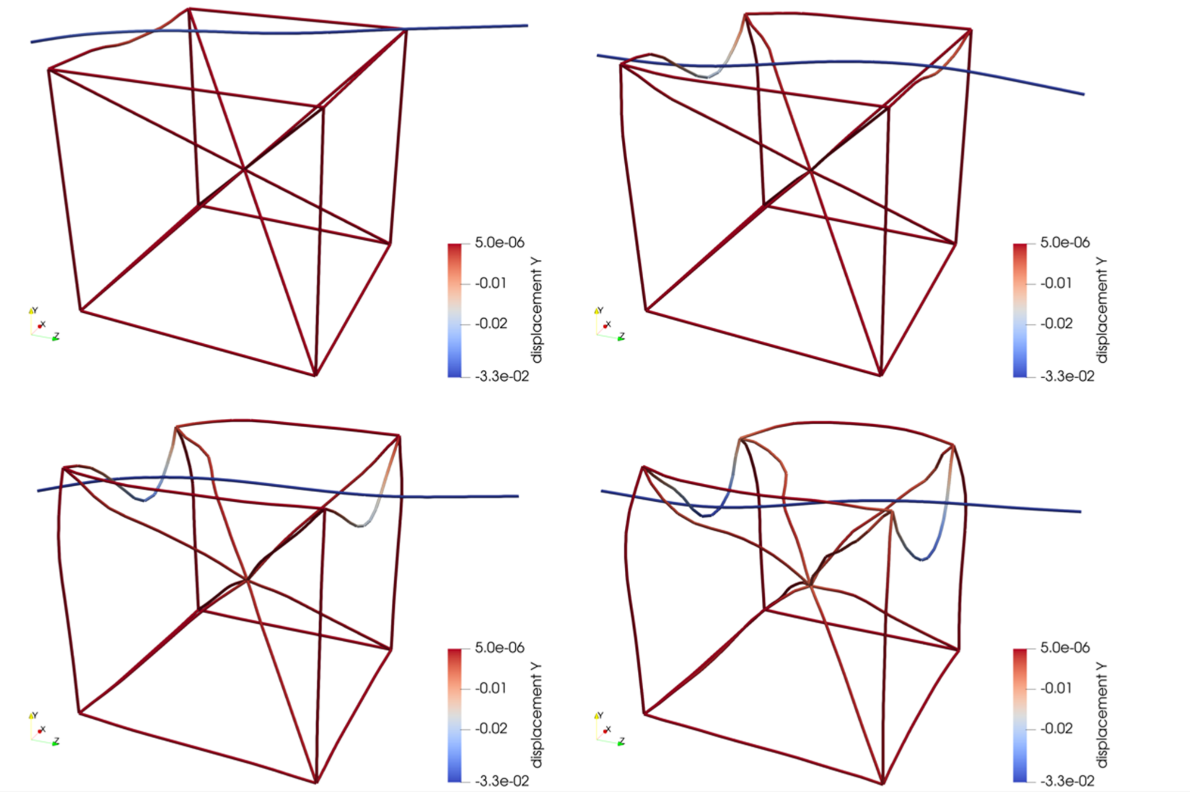

Figure 5.2: Four simulation frames ($E_{cube} < E_{impactor}$)

Figure 5.3 below is taken from the final time step of the simulation.

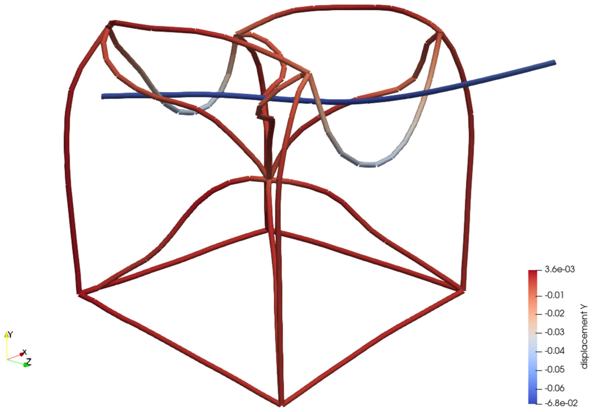

Figure 5.3: Deformed unit insideBCC cell post-impact ($E_{cube} < E_{impactor}$)

From Figure 5.3, it is evident that the cube has undergone partial collapse with many of its struts exhibiting large bending deformations. Inspection of the impactor reveals that the collision has caused it deform, but only slightly compared to the cube. The members that have absorbed the bulk of the impact are clearly the top horizontal struts. As evidenced by Figure 5.2, the contact sequence plays out as expected. The lower part of the impactor hits first, causing immediate deformation in one of the top struts. The impactor still has inertia following the first contact event, so it rotates about the contact point until its opposite end collides with another top strut. Following the second contact event, the impactor changes direction (now having a positive y-velocity), while the struts of the beam continue to deform and absorb the impact energy. The deformed diagonal struts eventually move into the path of the impactor, leading to subsequent smaller impact events until ultimately the simulation is complete.

5.1.2. $E_{impactor} < E_{cube}$

The second beam-cube impact scenario is the inverse of the first, with the stiffness of the impactor now being considerably less than that of the cube. Table 5.2 below enumerates the simulation parameters for this run.

Table 5.2: Simulation parameters for cube and beam impact ($E_{impactor} < E_{cube}$)

Parameter	Cube	Impactor
E [MPa]	10	0.5
r [m]	0.001	0.001
ρ [kg/m^3]	1000	1000
Nº elements per strut	5	8
Δt [s]	1.0e-5	
t_{final} [s]	2	

Figure 5.4 shows several frame extracts from the simulation results. The state of the system at t_{final} is subsequently highlighted in Figure 5.5.

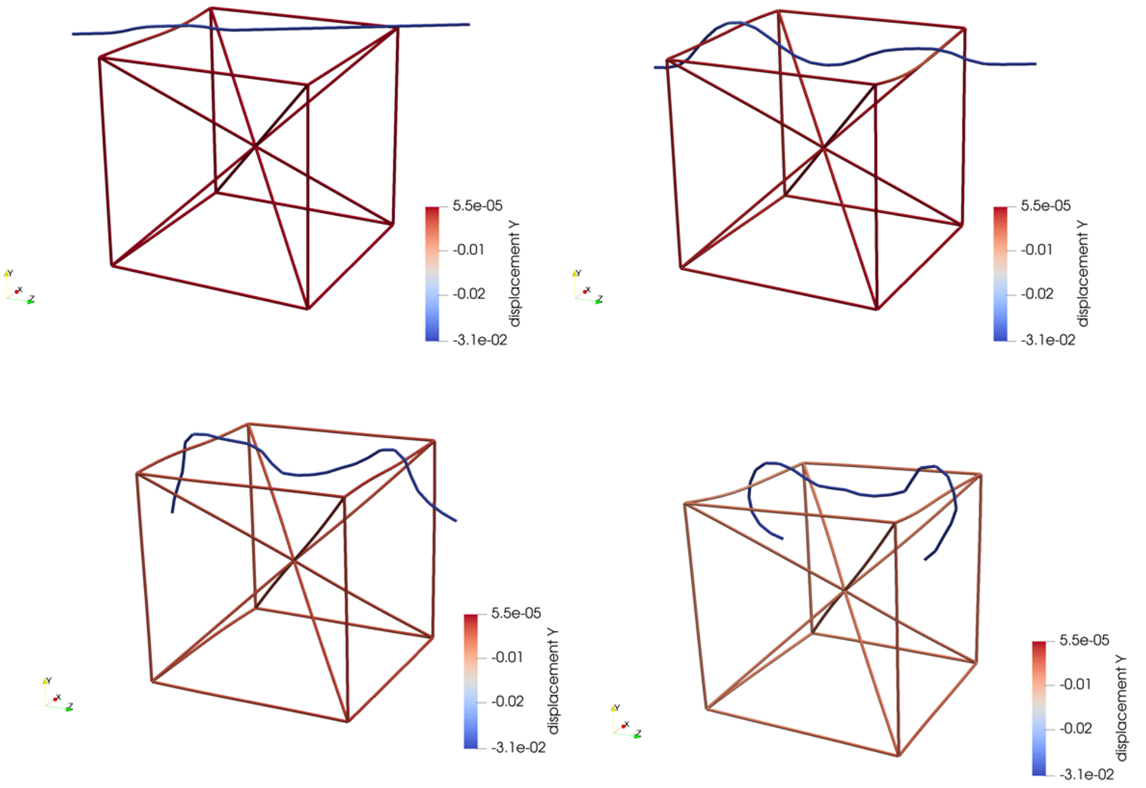

Figure 5.4: Four simulation frames ($E_{impactor} < E_{cube}$)

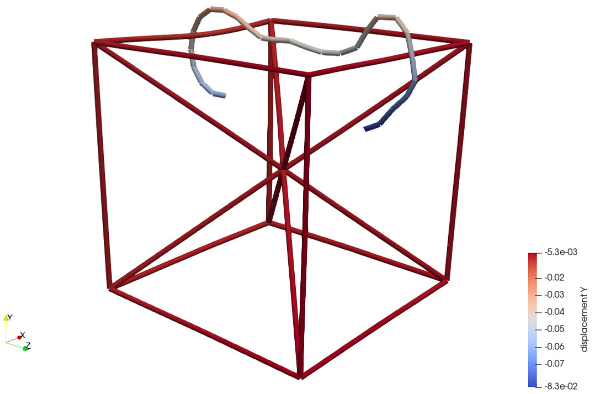

Figure 5.5: Deformed unit insideBCC cell post-impact ($E_{impactor} < E_{cube}$)

In contrast to the first scenario (depicted in Figure 5.3), the impacted cube deforms very little while the impactor undergoes large deformations. The post-processed simulation results reveal that, after initial contact with the cube's upper struts, the impactor beam locally reverses direction near the impact points. Meanwhile, the inertia of the moving beam causes the overextended segments to continue in their original trajectory, eventually leading them to curl around the top struts.

These two simple simulations show that the DCR method is capable of modelling impact applications for structures comprised of thin beams. As a final remark, it should be noted that both scenarios were shown to conserve the total system momentum at each time step.

5.2. Collision of two insideBCC unit cells

Third research sub-task (application 2)

Using the DCR method to model simultaneous beam-to-beam impact events.

In this section, a more complex collision scenario is analyzed. One unit insideBCC cell is fixed at its lower four joints, a while rotated copy of the cell is propelled at -3.0 m/s in the y-direction towards the stationary cell. The impact scenario is examined twice: first with a compliant material and then with a stiffer material. A visual representation of the setup is provided below in Figure 5.6.

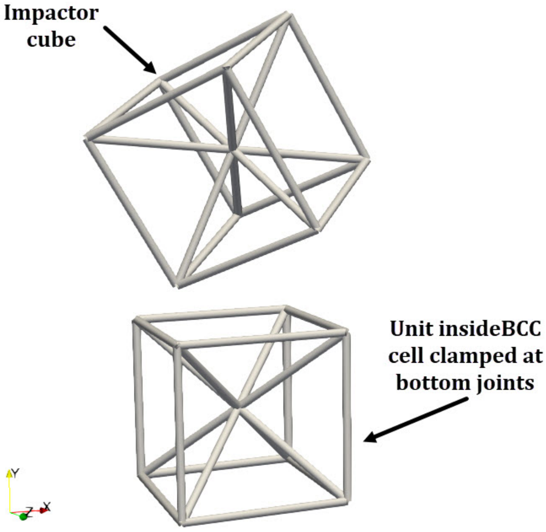

Figure 5.6: Simulation setup for the collision between two unit insideBCC cells

5.2.1. Compliant cubes

To begin, consider the scenario with the following simulation parameters

Table 5.3: Simulation parameters for impact between two unit insideBCC cells (E = 0.5 MPa)

Parameter	Impacted	Impactor
E [MPa]	0.5	0.5
r [m]	0.001	0.001
ρ [kg/m^3]	1000	1000
Nº elements per strut	5	5
Δt [s]	1.0e-7	
t_{final} [s]	2	

The evolution of the system is summarized visually via four still frames extracted from the results in Figure 5.7, followed by Figure 5.8, depicting the final state of the system.

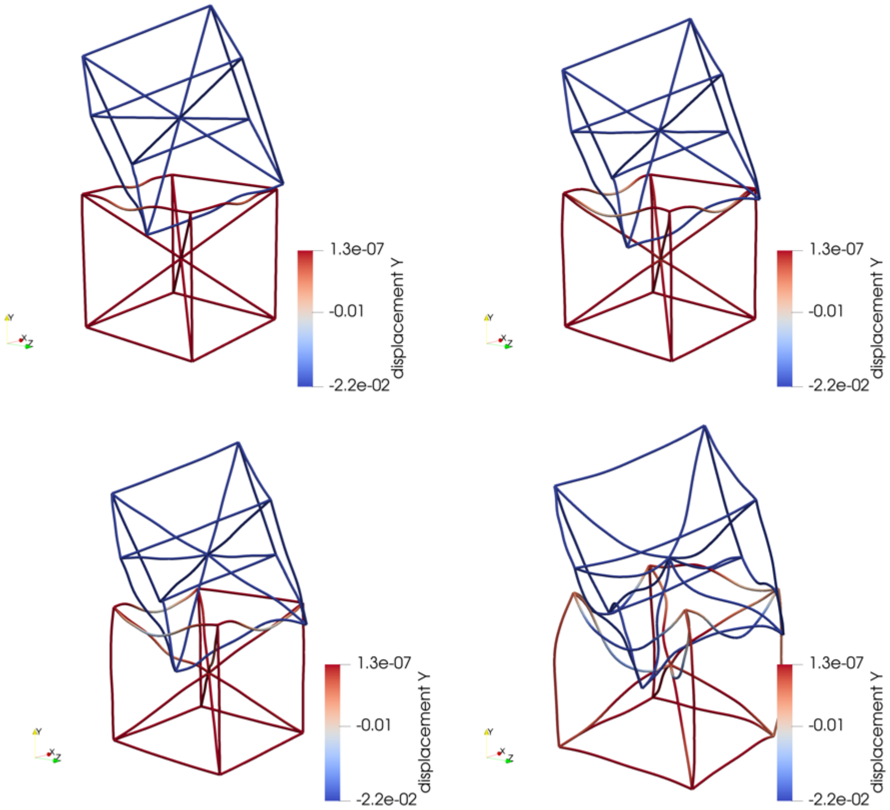

Figure 5.7: Four simulation frames (E = 0.5 MPa)

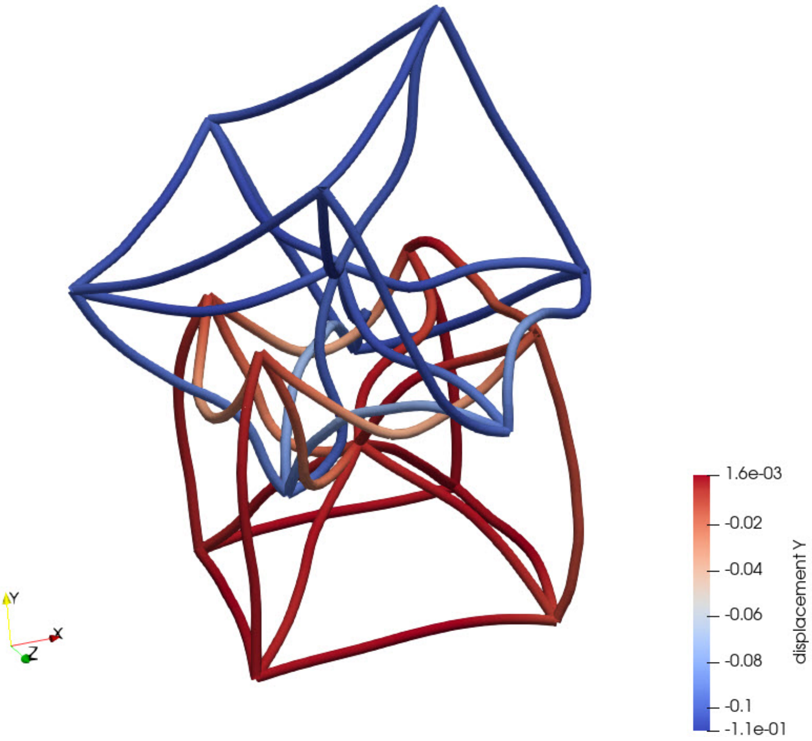

Figure 5.8: Deformed unit insideBCC cells post-impact (E = 0.5 MPa)

As shown in Figure 5.8, both cubes exhibit massive deformation due to impact. A complex web of contacting beams is produced as the impacting cell is stopped by the stationary cell. One crucial shortcoming of a former assumption becomes evident from this simulation. Since beam elements which have a node coinciding with a joint were excluded from participating in contact, one contact event is missed. To show this, a screenshot was taken at several time steps following the missed contact event. The missed contact event is highlighted in Figure 5.9 below.

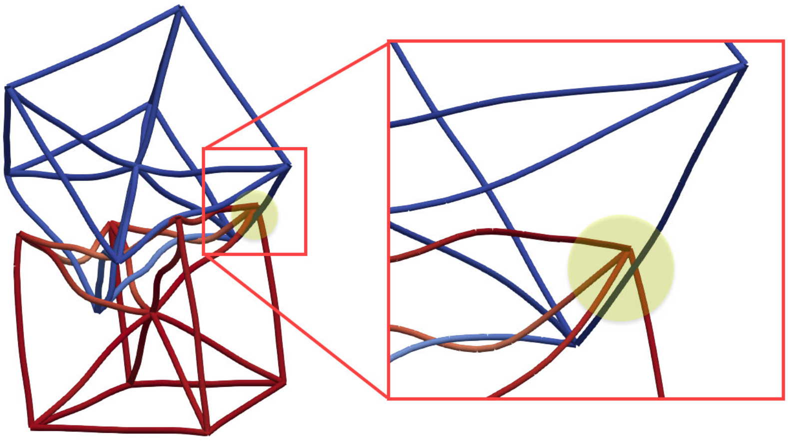

Figure 5.9: Missed contact at joint

The missed contact event occurred because a beam on the stationary cell (red) was detected as being in contact with the edge of the impactor cell (blue). However, since the detected beam on the stationary cell has a joint at one end, the contact algorithm skipped it, allowing the impactor beam to pass through the stationary beam. There are two possible approaches to address this type of missed contact. First, the contact algorithm can be adjusted to ignore interactions between elements with joint nodes only if both elements belong to the same structure. Alternatively, using a finer or biased mesh can reduce the size of the elements adjacent to the joint, thereby decreasing the likelihood of their involvement in contact events.

5.2.2. Stiffer cubes

Proceeding now with the same impact scenario with a stiffer material, consider the following simulation parameters:

Table 5.4: Simulation parameters for impact between two stiffer unit insideBCC cells (E = 10 MPa)

Parameter	Impacted	Impactor
E [MPa]	10	10
r [m]	0.001	0.001
ρ [kg/m^3]	1000	1000
N$^{\underline{o}}$ elements per strut	5	5
Δt [s]	1.0e-7	
t_{final} [s]	2	

The final state of the modified system is show in Figure 5.11 below.

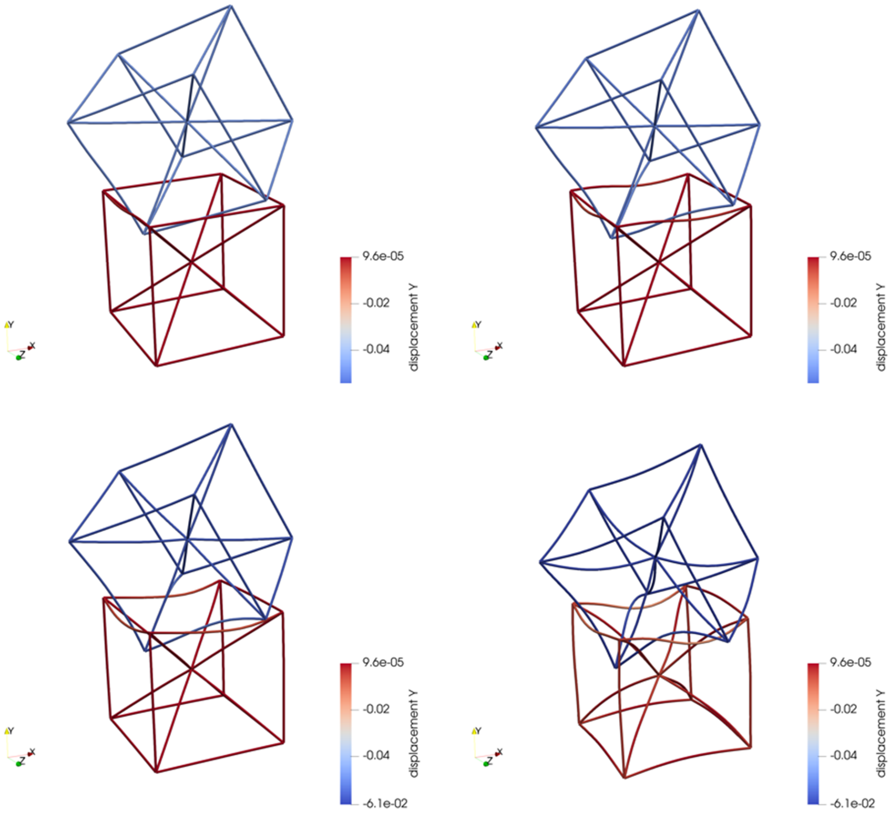

Figure 5.10: Four simulation frames ($E = 10$ MPa)

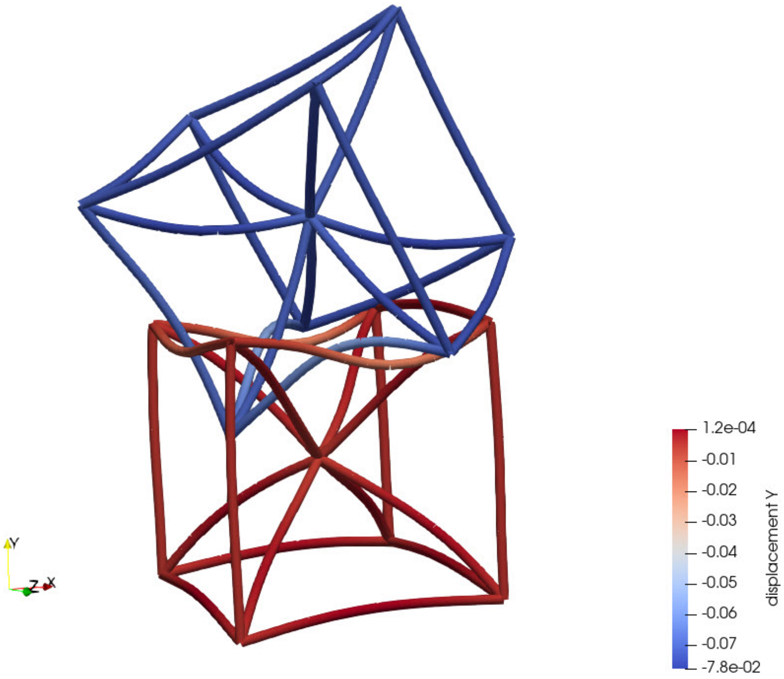

Figure 5.11: Deformed unit insideBCC cells post-impact ($E = 10$ MPa)

Figure 5.11 exhibits similar response characteristics as the more compliant version shown in Figure 5.8, including the missed contact in the vicinity of one of the upper joints. As expected, impact between two stiffer cells results in smaller deformations.

Finally, both simulations uphold the principle of momentum conservation and successfully model simultaneous contact. However, they also reveal a limitation in capturing contact near joints.

5.3. Compression of a 2x2x2 insideBCC lattice

Third research sub-task (application 3)

Using the DCR method to capture the contact stiffening effect in a compressed lattice structure.

The third and final application of the novel beam-to-beam contact algorithm tests its ability to model a well-documented phenomenon. As discussed in Subsection 2.1.2 and supported by various studies, a compressed lattice exhibits a final phase where structural collapse results in a stiffening effect. This effect is characterized by an increase in compressive load relative to compressive displacement, attributed to contact between struts in the collapsed lattice. The aim of these simulations is to demonstrate that a DCR-enabled simulation can accurately capture this stiffening effect. To achieve this, a lattice composed of insideBCC cells was assembled into a 2x2x2 supercell.

Characterizing the stiffening effect requires first establishing a baseline case, which involves running a compressive simulation on the supercell without capturing contact. In this baseline scenario, beams are allowed to intersect each other in a non-physical manner. Both the baseline and contact cases were run using the same setup, which is summarized in Table 5.5 below.

Table 5.5: Simulation parameters for a compressed lattice comprised of 2x2x2 insideBCC cells

Parameter	Value
E [MPa]	0.5
r [m]	0.001
ρ [kg/m^3]	1000
Nº elements per strut	4
Δt [s]	1.0e-5
t_{final} [s]	5

The compression simulation setup is depicted schematically in Figure 5.12 below.

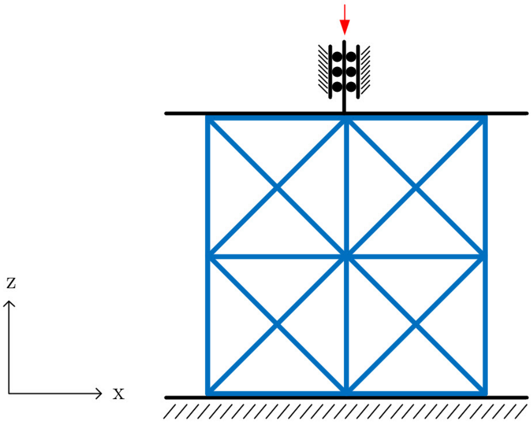

Figure 5.12: Setup for simulation of a compressed 2x2x2 insideBCC supercell

The deformed supercell at t_{final} is presented in Figure 5.13 below.

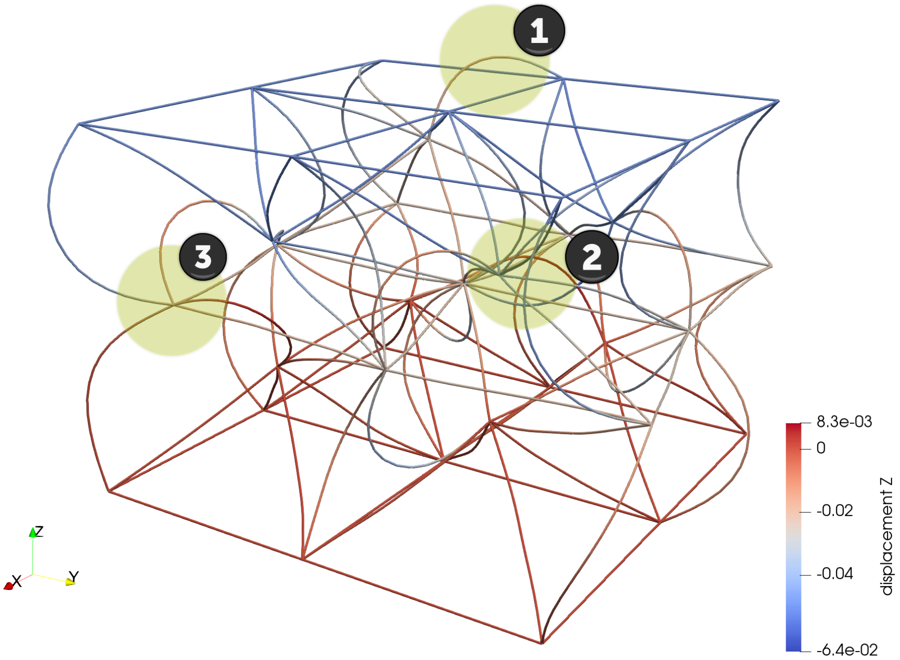

Figure 5.13: 2x2x2 insideBCC supercell compressed to 75% original height (without contact)

Several interesting features can be observed from the compressed state of the supercell depicted in Figure 5.13. To facilitate the discussion of these features, the numbered labels in Figure 5.13 will be used as reference keys.

Starting with the highlighted features corresponding to feature **1**, it is evident that certain struts have buckled unrealistically, as supports at the top and bottom would prevent such deformations. Because boundary conditions were applied to nodes, this simulation does not capture the interaction with the stationary bottom surface or the top compressive surface that would be present in real-life tests.

Feature **2** illustrates the consequence of omitting contact from the simulation. In this instance, several beams are intersecting in a physically impossible manner. This is just one example, but throughout the simulation, numerous such intersections occur.

In the final callout of Figure 5.13, feature **3** illustrates a direct consequence of the pin joint assumption. The buckling shape of the corner vertical beams would never be possible in a real-life structure, as a joint with non-zero stiffness would maintain some degree of local continuity in the beam tangents across the joint.

Having reviewed the limitations of the contact-free baseline case, the contact case can now be considered. The same compression scenario simulation was reproduced with the beam-to-beam DCR feature enabled. Still frames showing the gradual compression in four steps is presented in Figure 5.14 below.

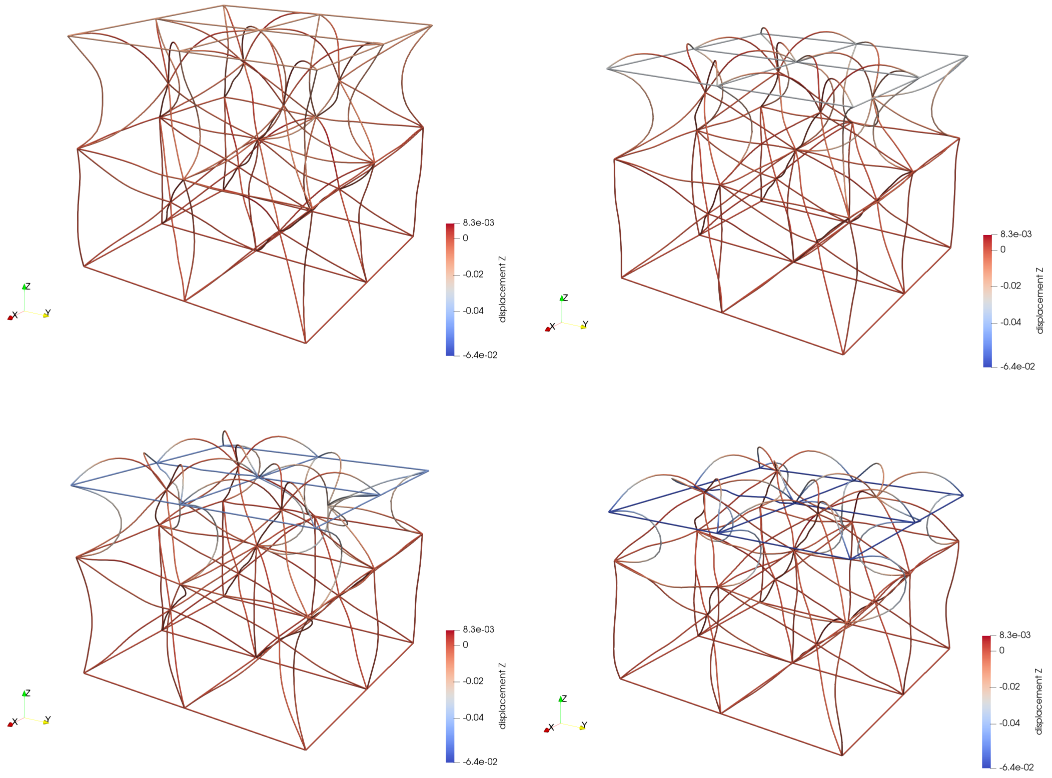

Figure 5.14: 2x2x2 insideBCC supercell at 8% (top left), 16% (top right), 24% (bottom left), and 32% (bottom right) compression in the axial *z*-direction

The final state of the system at 32% compression is highlighted with an enhanced view in Figure 5.15 below.

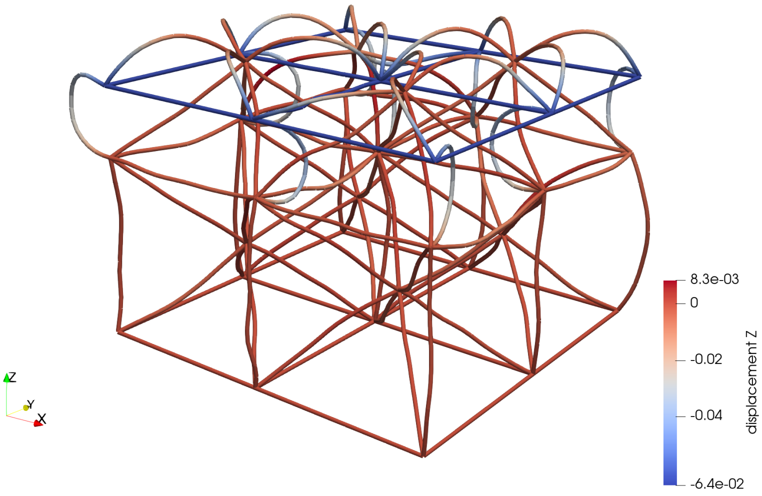

Figure 5.15: 2x2x2 insideBCC supercell at 68% original height (with contact)

Note that the randomly perturbed mesh was not modified between the run without contact and the one with contact to ensure that any differences can wholly be attributed to contact between beams. To emphasize the difference between the contact and non-contact versions, both sets of results were superimposed. The convention used in the figures below is blue for non-contact and orange for contact.

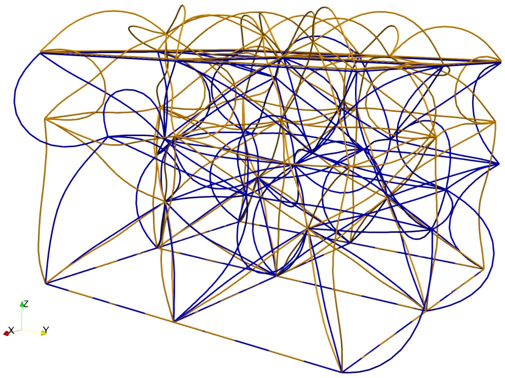

Figure 5.16: Iso view of the superimposed compression runs in their final state

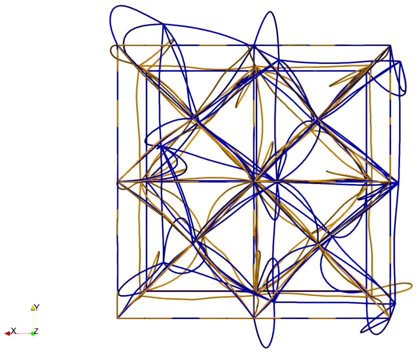

Figure 5.17: Top view of the superimposed compression runs in their final state

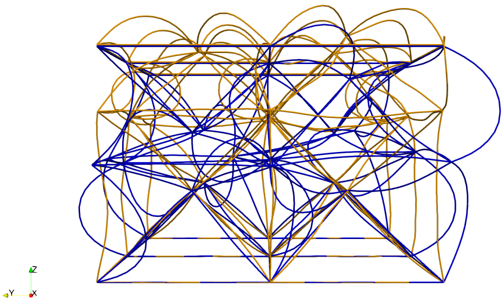

Figure 5.18: Front view of the superimposed compression runs in their final state

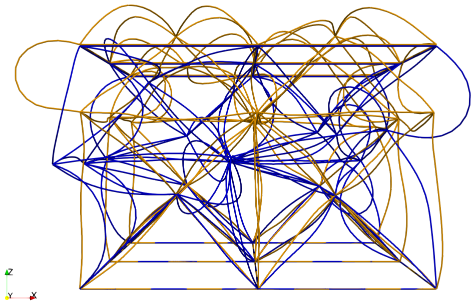

Figure 5.19: Side view of the superimposed compression runs in their final state

As a final means of assessing the contact results, the original load-displacement curve of the non-contact case was superimposed with the load-displacement curve of the contact case. The resulting response comparison is shown below in Figure 5.20.

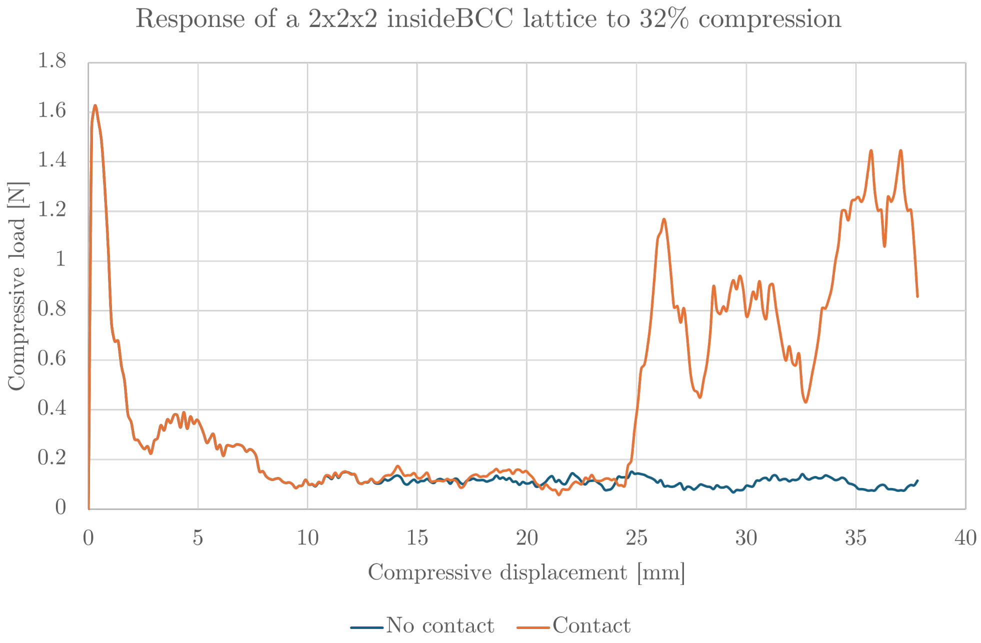

Figure 5.20: Load-displacement curve for a 2x2x2 insideBCC supercell compressed at 10 mm/s (with and without contact)

Figure 5.20 above shows a consistent response with the non-contact scenario, wherein both curves reveal a characteristic buckling response, with a sharp increase until the critical buckling load is reached, followed by a levelling out of the load curve. The curves match identically until approximately 11 mm of compression, where the orange curve diverges. This point marks the first contact event in the contact-integrated case. From this point until approximately 24 mm of compression, the two responses behave nearly the same. Once compression has reach this mark of approximately 12% compression, there is a large increase in the compressive load response. This is the true onset of the contact stiffening effect. Beyond this point, the bulk-level response of the architected material resembles that of the compression tests shown in the literature. The most notable discrepancy, however, is the presence of local dips in the compressive response curve in the stiffening regime (region of the orange curve beyond 24 mm in Figure 5.20). It is believed that these phenomena are a consequence of the pin joint assumption. The intermittent instabilities caused by the use of pin joints may be causing the structure to locally collapse

With the results presented in Figure 5.20, the third and most important research objective has been partially met. The *onset* of the contact stiffening effect has been captured using a novel DCR beam-to-beam contact model. It is only partially met, because the magnitude of the stiffening does not match what is reported in the literature. This is to be expected, however, since the simulation only compressed the structure by 32%, whereas the responses from the literature show the load-displacement until complete failure of the structure, which typically occurs beyond the 50% compression mark. It is thus hypothesized that if the same simulation shown in Figure 5.20 were allowed to continue to larger compressions, the contact stiffening effect would be more pronounced.

The lattice was not compressed by more than 25% due to time constraints. Obtaining an accurate model in this high compression displacement regime requires more elements per beam to ensure that no contact events are missed and a smaller time step to ensure solver stability. The version presented in this section took 72 hours to run on a gaming laptop. The same simulation was run on the research group's computational server, but because it was executed in a serial manner, it could only use a single processor. As a result, there was no performance improvement compared to running it on the gaming laptop. Given the additional requirements for a larger compression test, it would likely take over a week to complete on the same machine. For this reason, longer compression tests have been deferred to future iterations of application 3.

6
Conclusion

6.1. Summary of findings

Recalling the previously stated sub-tasks of the research objective, this thesis aimed to **1** derive a suitable DCR-based beam-to-beam contact formulation, **2** verify said formulation with benchmark problems, and **3** apply the novel formulation to a compressed architected material sample in order to observe the contact stiffening effect.

The DCR formulation for beam-to-beam contact was fully derived and is presented in Chapter 3. Verification case I (Section 4.1) and case II (Section 4.2) revealed that the novel contact formulation was successful at capturing a simple contact event between two slender beams.

The first two applications presented in Chapter 5 mark the first ever use of DCR for modelling physics involving beam-lattice structures. These applications, a beam-lattice collision and a lattice-lattice collision, demonstrated the preservation of total system momentum and accurately modelled the large deformation of the involved struts. Despite the limitations posed by the idealized pin joints used in these scenarios, the results are promising indicators of the success of the proposed new method.

The third application was successful in capturing the onset of the contact stiffening effect. The stiffening effect for compression values exceeding 32% was not reported due to time constraints. While early-stage stiffening due to contact is clearly shown in the results, the response for high values of compression has yet to be documented. Thus, the main objective is only partially satisfied.

6.2. Recommendations for future work

In addition to the insights gained from this thesis, several key areas have been identified for potential improvement in future developments of this topic.

6.2.1. Energy check

Although the verification cases strongly imply that energy is conserved during contact events, explicit demonstration is still pending. To validate the small time step assumption for modelling contact between slender beams, a thorough analysis of the total system energy over time is necessary. This entails extracting and plotting the kinetic and internal strain energies throughout a contact simulation. By doing so, it can be conclusively proven that the method conserves energy. This is hence the first step that must be taken before exploring the subsequent recommendations outlined in the section.

6.2.2. Alternative intersection removal approach

An alternative intersection removal approach within the context of DCR for beam elements was proposed in Section 3.4. It was highlighted that a potentially more realistic method of removing intersections is possible through polynomial fitting. A procedure for this method was outlined, although its implementation is yet to be tested at scale. Therefore, it is recommended that further investigation be conducted into the rigor and feasibility of this method, particularly regarding the numerical implementation of the SVD step in solving the least-squares problem. Once verified, this method can be integrated within the DCR framework to replace the rigid translation method of removing intersections.

6.2.3. Plasticity

At the start of this thesis, the summit formulation for beam elements did not include the ability to capture plasticity. This limitation motivated the choice of a hyperelastic constitutive law to model large deformations, a key feature for analyzing collapsed truss-lattice structures. However, the issue of plasticity now represents an ongoing area of research within Dr. Giovanardi's team. To model realistic architected materials for impact absorption applications in aerospace, the ability to represent stiffer materials is crucial. Therefore, it is recommended to continue the work towards developing a plasticity-integrated FEM formulation.

6.2.4. Lattice joints

As previously discussed in Subsection 3.2.6, this study employed idealized pin joints in the assembly of lattices. It was also highlighted in Chapter 2 that tuning the stiffness of joints is crucial for an accurate FEM implementation. The recommendation is thus to first incorporate rigid joints and then derive a systematic method for characterizing the local stiffness in the region surrounding a joint for numerical implementations, ensuring it matches benchmark physical tests.

6.2.5. Friction

Since this study was partially intended to establish a proof-of-concept for the novel beam-to-beam DCR formulation, a decision was made to consider the frictionless contact case. However, the original definition of the DCR method as provided by Cirak and West does include a frictional contact variant of the method [1]. As such, a recommendation for future iterations is to incorporate the effect of friction in the contact algorithm.

6.2.6. Fracture

An important feature of physical compression tests on lattices reported in the literature (see Subsection 2.1.2) is the onset of fracture in fully compressed samples. After the contact-enabled stiffening phase of compression, the lattice eventually fails at the material level. The ability to model fracture is not possible with the current element formulation. However, recent additions to summit include a method to model fracture in slender beams using the discontinuous GALERKIN/cohesive zone method [60].

6.2.7. Parallel implementation

Another key ability that is partially unlocked via the use of the discontinous GALERKIN method is the potential for parallel implementation, thereby distributing computation across multiple processors. It has already been shown by Radovitzky *et al.* that fracture in solids via the GALERKIN/cohesive zone method is conducive to parallelization and has exhibited accurate results in modelling ballistic impact [61].

The main obstacle in implementing the DCR method in parallel is the contact detection algorithm, which is non-trivial in a parallel setting. A study by Cirak *et al.* addresses this limitation by proposing a parallel framework for contact using solid elements. The authors propose a framework in which the contact surface mesh is stored on all computational nodes and a recursive coordinate bisection (RCB) algorithm is used to distribute surface elements evenly. A serial closest point algorithm identifies potential collisions on each node. The orthogonal range query algorithm, utilizing a sparse bucket data structure and binary search, reduces storage needs while maintaining performance [62]. These strategies enhance the efficiency and scalability of contact detection in large-scale parallel computations.

In the one-dimensional beam case, there is no distinction between the surface mesh elements, as all elements could potentially participate in contact. However, in the context of summit, significant changes to the current data structure handling would be necessary to incorporate such a parallel implementation. Despite these challenges, the benefits of distributing computation across parallel nodes would be immense. It is recommended that further research be conducted to determine whether this parallel implementation could be applied to the beam-to-beam DCR case in future iterations.

6.2.8. Implementation of a line-to-line DCR variant

The proposed DCR method utilizes a point-to-point formulation, enforcing the bilateral orthogonality condition between contacting element pairs. As reviewed in Subsection 2.3.8, this approach can lead to numerical issues in finding unique solutions in some edge cases. An alternative approach, called line-to-line, uses a unilateral orthogonality condition to approximate a distributed penalty load rather than a point force, also capturing the contact contribution as a penalty potential. This unilateral constraint ensures the existence of a solution for small contact angles, but introduces additional complexities in numerical integration. It is thus recommended that further investigation be conducted into harmonizing the penalty-free DCR with line-to-line mortar methods.

6.2.9. Different lattice structures

Given the limited scope of this thesis, only a single lattice structure was studied. The choice of the insideBCC configuration was motivated in Subsection 2.1.1. However, there are countless other interesting configurations, each possessing unique structural characteristics. Among the more interesting configurations are the FCC and HCP, which, like the BCC, stem from crystallographic microstructures (see Figure 6.1). Additionally, it would be fascinating to study more unconventional configurations, such as auxetic, phononic, or even aperiodic lattices, within a contact-integrated framework. The recommendation is to expand the space of architected materials by automating mesh generation based on a single unit cell configuration, thereby unlocking the potential to model a plethora of diverse architected materials.

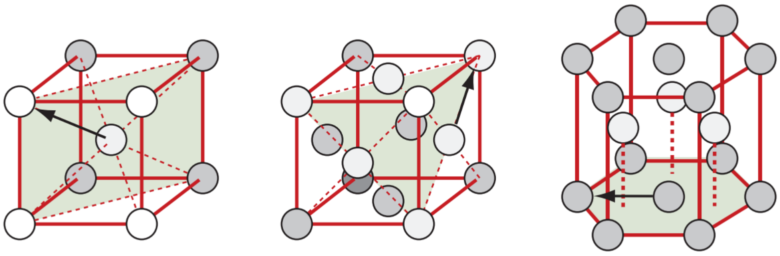

Figure 6.1: Configurations of the BCC (left), FCC (middle), and HCP unit cells [63]

6.3. Final remarks

In closing, this thesis has successfully derived, verified, and applied a novel DCR-based beam-to-beam contact formulation for geometrically exact slender beams, demonstrating a promising advancement in modelling the response of truss-based architected materials to impact. The method was successful in capturing the onset of the contact-induced stiffening effect in a compressed insideBCC lattice. Despite the limitations posed by idealized pin joints, frictionless contact, and compliant media assumptions, the findings underscore the potential of the proposed method. Recommendations for future work include parallelization, incorporating plasticity, the use of rigid joints, including friction, fracture modelling, as well as exploring alternative intersection removal approaches. Expanding the study to different lattice structures will further enhance the understanding and application of architected materials for modelling HVI shields.

References

[1] F. Cirak and M. West. "Decomposition contact response (DCR) for explicit finite element dynamics". *International Journal for Numerical Methods in Engineering* 64 (2005), pp. 1078–1110. DOI: `10.1002/nme.1400`.

[2] W. G. Colvin T.J. Karcz J. "Cost and Benefit Analysis of Orbital Debris Remediation". *Nasa report* (Mar. 2023).

[3] S. Ryan, T. Hedman, and E. L. Christiansen. "Honeycomb vs. foam: Evaluating potential upgrades to ISS module shielding". *Acta Astronautica* 67 (7-8 Oct. 2010). DOI: `10.1016/j.actaastro.2010.05.021`.

[4] R. Voillat, F. Gallien, A. Mortensen, and V. Gass. "Hypervelocity impact testing on stochastic and structured open porosity cast Al-Si cellular structures for space applications". *International Journal of Impact Engineering* 120 (Oct. 2018). DOI: `10.1016/j.ijimpeng.2018.05.002`.

[5] X. Zhang, R. Wang, J. Liu, X. Li, and G. Jia. "A numerical method for the ballistic performance prediction of the sandwiched open cell aluminum foam under hypervelocity impact". *Aerospace Science and Technology* 75 (Apr. 2018). DOI: `10.1016/j.ast.2017.12.034`.

[6] M. Jamshidian, N. Boddeti, D. W. Rosen, and O. Weeger. "Multiscale modelling of soft lattice metamaterials: Micromechanical nonlinear buckling analysis, experimental verification, and macroscale constitutive behaviour". 188 (Dec. 2020). DOI: `10.1016/j.ijmecsci.2020.105956`.

[7] G. Labeas and E. Ptochos. "Homogenization of selective laser melting cellular material for impact performance simulation". 6 (4 Aug. 2015), pp. 439–450. DOI: `10.1108/IJSI-10-2014-0059`.

[8] R. Gümrük and R. A. Mines. "Compressive behaviour of stainless steel micro-lattice structures". 68 (Mar. 2013), pp. 125–139. DOI: `10.1016/j.ijmecsci.2013.01.006`.

[9] M. Pham, C. Liu, I. Todd, and J. Lertthanasarn. "Damage-tolerant architected materials inspired by crystal microstructure". *Nature* 565 (7739 Jan. 2019), pp. 305–311. DOI: `10.1038/s41586-018-0850-3`.

[10] T. A. Alwattar and A. Mian. "Developing an equivalent solid material model for bcc lattice cell structures involving vertical and horizontal struts". 4 (2 2020). DOI: `10.3390/jcs4020074`.

[11] A. G. Evans, M. Y. He, V. S. Deshpande, J. W. Hutchinson, A. J. Jacobsen, and W. B. Carter. "Concepts for enhanced energy absorption using hollow micro-lattices". *International Journal of Impact Engineering* 37 (9 Sept. 2010), pp. 947–959. DOI: `10.1016/j.ijimpeng.2010.03.007`.

[12] C. Meier, A. Popp, and W. Wall. "A finite element approach for the line-to-line contact interaction of thin beams with arbitrary orientation". 308 (2016), pp. 377–413. DOI: `https://doi.org/10.1016/j.cma.2016.05.012`.

[13] T. A. Schaedler and W. B. Carter. "Architected Cellular Materials". *Annual Review of Materials Research* 46 (July 2016), pp. 187–210. DOI: `10.1146/annurev-matsci-070115-031624`.

[14] D. Nepal, S. Kang, K. M. Adstedt, K. Kanhaiya, M. R. Bockstaller, L. C. Brinson, M. J. Buehler, P. V. Coveney, K. Dayal, J. A. El-Awady, L. C. Henderson, D. L. Kaplan, S. Keten, N. A. Kotov, G. C. Schatz, S. Vignolini, F. Vollrath, Y. Wang, B. I. Yakobson, V. V. Tsukruk, and H. Heinz. "Hierarchically structured bioinspired nanocomposites". *Nature Materials* 22 (1 Jan. 2023), pp. 18–35. DOI: `10.1038/s41563-022-01384-1`.

[15] R. Mines. *Metallic Microlattice Structures: Manufacture, Materials and Application*. Cham, Switzerland: Springer, 2019.

[16] S. Watts. "Elastic response of hollow truss lattice micro-architectures". *International Journal of Solids and Structures* 206 (Dec. 2020), pp. 472–564. DOI: `10.1016/j.ijsolstr.2020.08.018`.

[17] T. A. Schaedler, C. J. Ro, A. E. Sorensen, Z. Eckel, S. S. Yang, W. B. Carter, and A. J. Jacobsen. "Designing metallic microlattices for energy absorber applications". *Advanced Engineering Materials* 16 (3 2014), pp. 276–283. DOI: `10.1002/adem.201300206`.

[18] W. Borchardt-Ott. *Crystallography*. Springer Berlin Heidelberg, 1993. DOI: `10.1007/978-3-662-00608-5`.

[19] M. H. Luxner, J. Stampfl, and H. E. Pettermann. "Finite element modeling concepts and linear analyses of 3D regular open cell structures". 40 (22 Nov. 2005), pp. 5859–5866. DOI: `10.1007/s10853-005-5020-y`.

[20] C. Meier, A. Popp, and W. Wall. "Geometrically exact finite element formulations for slender beams: Kirchhoff-Love theory versus Simo-Reissner theory". *Archives of Computational Methods in Engineering* 26 (2019), pp. 163–243. DOI: `10.1007/s11831-017-9232-5`.

[21] J. Heyman. *Structural Analysis: A Historical Approach*. Cambridge University Press, 1998.

[22] A. Öchsner. *Classical Beam Theories of Structural Mechanics*. Springer International Publishing, Jan. 2021, pp. 1–186. DOI: `10.1007/978-3-030-76035-9`.

[23] G. Kirchhoff. "Ueber das Gleichgewicht und die Bewegung eines unendlich dünnen elastischen Stabes." ger. *Journal für die reine und angewandte Mathematik* 56 (1859), pp. 285–313.

[24] A. E. H. Love. *A treatise on the mathematical theory of elasticity*. Fourth. Cambridge University Press, 1927.

[25] iuser Verlag Basel and B. E. Reissner. "On One-Dimensional Finite-Strain Beam Theory". *Journal of Applied Mathematics and Physics (ZAMP)* 23 (1972).

[26] E. Reissner. "Reflections on the theory of elastic plates". *Applied Mechanics Review* 38.11 (1985), pp. 1453–1464. DOI: `10.1115/1.3143699`.

[27] J. Simo. “A finite strain beam formulation. The three-dimensional dynamic problem. Part I”. 49.1 (1985), pp. 55–70. DOI: `https:/s/doi.org/10.1016/0045-7825(85)90050-7`.

[28] M. A. Crisfield and G. Jelenic. “Objectivity of strain measures in the geometrically exact three-dimensional beam theory and its finite-element implementation”. *Proceedings of the Royal Society A: Mathematical, Physical and Engineering Sciences* 455 (1983 1999), pp. 1125–1147. DOI: `10.1098/rspa.1999.0352`.

[29] J. C. Simo and L. Vu-Quoc. *A three-dimensional finite-strain rod model. Part II: Computational aspects*. 1986.

[30] B. C. Hall. *Lie Groups, Lie Algebras, and Representations*. Second. Springer, 2015.

[31] C. Meier, A. Popp, and W. A. Wall. “A locking-free finite element formulation and reduced models for geometrically exact Kirchhoff rods”. *Computer Methods in Applied Mechanics and Engineering* 290 (2015), pp. 314–341. DOI: `https://doi.org/10.1016/j.cma.2015.02.029`.

[32] M. Schulz and M. Böl. “A finite element formulation for a geometrically exact Kirchhoff–Love beam based on constrained translation”. *Computational Mechanics* 64 (4 Oct. 2019), pp. 1155–1175. DOI: `10.1007/s00466-019-01698-z`.

[33] P. Wriggers. *Computational Contact Mechanics*. Berlin: Springer, 2006.

[34] A. Signorini. *Sopra alcune questioni di statica dei sistemi continui*. 1933.

[35] A. Signorini. “Questioni di elasticita’ non linearizzata (signorini)”. 1960.

[36] N.J. Carpenter, R.L. Taylor, and M.G. Katona. “Lagrange constraints for transient finite-element surface-contact”. *International Journal for Numerical Methods in Engineering* 32 (1991), pp. 103–128.

[37] J. E. Marsden and A. Tromba. *Vector calculus*. W.H. Freeman, 2012, p. 545.

[38] R. C. Fetecau, J. E. Marsden, M. Ortiz, and M. West. “Nonsmooth lagrangian mechanics and variational collision integrators”. *SIAM Journal on Applied Dynamical Systems* 2 (3 Aug. 2003). DOI: `10.1137`.

[39] J. E. Marsden and M. West. “Discrete mechanics and variational integrators”. *Acta numerica* (2001), pp. 357–514.

[40] T. J. Hughes. *The finite element method: Linear static and dynamic finite element analysis*. New York: Dover Publications, Inc, 2000.

[41] E. Hinton, T. Rock, and O. Zienkiewicz. “A note on mass lumping and related processes in the finite element method”. *Earthquake Engineering and Structural Dynamics* 4 (1976), pp. 245–249. DOI: `10.1002/eqe.4290040305`.

[42] N. Newmark. “A Method of Computation for Structrual Dynamics”. *Journal of Engineering Mechanics* (1959).

[43] J. Nitsche. “Uber ein Variationsprinzip zur Lösung Dirichlet-Problemen bei Verwendung von Teilräumen, die keinen Randbedingungen uneworfen sind”. *Abhandlungen aus dem Mathematischen Seminar der Universität Hamburg* 36 (1971), pp. 9–15.

[44] Y. Renard. “Generalized Newton’s methods for the approximation and resolution of frictional contact problems in elasticity”. 256 (Apr. 2013). DOI: `10.1016/j.cma.2012.12.008`.

[45] F. Chouly. “An adaptation of Nitsche’s method to the Tresca friction problem”. *Journal of Mathematical Analysis and Applications* 411 (1 Mar. 2014). DOI: `10.1016/j.jmaa.2013.09.019`.

[46] T. Gustafsson, R. Stenberg, and J. Videman. “On Nitsche’s method for elastic contact problems”. 42 (2 Feb. 2020).

[47] P. Wriggers and G. Zavarise. “On contact between three-dimensional beams undergoing large deflections”. *Communications in Numerical Methods in Engineering* 13.6 (1997), pp. 429–438. DOI: `10.1002/(SICI)1099-0887(199706)13:6<429::AID-CNM70>3.0.CO;2-X`.

[48] C. Meier, W. Wall, and A. Popp. “A unified approach for beam-to-beam contact”. 315 (2017), pp. 972–1010. DOI: `10.1016/j.cma.2016.11.028`.

[49] P. Farah, A. Popp, and W. A. Wall. “Segment-based vs. Element-based integration for mortar methods in computational contact mechanics”. *Computational Mechanics* 55 (1 Jan. 2015), pp. 209–228. DOI: `10.1007/s00466-014-1093-2`.

[50] A. Bosten, A. Cosimo, J. Linn, and O. Brüls. “A mortar formulation for frictionless line-to-line beam contact”. *Multibody System Dynamics* 54 (1 Jan. 2022), pp. 31–52. DOI: `10.1007/s11044-021-09799-5`.

[51] C. Meier, M. Grill, W. Wall, and A. Popp. “Geometrically exact beam elements and smooth contact schemes for the modeling of fiber-based materials and structures” (2017), pp. 1–23. DOI: `10.1016/j.ijsolstr.2017.07.020`.

[52] S. B. Raknes, X. Deng, Y. Bazilevs, D. J. Benson, K. M. Mathisen, and T. Kvamsdal. “Isogeometric rotation-free bending-stabilized cables: Statics, dynamics, bending strips and coupling with shells”. *Computer Methods in Applied Mechanics and Engineering* 263 (Aug. 2013), pp. 127–143. DOI: `10.1016/j.cma.2013.05.005`.

[53] C. Meier, A. Popp, and W. Wall. “An objective 3D large deformation finite element formulation for geometrically exact curved Kirchhoff rods”. 278 (2014), pp. 445–478. DOI: `https://doi.org/10.1016/j.cma.2014.05.017`.

[54] L. Noels and R. Radovitzky. “Alternative approaches for the derivation of discontinuous Galerkin methods for nonlinear mechanics”. 74 (2007), pp. 1031–1045. DOI: `10.1115/1.2712228`.

[55] A. Koshakji, G. Chomette, J. Turner, J. Jablonski, A. Haynes, D. Carlucci, B. Giovanardi, and R. Radovitzky. “A robust computational framework for simulating the dynamics of large assemblies of highly-flexible fibers immersed in viscous flow” (*submitted*).

[56] B. Giovanardi, S. Serebrinsky, and R. Radovitzky. “A fully-coupled computational framework for large-scale simulation of fluid-driven fracture propagation on parallel computers” (2020).

[57] R. Penrose and J. A. Todd. "On best approximate solutions of linear matrix equations". *Mathematical Proceedings of the Cambridge Philosophical Society* 52 (1 1956). DOI: `10.1017/S0305004100030929`.

[58] G. Strang. *Linear Algebra and its Applications*. Third. Thomson Learning, 1988.

[59] A. W. Leissa and M. I. Sonalla. "VIBRATIONS OF CANTILEVER BEAMS WITH VARIOUS INITIAL CONDITIONS". *Journal of Sound and Vibration* (1991).

[60] S. K. Kota, S. Kumar, and B. Giovanardi. "A discontinuous Galerkin / cohesive zone model approach for the computational modeling of fracture in geometrically exact slender beams". *Computational Mechanics* (Dec. 2024). DOI: `10.1007/s00466-024-02521-0`.

[61] R. Radovitzky, A. Seagraves, M. Tupek, and L. Noels. "A scalable 3D fracture and fragmentation algorithm based on a hybrid, discontinuous Galerkin, cohesive element method". *Computer Methods in Applied Mechanics and Engineering* 200 (2011), pp. 326–344. DOI: `10.1016/j.cma.2010.08.014`.

[62] E. Cirak, M. West, S. Mauch, and R. Radovitzky. "Parallel finite element computation of contact-impact problems with large deformations". *Computational Fluid and Solid Mechanics* (2003).

[63] M. Ashby, H. Shercliff, and D. Cebon. *Materials Engineering, Science, Processing and Design*. First. Butterworth-Heinemann Elsevier, 2007.

[64] R. Lakes. "Foam Structures with a Negative Poisson's Ratio". *Science* 235 (4792 1987), pp. 1038–1040.

[65] R. S. Underhill. *Defense Applications of Auxetic Materials*. 2014.

[66] A. Clausen, F. Wang, J. S. Jensen, O. Sigmund, and J. A. Lewis. "Topology Optimized Architectures with Programmable Poisson's Ratio over Large Deformations". *Advanced Materials* 27 (37 Oct. 2015), pp. 5523–5527. DOI: `10.1002/adma.201502485`.

[67] S. Babaee, J. Shim, J. C. Weaver, E. R. Chen, N. Patel, and K. Bertoldi. "3D soft metamaterials with negative poisson's ratio". *Advanced Materials* 25 (36 Sept. 2013), pp. 5044–5049. DOI: `10.1002/adma.201301986`.

[68] J. Liu, T. Gu, S. Shan, S. H. Kang, J. C. Weaver, and K. Bertoldi. "Harnessing Buckling to Design Architected Materials that Exhibit Effective Negative Swelling". *Advanced Materials* 28 (31 Aug. 2016), pp. 6619–6624. DOI: `10.1002/adma.201600812`.

[69] Y. Jiang and Q. Wang. "Highly-stretchable 3D-architected Mechanical Metamaterials". *Scientific Reports* 6 (Sept. 2016). DOI: `10.1038/srep34147`.

[70] M. S. Kushwaha, P. Halevi, L. Dobrzynski, and B. Djafari-Rouhani. "Acoustic band structure of periodic elastic composites". *Physical Review Letters* 71 (13 1993), pp. 2022–2025. DOI: `10.1103/PhysRevLett.71.2022`.

[71] V. Laude. *Phononic Crystals: Artificial Crystals for Sonic, Acoustic, and Elastic Waves*. De Gruyter, 2015.

[72] Y. Chen, F. Qian, L. Zuo, F. Scarpa, and L. Wang. "Broadband and multiband vibration mitigation in lattice metamaterials with sinusoidally-shaped ligaments". *Extreme Mechanics Letters* 17 (Nov. 2017), pp. 24–32. DOI: `10.1016/j.eml.2017.09.012`.

A

Other applications for architected materials

Naturally, novel aerospace metamaterials demand superior strength properties than their monolithic counterparts, and hence, stiff struts in the context of architected cellular materials. Applications of metamaterials bearing the same structure, however, go well beyond aerospace. By tuning the lattice structure and opting for more compliant media, the mechanisms that underpin compressive responses in cellular materials can be harnessed for a myriad of fascinating industry applications. Perhaps the most notable example of architected materials yielding unique structural properties is found in auxetic materials. POISSON's ratio is a material property which characterizes the strain response of a loaded material by quantifying how much the material expands in the direction perpendicular to a compressive load or how much it contracts in the direction perpendicular to a tensile load. Nearly all materials behave in this way. In a contrasting scenario, when tensile loads result in perpendicular expansion and compression leads to perpendicular contraction, the material thus possesses a negative POISSON's ratio. It had long been postulated that such materials could exist, but this was only demonstrated in 1987 with a synthetic foam (whose structure comprised of reentrant unit cells with 24 faces) by Lakes [64]. A visual schematic of an auxetic material made up of *bowtie* cells is shown in Figure A.1 below.

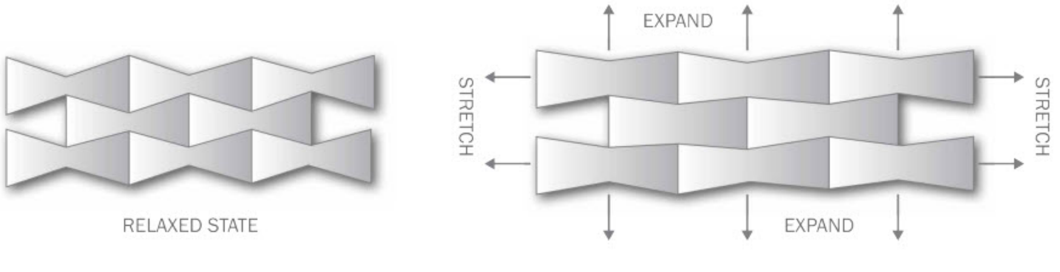

Figure A.1: Reentrant structure displaying an auxetic response to tensile load [65]

In continuing on the trajectory of soft-latticed auxetic material development, significant strides have been taken to fine-tune their properties. Clausen *et al.* demonstrated the application of topology optimization concepts in programming a material's POISSON's ratio (see Figure A.2) [66]. In a separate study, Babaee *et al.* introduced a repository of three-dimensional auxetic building elements, accompanied by systematic protocols for their selection and assembly [67]. The proposed cellular architecture, as detailed in [67], draws inspiration from crystal packing arrangements and utilizes elastic buckling, earning it the coined term *Bucklicrystals* (see Figure A.3). Another interesting case of soft buckling-enabled architected materials was conducted by Liu *et al.*, aiming to develop a medium capable of extreme volume change [68]. Rather than using elastic beam buckling however, the architected materials proposed in [68] leverage the mechanics of (thin) plate buckling to achieve a negative swelling effect when imbibing a solvent (see Figure A.4).

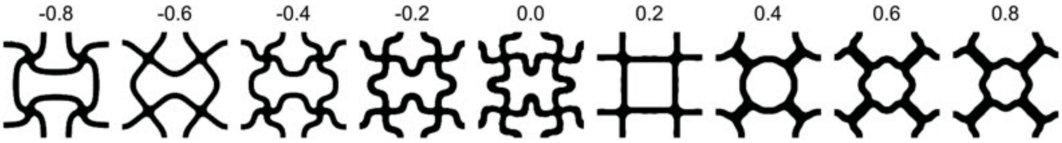

Figure A.2: Various cellular lattices used to achieve a specific POISSON's ratio [66]

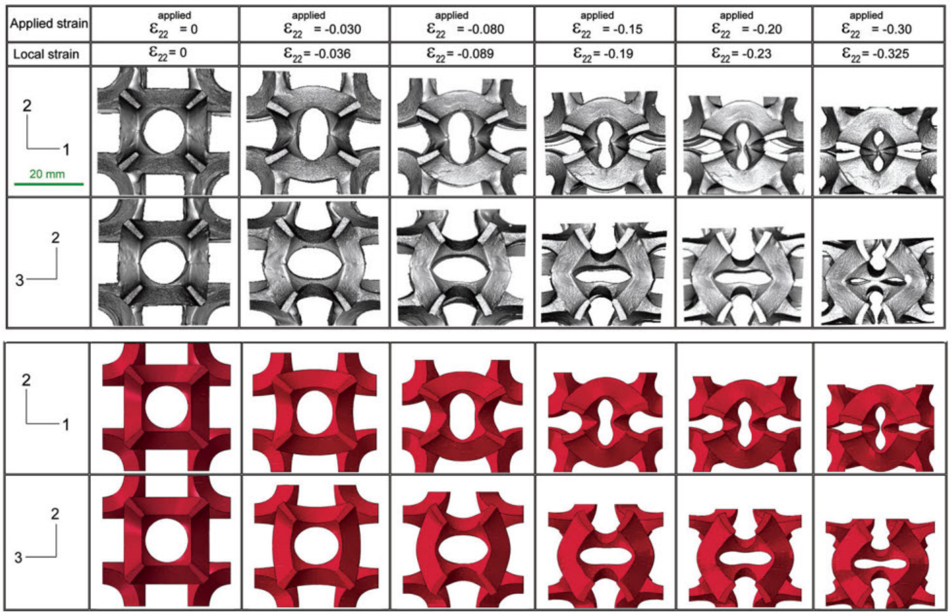

Figure A.3: Magnified cross-sectional views of a 6-hole Bucklicrystal taken from micro-CT X-ray scanning at different levels of strains along with corresponding simulation results [67]

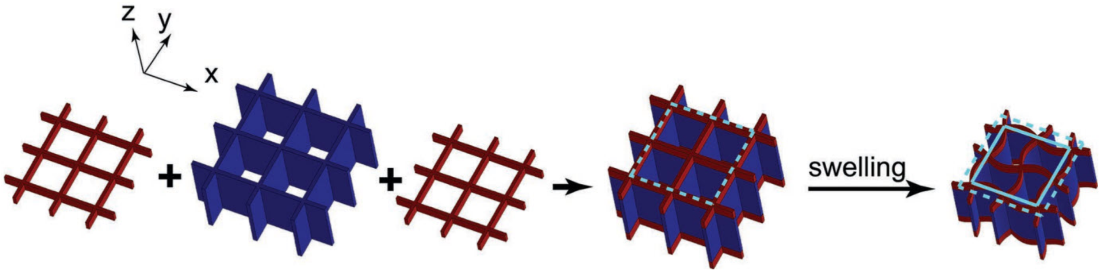

Figure A.4: Cellular structure comprised of a layered plate made of two materials with different mechanical properties buckling out of plane when imbibed with a solvent, leading to a negative swelling effect [68]

Jiang and Wang harmonize the properties afforded by highly-stretchable elastomers with the emergent properties of complex architectures to propose a framework for a new type of metamaterial [69]. Components crafted from these compliant lattices find versatile applications in robotics, serving as flexible connectors, in packaging for impact absorption, in disability rehabilitation devices, and in wearable electronics [69]. To conclude the discussion on potential metamaterial applications, another engineering use for architected materials shall be explored — *phononic crystals*. A large body of work surrounds the study of phononic crystals since the term was initially coined by Kushwaha *et al.* in their 1993 publication on the acoustic band structure of periodic elastic composites [70]. The term is derived from *phonon*, which are mechanical analogs to the electron serving as a dynamic metric for characterizing thermal and conductive properties in periodic lattices [71]. Furthermore, phononic crystals based on architected microlattices can be tailored to dampen broadband vibrational frequencies, as evidenced by Chen *et al.*'s work with metamaterials composed of sinusoidal-shaped ligaments (Figure A.5) [72]

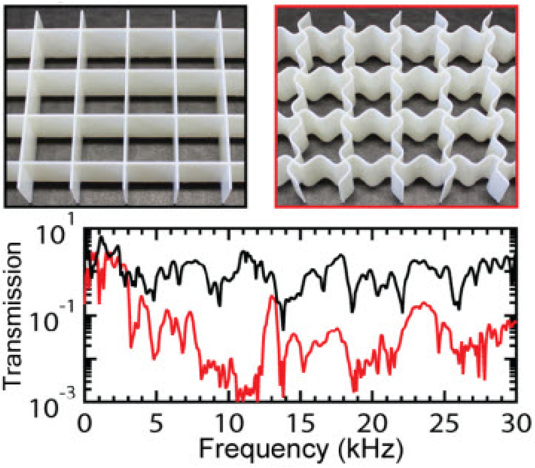

Figure A.5: Vibration control exhibited by lattice metamaterials with curved ligaments proposed by [72]

While this section has highlighted some of the most prevalent applications of architected materials in the literature, the potential uses for these unique structures remain largely uncharted. It is anticipated that the advent of additive manufacturing, combined with the ever-improving capabilities of machine learning models, will unlock the potential of architected materials for a multitude of yet-to-be-discovered engineering applications.

B

Template license

This thesis was made with a modified document template by Daan Zwaneveld, licensed via Creative Commons permission CC BY 2.0 ().